The Pennsylvania State University

The Graduate School

Department of Electrical Engineering

LOWER TROPOSPHERIC TEMPERATURE MEASUREMENT SCHEME FOR AN ADVANCED LIDAR ATMOSPHERIC PROFILING SYSTEM

A Thesis in

Electrical Engineering

by

Corey T. Slick

Submitted in Partial Fulfillment
of the Requirements
for the Degree of

Master of Science

May 2002

I grant The Pennsylvania State University the nonexclusive right to use this work for the University's own purposes and to make single copies of the work available to the public on a not-for-profit basis if copies are not otherwise available.

_____

Corey T. Slick

We approve the thesis of Corey T. Slick.

Date of Signature

_____ _____

C. Russell Philbrick
Professor of Electrical Engineering
Thesis Advisor

_____ _____

Victor Pasko
Associate Professor of Electrical Engineering

_____ _____

W. Kenneth Jenkins
Professor of Electrical Engineering
Head of the Department of Electrical Engineering

Abstract

LIght Detection And Ranging (LIDAR) systems can be used to sense atmospheric properties from a remote distance. The basic Raman lidar technique is to transmit a specific frequency of laser radiation into the sky, and collect the returned vibrational and rotational Raman-shifted frequencies with a telescope. By then separating and processing the return wavelengths associated with specific molecules, near real-time profiles of atmospheric properties can be obtained. Temperature measurement using this method was first suggest by Cooney [1972], and has since been examined by a number of groups. Current capabilities of lidar to measure temperature and other major properties of the lower atmosphere rival those of the antiquated and costly radiosonde method. The Lidar Atmospheric Profile Sensor (LAPS) is an optical remote sensing system developed at Penn State Univerisity for vertical profiling of lower tropospheric RF refractivity from aboard U.S. Navy ships. The system was demonstrated in late 1996, and has since been used in a number of atmospheric studies. The need for a variety of system performance modificaitons, noted during various field studies utilizing LAPS, has been observed and work toward an Advanced LAPS (ALAPS) is now underway. The design of the temperature measurement scheme presented here was seen as a second step toward the ALAPS system, the first step having been an upgrade in the electronics control system by Achey [2002]. As was shown, the capability of measuring atmospheric temperature is a significant factor in determining RF refractivity gradients. The design of a laser-based system to do this requires careful consideration of the safety of personnel working near or directly on the instrument after it has been deployed. The ability to measure atmospheric temperature with an eye-safe, ultraviolet transmission wavelength of 355 nm was examined for this reason. Selection of optical components and specification of the test setup to be used for daytime and nighttime profiling of lower tropospheric temperature, utilizing the LAPS system in a slightly modified form, has been done. A comparison of regression techniques for processing lidar rotational Raman temperature data is also given. This comparison showed agreement between calibration done with the instrument's theoretical temperature sensitivity curve and calibration with a radiosonde with the advantage that the theoretical curve provides better extension of the applicable range of profile temperatures.

Table Of Contents

List of Figures

List of Tables

Acknowledgements

I would like to thank my advisor, C. Russell Philbrick, for his assistance in all areas during my graduate studies. For the greater part of the laser system knowledge I have gained, I have Tom Petach of the Applied Research Laboratory to thank. Also from Penn State, thanks are due to Alex Achey, Ed Novitsky, Gregg O'Marr, Sriram Kizhakkemadam, Guangkun Li, Victor Pasko, Greg Babich, Laura Papish, Linda Becker, and Diana Feltenberger.

Further back, I would like to thank Mr. James Kahl and Mr. James Frankiewicz, for their foundational contributions to my success in a technical field.

And of course, I must thank my family and friends (and also my friend's *families* in some cases) for putting up with me during my time in college.

I acknowledge the support of my graduate research by the United States Navy SPAWAR PMW-185 office through the PSU Applied Research Laboratory, and by the United States Environmental Protection Agency, grant # R826373.

Chapter 1 - INTRODUCTION

The use of the pure rotational Raman spectrum of laser light backscattered from molecular nitrogen and molecular oxygen to measure atmospheric temperature was first proposed by Cooney [1974]. Cooney suggested that a differential technique, utilizing ratios of the signals received from two channels centered at different wavelengths in the rotational Raman spectrum, may be the best way to guarantee adequate temperature sensitivity, while removing most of the error sources induced by atmospheric and system parameter variations. The basic principle of this temperature measurement technique can be arrived at by examining the quantum-mechanical distribution of energy states within the rotational Raman spectrum. This analysis demonstrates that the backscattering cross-sections of the lines in the rotational Raman spectrum depend only on the temperature of the gas within the scattering volume examined, and known constants associated with each of the molecules from which the scattering occurred. In the case of air, N_2 and O_2 are the primary scatterers, and the constants related to them are known to a high degree of precision. Therefore, the rotational Raman spectra of N_2 and O_2 can be accurately predicted. This capability allows one to develop an optimal detection design for isolating particular regions of the rotational spectra.

Since the publication of Cooney's work, several groups have developed Light Detection and Ranging (LIDAR) systems based upon this method of temperature measurement. Among common system design variations are the laser transmitter pulse energy and wavelength, return signal wavelength separating technique, and calibration scheme. The main sources of difficulty with these systems continue to be sufficient blocking of elastic backscatter (which is done in our system with narrow-band optical filters), calibration of the temperature data, and system drift effects on calibration. Haris [1995] investigated the effect of the rotational Raman return from water vapor on the ratio of the photon counts received from two temperature channels, and found that the resulting systematic error was less than 0.2 K.

Optical remote sensing techniques are employed in place of microwave radar because backscattering cross-section, and hence return signal strength, is proportional to the fourth power of the frequency of electromagnetic energy transmitted. Rotational

Raman backscattering intensities are hundreds of times larger when transmitting at optical frequencies, particularly when the blue or ultraviolet portion of the spectrum is considered. Raman inelastic scattering is encountered when laser radiation is scattered by molecules at energy differences associated with the vibrational and rotational states of the molecule. The energy difference between the initial and final vibrational and rotational states of a molecule causes a wavelength shift of the scattered photons.

The Lidar Atmospheric Profile Sensor (LAPS) instrument discussed in this thesis was originally designed as a prototype instrument for the U.S. Navy to obtain RF refractivity measurements in a shipboard environment [Philbrick, 1996]. The instrument has been used in a number of scientific investigations following its demonstration for the U.S. Navy aboard the USNS Sumner during August-October, 1996. LAPS has demonstrated the capability of measuring major properties of the lower atmosphere, including temperature, specific humidity, RF refraction, optical extinction, and ozone concentration. The system can be operated autonomously, and provides near real-time measurements of these properties; whereas costly and time-consuming radiosonde releases are currently used to obtain these measurements. Lidar techniques have been shown to be accurate enough and have been developed to a point where they may be commercialized to replace sonde releases for routine atmospheric profiling. This thesis is intended to provide a stepping stone toward the development of the Advanced LAPS (ALAPS) instrument, which will serve as an engineering prototype for commercial production of lidar instruments.

My research at Penn State has focused on the method of temperature measurement using the pure rotational Raman spectra of N_2 and O_2. Specifically, a method for measuring atmospheric temperature using the backscatter from the ultraviolet 3^{rd} harmonic of the LAPS Nd:YAG laser has been devised. This configuration is intended to be suitable for both daytime and nighttime measurement capabilities. Also discussed is an alternate method for calibration of the LAPS lidar temperature measurements, and the future work required to demonstrate the validity of the design proposals presented in this thesis.

Chapter 2 - LAPS INSTRUMENT AND PROGRAM BACKGROUND

2.1 LAPS History and System Characteristics

The Lidar Atmospheric Profile Sensor (LAPS) instrument is a monostatic, optical remote sensing instrument using Raman scattering techniques to investigate properties of the lower atmosphere. The original purpose of LAPS was to demonstrate a prototype multi-wavelength Raman lidar capable of making RF refractivity measurements from aboard U.S. Navy ships. LAPS was designed and built at the Penn State University Applied Research Laboratory during the time period 1994 to 1996, and tested in its originally intended shipboard environment during August through October 1996 [Philbrick, 1996]. Since then, LAPS has been used in a number of tropospheric studies, which have been mostly concerned with the meteorological profiling and measurements of concentrations of ozone and particulate matter during air pollution events. Along with the capability of measuring ozone concentration, which is done by employing a DIfferential Absorption Lidar (DIAL) technique, the LAPS instrument is also capable of capturing vertical profiles of atmospheric temperature and water vapor concentration (specific humidity). The latter two measurements are of particular interest due to their significant contributions to RF refraction gradients in the lower atmosphere. Optical extinction measurements can also be made, providing characterization of the electro-optic environment, and making visibility determination possible.

The main components of the LAPS instrument are the transmitter, receiver, wavelength separation unit, detectors, data collection electronics and control system. Both the transmitter and receiver are contained in what has been termed the deck unit. The wavelength separation optics, detectors, data collection, and control electronics are housed in the console unit. The idea behind this configuration is that the deck unit was to be located on the deck of a Navy ship, while the console would be shielded from the weather in some other location on the ship. The deck unit was designed to be weather-tight, and has been proven time and again to be so.

The transmitter is a Nd:YAG laser, equipped with frequency doubling and quadrupling optics. The fundamental line of the transmitter is at 1.06 μm, giving transmitted signals at 532 nm (2^{nd} harmonic) and 266 nm (4^{th} harmonic). The remaining fundamental is dissipated on a water-cooled beam dump, which is shown in Figure 2.1. To reduce the beam divergence and the eye safety hazard for personnel working near the instrument, the transmitted beam is expanded by a 5X beam expander from 9 mm to 4.5 cm in diameter. Although the laser outputs a very high energy per pulse, the larger cross-section area achieved with the beam expander ensures a power density below ANSI standards for near-field diffuse reflections. The beam expander also decreases the divergence of the transmitted beam by five times to about 100 μrad so that it is match with the telescope and fiber 250 μrad field of view. Eye safety for people on aircraft and for people looking up from the ground due to an aircraft intercepting the beam has also been guaranteed by the installation of a safety radar, which protects a 6° cone angle around the beam. If an aircraft flies into the vicinity of the transmitted beam, the instrument will automatically be halted until the area is again clear. Table 2.1 summarizes the characteristics of the LAPS transmitter.

Table 2.1. LAPS transmitter characteristics.

Laser	Continuum Model 9030 with 5X Beam Expander
Pulse Frequency	30 Hz
Pulse Duration	8 ns
Fundamental Power	1.6 J/Pulse
Power Output at 1064 nm	Dumped into heat sink
Energy Output at 532 nm	800 mJ/Pulse – KD*P
Energy Output at 355 nm	400 mJ/Pulse – KDP
Energy Output at 266 nm	120 mJ/Pulse - BBO ; 90 mJ/Pulse – KD*P
Beam Divergence (after expansion)	0.1 mrad (FWHM)
Linewidth (1064)	30 GHz (1 cm^{-1})

The receiver subsystem, shown in Figure 2.2, consists of a reflecting telescope, constructed with a parabolic mirror 61 cm in diameter with a focal length of 1.5 m, and a fiber optic cable 1 mm in diameter located at the focal point of the mirror. The position of the fiber can be adjusted by the operator using computer controlled micropositioners. Also, a field stop 0.3 mm in diameter, which limits the field of view of the telescope and

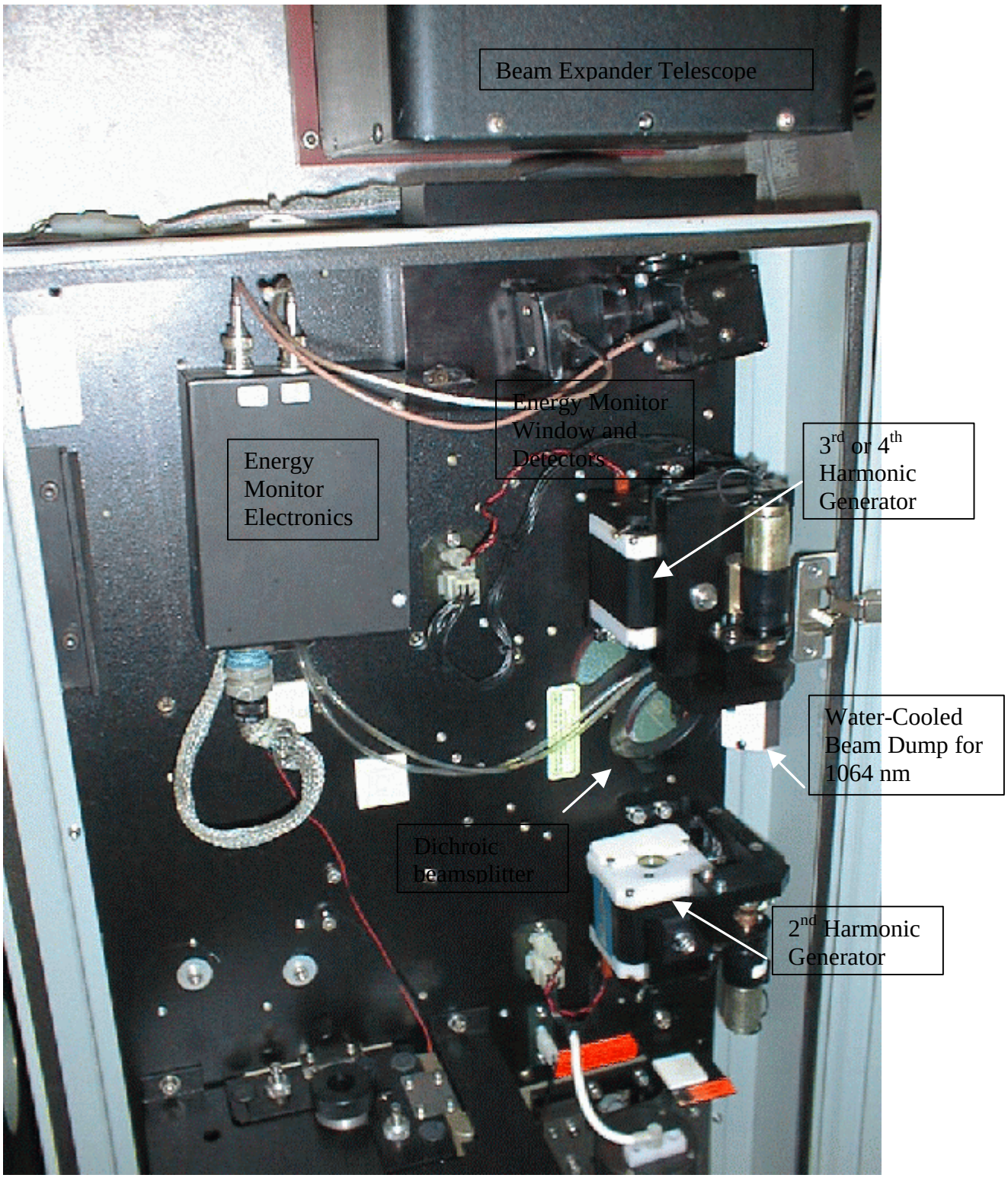

Figure 2.1. LAPS Transmitter optics (photo credit, C.R. Philbrick).

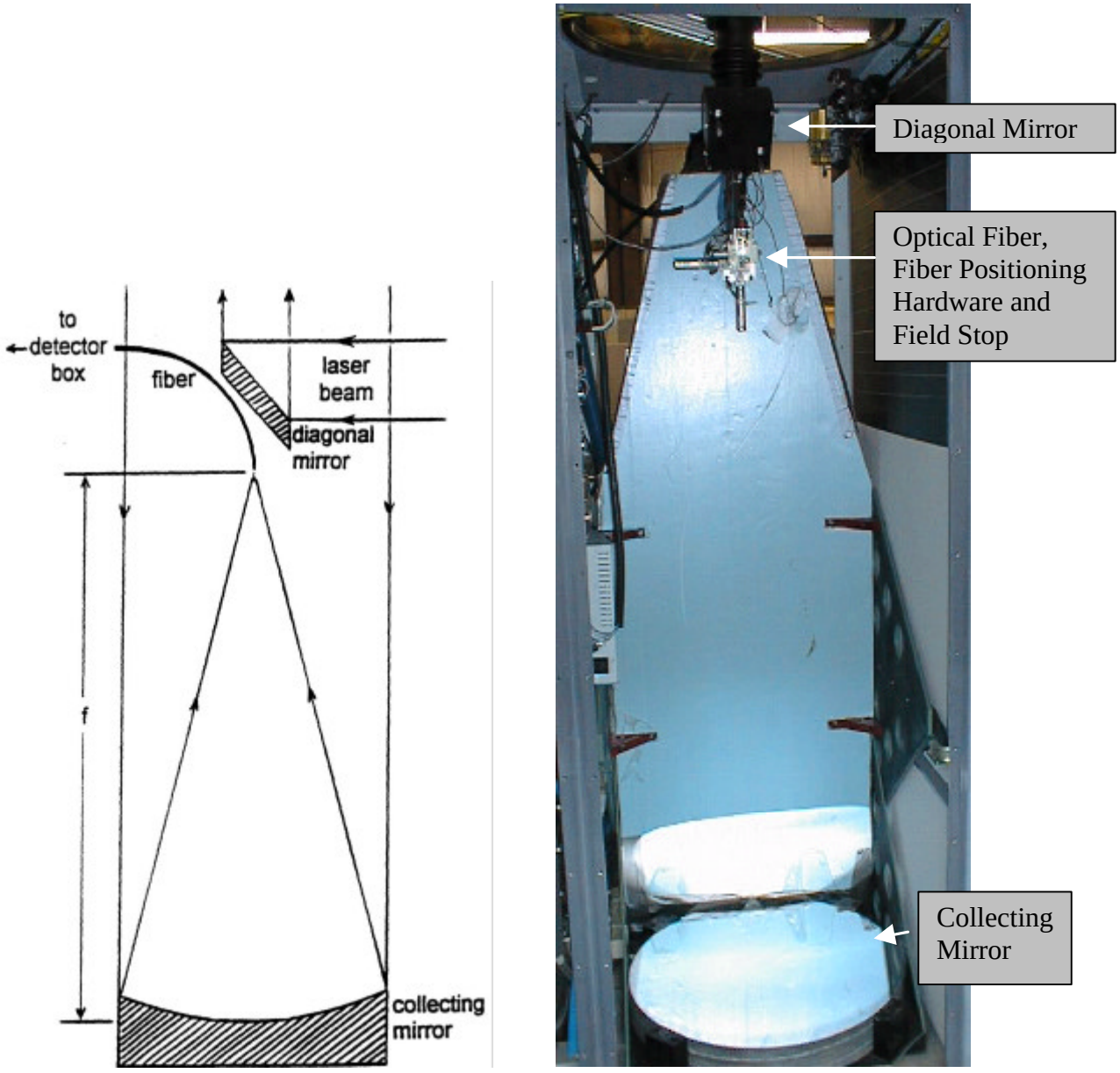

(a) (b)

Figure 2.2. LAPS transmitter and receiver components: (a) Schematic showing transmitted and received beams [Mulik, 2000]. (b) Photograph of transmission / reception aperture and receiving telescope (photos credit, C.R. Philbrick).

hence the background sky noise, is installed in the fiber housing. This aperture can be inserted and removed on command from the control console computer, and provides verification of the system optical alignment. The characteristics of the LAPS reception optics are given in Table 2.2. Aside from a newly-redesigned data acquisition computer [Achey, 2002] and various power supplies and cooling hardware, the components discussed above for the transmitter, receiver and safety subsystems basically sum up the content of the deck unit.

Table 2.2. Characteristics of LAPS receiver telescope optics.

<table>
<tr><td>Mirror</td><td>• Parabolic
• 61 cm diameter
• 1.5 m focal length</td></tr>
<tr><td>Optical Fiber</td><td>
<table>
<tr><td>[Chadha, 2001]</td><td>Core</td><td>Cladding</td></tr>
<tr><td>Material</td><td>SiO_2 (Surprasil)</td><td>Fluosil Standard</td></tr>
<tr><td>Refractive Index @ 633 nm</td><td>1.457</td><td>1.44</td></tr>
</table>
• 23 m length [Balsiger et al., 1996]
</td></tr>
<tr><td>Field Stops</td><td>• Fiber end – 1 mm diameter
• Insertable on command - 0.3 mm diameter</td></tr>
</table>

The deck and console units are linked by only the fiber optic cable discussed above and an ethernet cable, which connects the data acquisition computer in the deck unit to the control and data processing computer in the console unit. The fiber transfers the light collected with the telescope into the wavelength separation and detector subsystem. Using wavelength-separating (dichroic) and intensity-separating beamsplitters, the light is then directed to one of seven channels - each channel terminating on a photomultiplier tube (PMT). Just prior to each PMT is a series of optics. Each channel has a focusing optic, which adjusts the beam image to illuminate approximately ¾ of the photocathode active area of the PMT [Chadha, 2001]. Also, narrow-band optical filters, which block out all but a very narrow wavelength portion centered on the Raman line to be analyzed, are placed in each channel. A detailed discussion of the specification of these filters is given in Chapter 4. Some of the channels use neutral density filters to reduce the signal intensity to a level that will not saturate the

PMT. Finally, some of the channels use a broad-band filter to further increase the out-of-band rejection of a specific spectral region. The reader is referred to Chadha [2001] for a detailed description of the optics used in the wavelength separation and detection subsystem.

The PMTs incorporated into the LAPS instrument are operated in the photon counting mode, which means that the individual current pulses corresponding to each photo-electron generated at the photocathode and multiplied by a large gain factor, typically 10^4 to 10^7, and then individual current pulses are counted over a set threshold. This photon counting provides a more stable sensitivity than performing an A/D conversion on the DC current levels. This approach has been chosen for a number of reasons, including gain stability, reduction of dark current effects, and increased dynamic range. Dark current, which is due to false signals in the absence of any incident photons, is further reduced in the visible channels by thermoelectrically cooling the PMTs to reduce thermionic emission of the photocathode. The output signals of the PMTs consist of a noise floor, on which the full amplitude pulses are superimposed. The noise floor is generated by pulses which do not originate at the photocathode, and thus do not undergo the full gain of the PMT. A logic pulse is then generated for every signal spike which is greater than some minimum threshold level. Figure 2.3 shows a graphic representation of this process.

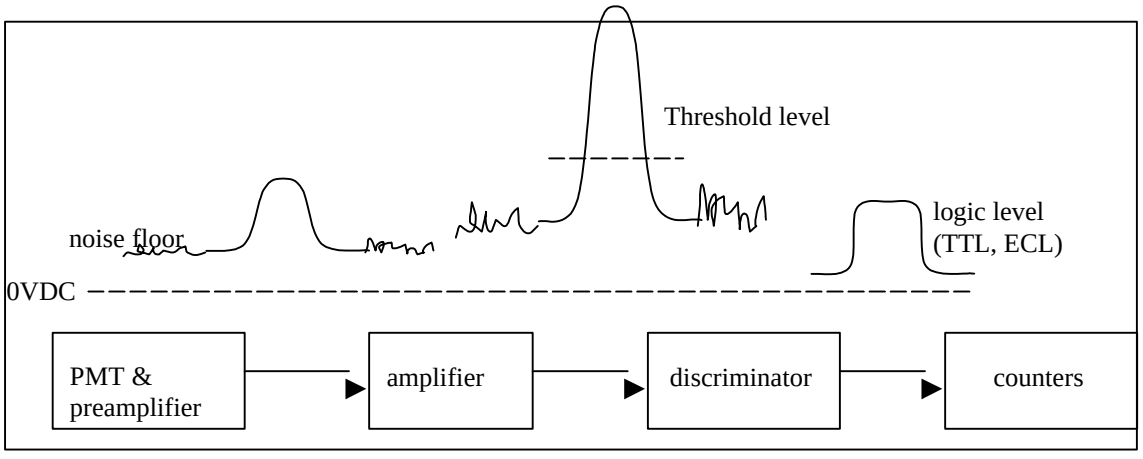

Figure 2.3. Pictorial representation of photon-counting electronics (diagram prepared by Alex Achey).

The data is then sorted into range bins, which are 500 ns in duration. The time interval corresponding to a vertical bin range resolution is,

$$R_{bin} = \frac{c}{2} \cdot t = \frac{3 \cdot 10^{8}[m/s]}{2} \cdot 500 \cdot 10^{-9}[s] = 75[m] \qquad 2.1$$

The factor of ½ comes from the fact that the outgoing pulse must travel up through the scattering volume and then back. Once the pulses have been binned, they are recorded in a raw data file as received photon counts at particular heights in specific Raman channels. Also recorded into the raw data files are a few other parameters measured by in situ sensors on LAPS.

The LAPS console computer uses the lidar scattering equation to processes the raw data files in real time and display vertical profiles of atmospheric temperature and water vapor concentration. Optical extinction and ozone profiles can be created in post-processing of the data. The lidar scatter equation gives the predicted backscattered power $P(l_R,z)$ received by a monostatic lidar system as [Measures, 1984]:

$$P(l_R, z) = P_T(l_T)x_T(l_T)x_R(l_R)\frac{ct}{2}\frac{A}{z^2}b(l_T, l_R)\exp\left[-\int_0^z [a(l_T, z') + a(l_R, z')]dz'\right] \qquad 2.2$$

where,

z	is the altitude of the volume element from which the return signal is scattered [m],
l_T	is the wavelength of the laser light transmitted [m],
l_R	is the wavelength of the laser light received [m],
$P_T(l_T)$	is the power transmitted at wavelength l_T [W],
$x_T(l_T)$	is the net optical efficiency at wavelength l_T of all transmitting devices [unitless],
$x_R(l_R)$	is the net optical efficiency at wavelength l_R of all receiving devices [unitless],
c	is the speed of light in air [m s^{-1}],
t	is the bin duration [s],

A is the area of the receiving telescope [m^2],

$b(\lambda_T, \lambda_R)$ is the back scattering cross section [m^{-1}] of the volume scattering element for the laser wavelength λ_T at Raman shifted wavelength λ_R [m^{-1}],

$a(\lambda, z')$ is the extinction coefficient at wavelength λ at range z' [m^{-1}].

Using this relation, the number of photon counts expected from the received signal can be determined. It should be noted that to predict returns for the LAPS system using Eqn. 2.2, $P_T(\lambda_T)$ should be the *time-average* transmitted power at wavelength λ_T.

2.2 LAPS Operating Principle

As stated earlier, the LAPS instrument is a monostatic lidar system which takes advantage of the phenomenon of Raman scattering. Monostatic systems are those in which the transmitter and receiver are at the same location, as opposed to multi- or bi-static systems, where the transmitter and receiver are not collocated. Additionally, LAPS is a coaxial system, meaning that the transmitted and received beams have the same optical axis. Other systems in which this is not the case are considered bi-axial.

Raman scattering results in the laser radiation scattered by a molecule being shifted in frequency from that transmitted. This energy difference between the incident and received photons is characteristic of the rotational and vibrational energy states of specific molecules. An atmospheric molecule is most likely in its ground state when its charge cloud is disturbed by an incident photon. During the scattering vibrational process, a molecule will increase the energy within the electron cloud to a virtual energy level equivalent to that of the scattering photon. Upon relaxation from the virtual energy level, a photon is usually emitted with the incident energy plus or minus the small increment associated witht the thermal Doppler velocity of the molecule. However the photon can have less energy by the magnitude of the vibration and rotation energy states when Raman scattering occurs. This scenario is termed the Stokes transition. If however a molecule is in an unlikely excited vibrational energy state prior to interaction with an incident photon, then the emitted photon will have increased energy when the molecule returns to the ground state, and will be shifted to a higher frequency than that incident,

and results in the anti-Stokes transition. Both of these processes are illustrated in Figure 2.4. As is shown in the figure, the rotational energy levels, represented by the rotational quantum number J, are much more closely spaced than the vibrational levels, denoted by v. This fact can present a problem when attempting to isolate portions of the rotational spectrum with narrow-band optical filters, but this is discussed later in section 4.3.

Objects with complex shape inherently have three independent moments of inertia, each corresponding to a physical dimension. Molecules having one moment equal to zero are classified as *linear rotors*. Diatomic molecules, such as N_2 and O_2, are of this type. Rotational Raman energy levels, transitions allowed by the $\Delta J = \pm 2$ quantum selection rule and corresponding wavenumber shifts of a typical rotational Raman spectrum of a linear rotor are shown in Figure 2.5 [Atkins, 2000]. Important to note for calculating N_2 and O_2 rotational Raman returns from the atmosphere are the relative concentrations of the two species. These two molecules are the principle constituents of the atmosphere, N_2 making up approximately 78% and O_2 21%. The backscattering intensities of the N_2 and O_2 rotational Raman lines are scaled by these percentages when projecting atmospheric returns.

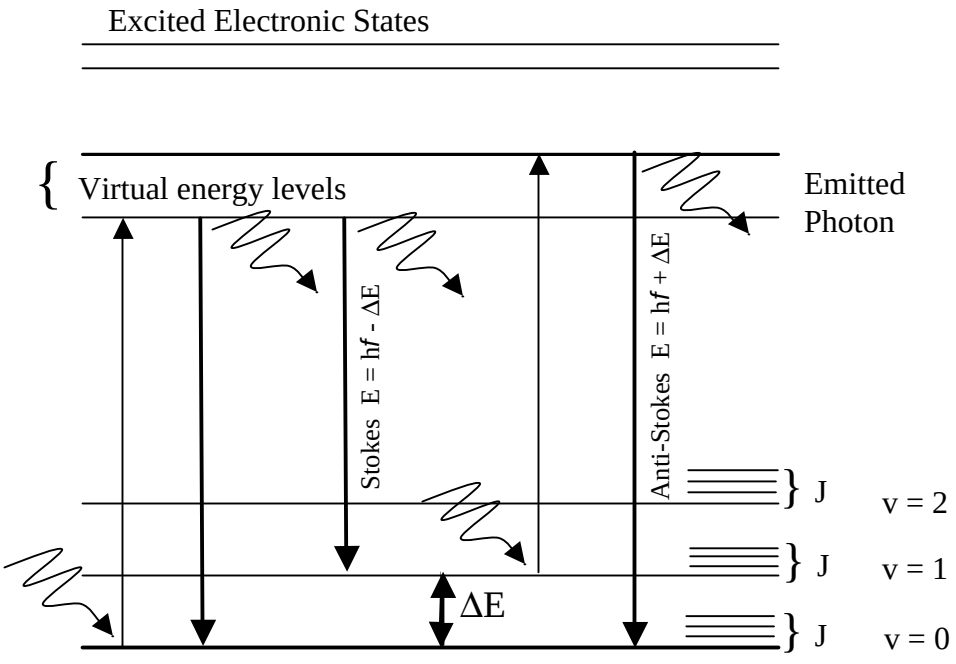

Figure 2.4. Graphical representation of Raman scattering theory, showing both Stokes and anti-Stokes transitions [Mulik, 2000].

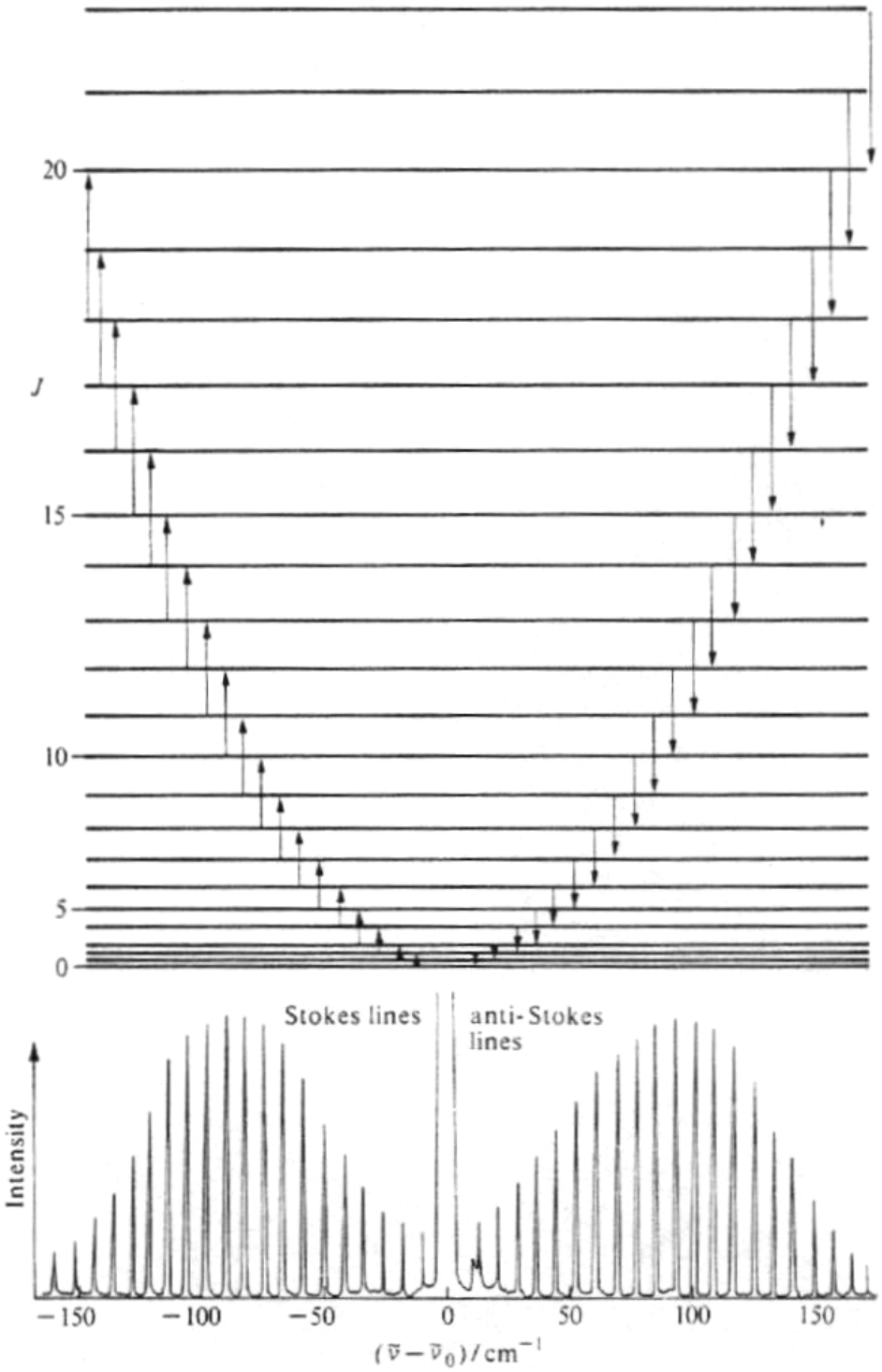

Figure 2.5. Rotational Raman energy levels, allowed $\Delta J = \pm 2$ transitions and corresponding wavenumber shifts of a typical rotational Raman spectrum of a linear rotor [Atkins, 2000].

2.3 LAPS Measurements

Utilizing ratios of the lidar scatter equation (Eqn. 2.2), vertical profiles of atmospheric temperature, water vapor concentration (specific humidity), ozone concentration, and optical extinction can be determined with the LAPS instrument. In the case of temperature measurement, the ratio of the rotational Raman signals from the 528 nm and 530 nm channels are taken. This ratio curve is then least-squares fitted to radiosonde data taken at approximately the same vertical locations. A second-order polynomial of the form [Haris, 1995],

$$T(R) = aR^2 + bR + c \qquad 2.3$$

where,

T(R)	is the temperature as a function of the lidar signal ratio
R	is the lidar ratio of the 528 nm signal and the 530 nm signal
a, *b*, and *c*	are calibration constants determined from filter sonde data

is used for this purpose. An improved method for regression fitting LAPS temperature data is discussed in Chapter 6.

Water vapor concentration as a function of altitude, W(z), is calculated by taking the ratio of the first Stokes shift from the water molecule to that of molecular nitrogen, and multiplying by a calibration constant. Specifically [Rajan et al., 1994],

$$W(z) = K_{cal} \frac{S_{H2O}(z)}{S_{N2}(z)} \qquad 2.4$$

where,

S_{H2O} is the signal from the vibrational Raman shift of H_2O at 660 or 295 nm,

S_{N2} is the signal from the vibrational Raman shift of N_2 at 607 or 284 nm,

K_{cal} is a calibration constant.

The Stokes shift from either 532 nm or 266 nm is used, depending upon whether the measurement is taken during the daytime or at night. The intensity of the day sky background in the visible portion of the spectrum requires that the visible channels be disabled and protected during the daytime. The daytime saturation of the sensitive PMTs would result in nonlinear performance, statistically useless data, and in event of severe overload could cause irrepairable damage. This inoperability of the visible channels in the daytime is one of the motivations of moving to 355 nm transmission.

Operating in the 230 nm – 300 nm "solar blind" region of the spectrum (the region where stratospheric ozone absorbs the incoming solar radiation) permits daytime measurements. Considering that the solar irradiance at the surface of the earth is 2.5 times lower at 355 nm than at 532 nm, while the backscatter cross-section for 355 nm radiation is five times larger than that for 532 nm radiation, leads us to consider operating in this region. The rotational lines at the third harmonic are also closer together, which decreases the filter bandwidths necessary to capture N_2 and O_2 rotational lines [Haris, 1995]. The filters specified in this thesis have a FWHM of 0.1 nm, out-of-band blocking of OD-5, and OD-8 to 10 blocking at the laser line. These factors can increase the SNR by increasing the number of rotational lines within the filter bandwidth and also by limiting the background noise contribution to the signal. In the case of this study, the increase in SNR is due to reduction of background noise, since only one pair of rotational lines is intended to be examined within each filter passband. In addition, a higher energy pulse is achievable at 355 nm than at 266 nm (approximately 350 mJ compared to 100 mJ) with the current laser transmitter.

Optical extinction profiles are measured at multiple wavelengths and are based on gradients in molecular profiles [O'Brien et al., 1996]. Ozone profiles are calculated by using a DIAL analysis of the ratio of the Raman-shifted O_2 and N_2 signals. These measurements will not be discussed in detail here since they have no bearing on the goal of this thesis. Projected measurements obtainable using simultaneously transmitted wavelengths of 355 nm and 532 nm are given in Table 2.3.

Table 2.3. LAPS measurements using 532 and 355 nm transmission [Esposito, 1999].

Property	Measurement	Altitude	Time - Resolution
Water Vapor	660/607 (H_2O/N_2) 408/387 (H_2O/N_2)	Surface to 5 km Surface to 5 km	Night - 1 min Day & Night - 1 min
Temperature	528/530 353/354 Rotational Raman	Surface to 5 km Surface to 5 km	Night - 10 to 30 min Day & Night - 10 to 30 min
Extinction 530nm	530 nm Rotational Raman	Surface to 5 km	Night - 10 to 30 min
Extinction 607nm	607 nm N_2 Vibrational Raman	Surface to 5 km	Night 10 to 30 min

Chapter 3 - Advanced Lidar Atmospheric Profile Sensor

3.1 Overview of ALAPS

The Advanced LAPS (ALAPS) system is intended to be the final engineering prototype for a production lidar system to be used aboard Navy ships; the LAPS instrument being the functional demonstration prototype for ALAPS. The main purpose of ALAPS is to provide the capability of measuring lower atmpspheric RF refractivity, which has a significant effect on electromagnetic wave propagation in the frequency range up to approximately 5 GHz – hence the appropriateness of employing remote sensing techniques at optical frequencies (~ 10^{15} Hz) for this purpose. The U.S. Navy has set a number of specifications for the ALAPS system, among those are:

- Capability to measure major atmospheric properties contributing to RF refraction – water vapor (specific humidity) and temperature
- Invisible, eye-safe transmission wavelength
- Day / night operation
- Automatic operation and self-calibration
- Increased resolution from 75 m to 15 m - the current design approach is to use 3 m range and 1 GHz photon counting electronics
- Reduced size of deck unit – volume less than 1 m^3
- Reduced power requirement to 30% of LAPS, and use shipboard heating and cooling systems
- Provide electro-optic propagation measurement of optical extinction
- Provide measurement capability for 4 month deployment between required major servicing

The first step toward reducing the size of the instrument was made by Achey [2002] in redesigning the electronics control system. This upgrade was also a significant step forward in ensuring automated operation of the instrument by incorporating a hard real-time operating system into the control computer [Achey, 2002]. Our laboratory has also previously demonstrated 1 GHz photon counting electronics, which provides 25X the

range resolution available with LAPS. The goal of this thesis is to add to the foundation already begun for ALAPS by providing a detailed method for making daytime and nighttime measurements of atmospheric temperature, utilizing an invisible, eye-safe transmission wavelength.

3.2 ALAPS Design Considerations and Requirements

3.2.1 Invisible Operation

A preferred attribute of a system designed to make repeated measurements of atmospheric properties in a populated area is that it should not draw attention. Figure 3.1 shows scattering of the LAPS 2nd harmonic transmission through a cloud layer during night operation in northeast Philadelphia during the summer 2001 North East - Oxidant and Particle Study (NE-OPS) campaign. At bottom-center of the picture is shown the readily visible beam's typical appearance in the night sky, where the beam is usually visible for distances up to 3 km. Much easier to observe however, is the scattering shown in the center of the photograph. This is obviously not a desirable side-effect. This blatancy is also a problem with the currently used radiosonde method due to its data transmission at L-band wavelengths over a range of hundreds of kilometers. The atmospheric measurements made with LAPS are also visible at night over a range of a few kilometers, and hence our motivation to use remote sensing techniques only at ultraviolet wavelengths for ALAPS.

The wavelength band of the visible portion electromagnetic spectrum is approximately 400 – 700 nm, and 532 nm is relatively close to the midpoint. This central region of the visible spectrum causes the greatest response in the eye. Changing to a transmission wavelength of 355 nm moves the operating wavelength below that which is visible to humans, hence eliminating the problem of the output beam being easily observed and detected. Additionally, one may suspect that the ultraviolet wavelengths which are Raman-shifted to the visible portion of the spectrum may be detectable in the night sky. This is not the case however, regardless of transmitted harmonic, due to the extremely low signals due to the small backscattering cross-sections encountered.

Figure 3.1. Second harmonic of the LAPS Nd:YAG laser scattering through a low cloud layer.

3.2.2 Eye-Safe Emission

Using the current laser system installed in LAPS, output pulse energy at 355 nm is approximately 400 mJ. The ANSI standard Maximum Permitted Exposure (MPE) to a pulsed laser of this wavelength is 6.7 mJ cm^{-2}. At the exit of the laser cabinet, the beam has a radius of 0.45 cm, giving an area of 0.636 cm^2. Hence, the energy density even after the 5X beam expander is 126 mJ cm^{-2} – an unacceptable level for a production

instrument. To bring the energy density to a level at or below the MPE, either the beam would have to be expanded to a larger size at the exit of the laser cabinet, or the pulse energy of the laser decreased. For use in ALAPS, it has been shown that a laser giving 300 mJ / pulse, with an output beam diameter of 10 mm expanded 15X results in an energy density of 1.7 mJ cm^{-2} – about one-fourth of the MPE at 355 nm. This pulse energy should also be sufficient to give a backscattered signal strong enough to produce acceptable SNRs in the detection system.

3.2.3 Required Measurement Capabilities

As was previously stated, the original intent of the LAPS instrument was to measure RF refractivity profiles in the lower atmosphere. These profiles can be used to determine electromagnetic refraction and ducting conditions, which are of concern in radar tracking and communications applications. The determining factor in EM ducting are gradients in the localized refractive index, n, which are which are cause by gradients in the scattering by water vapor and molecular density. Measurements of temperature and water vapor concentration give the capability of calculating the index of refraction based upon an empirically developed relationship. However, changes in refractive index through the atmosphere vary so slightly from unity that a more suitable unit to define refractivity conditions was adopted. The refractivity, which is given in N-units, represents the significant figures of n. RF-refractivity is then given by the relation [Philbrick, 1996],

$$N = (n-1)\cdot 10^6 = 77.6\frac{P}{T} + 3.73\cdot 10^5\frac{e}{T^2} \qquad 3.1$$

where,

$$e = \frac{(r\cdot P)}{r+621.97} \qquad 3.2$$

and,

e is the water vapor partial pressure [mb]

P is the surface pressure [mb]

r	is the specific humidity (water vapor concentration) [g kg^{-1}]
T	is the temperature [K]

The lidar data provides the profiles of specific humidity and temperature to input for calculation. The pressure is measured at the surface and then can be calculated at all other altitudes from the hydrostatic equation.

Modified refractivity M incorporates the curvature of the Earth and is defined by [Wave Propagation Panel, 1990],

$$M = \left(\frac{h}{a}\right)\cdot 10^6 = N + 0.157h \qquad 3.3$$

where,

h	is the height above the earth's surface [m]
a	is the radius of Earth [m]

Plotting atmospheric profiles of refractivity in M-units makes trapping conditions immediately obvious. Idealized examples of common ducting conditions caused by different M-profiles are given in Figure 3.2. As can be seen from the figure, trapping layers will occur for any negative M gradient. The strength of the duct is related to the magnitude of the change in M units across the duct. The optimum coupling height shown in Figure 3.2(a) is the height at which energy from a radiator placed at that height would be most effectively trapped, relative to other heights within the duct.

The four atmospheric refractive conditions are illustrated in Figure 3.3 and Table 3.1 gives corresponding N- and M-unit gradients. It is seen from Figure 3.3 that what characterizes the different refractive conditions is the radio ray curvature with respect to the curvature of the Earth. Trapping in a duct occurs when the radio ray curvature, induced by the refraction gradient, is greater than the curvature of the Earth. Figure 3.4 demonstrates how profiles created with the LAPS instrument of water vapor concentration and temperature contribute to determining modified refractivity gradients.

Gradients in M-units can then be fed into other systems and used to develop radar coverage pattern diagrams. These diagrams are used to exploit the electromagnetic

environment for tactical purposes. A potential tactical use of knowledge of radar coverage patterns is illustrated in Figure 3.5. Radiosonde measurements of temperature, pressure and humidity are the primary data input to the system. Moving from sonde measurements of these atmospheric properties to measurements made by optical remote sensing using lidar techniques would enhance the time resolution of measurements to very near real-time (1 to 5 minutes), and provide continuous results.

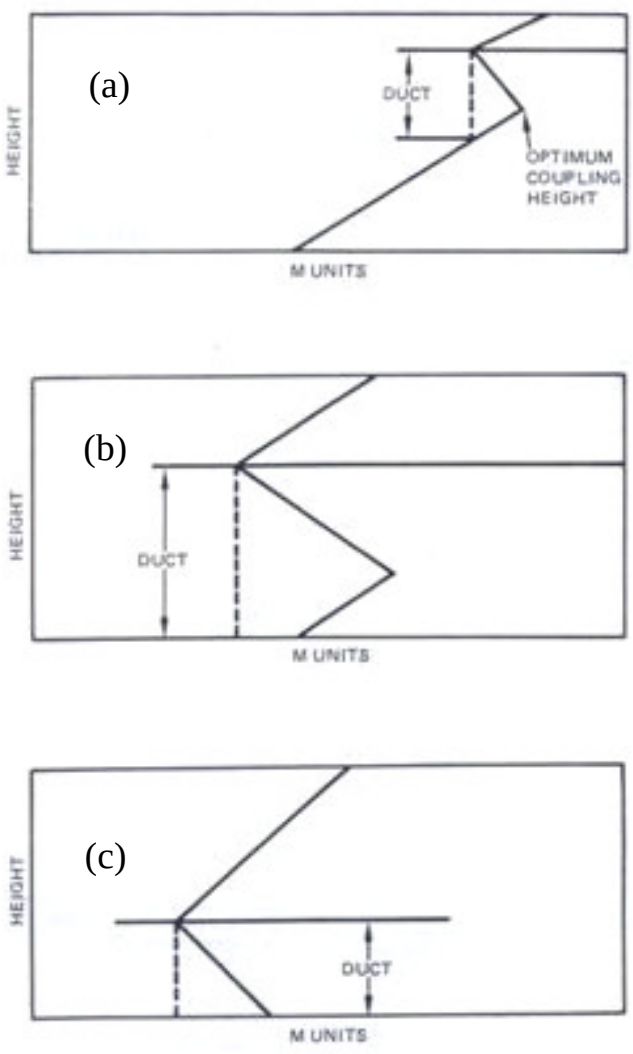

Figure 3.2. Effects of different M-profiles on ducting conditions. (a) Elevated duct (trapping layer elevated), (b) Surface-based elevated duct (trapping layer elevated), and (c) Surface duct (trapping layer on surface) [Helvey et al., 1994].

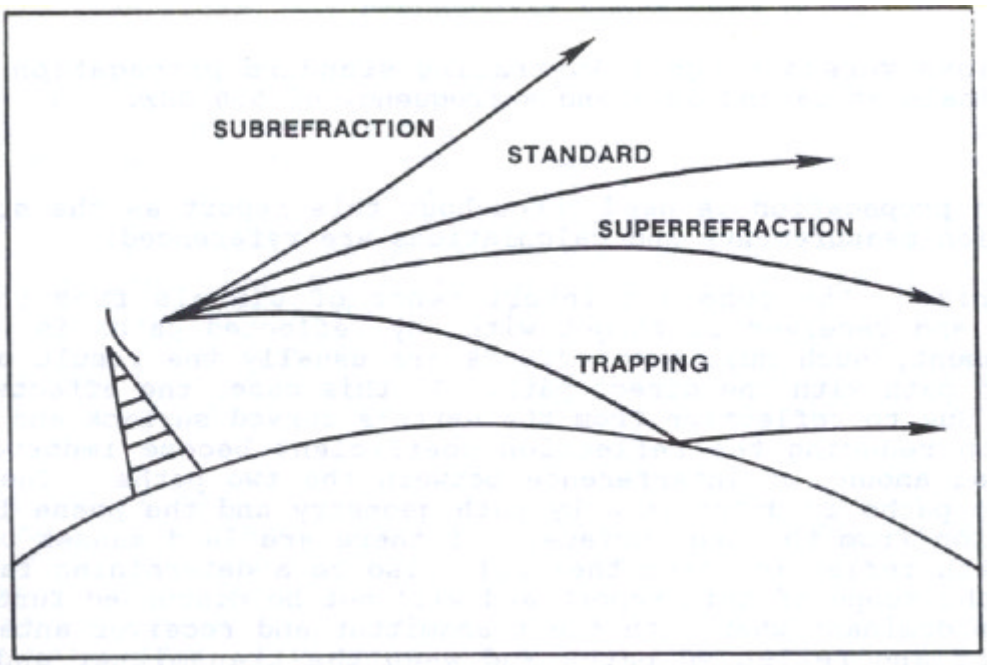

Figure 3.3. Relative bending for each of the four refractive conditions [Wave Propagation Panel, 1990].

Table 3.1. Refractive regimes, as referred to Figure 3.3 [Wave Propagation Panel, 1990].

Condition	**N-Gradient [N km^{-1}]**	**M-Gradient [M km^{-1}]**
Trapping	$dN/dh \leq -157$	$dM/dh \leq 0$
Superrefractive	$-157 \leq dN/dh < -79$	$0 < dM/dh \leq 78$
Standard	$-79 \leq dN/dh < 0$	$78 < dM/dh \leq 157$
Subrefractive	$dN/dh > 0$	$dM/dh > 157$

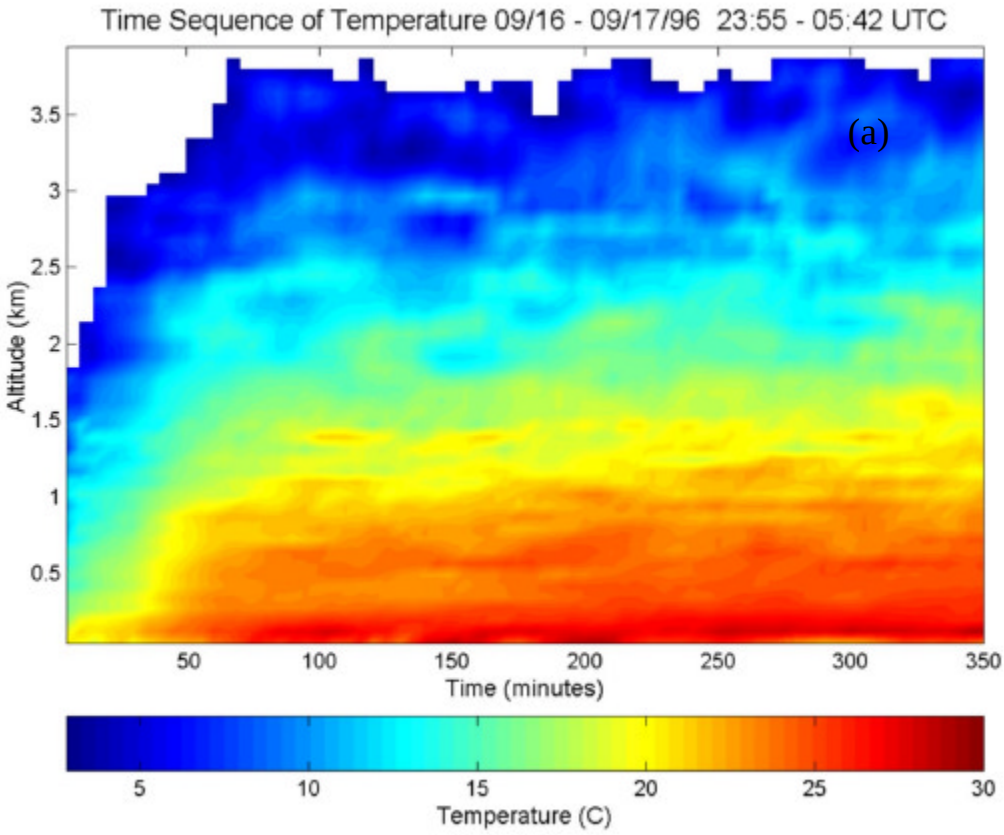
Time Sequence of Temperature 09/16 - 09/17/96 23:55 - 05:42 UTC
(a)
Altitude (km)
3.5
3
2.5
2
1.5
1
0.5
50
100
150
200
250
300
350
Time (minutes)
5
10
15
20
25
30
Temperature (C)

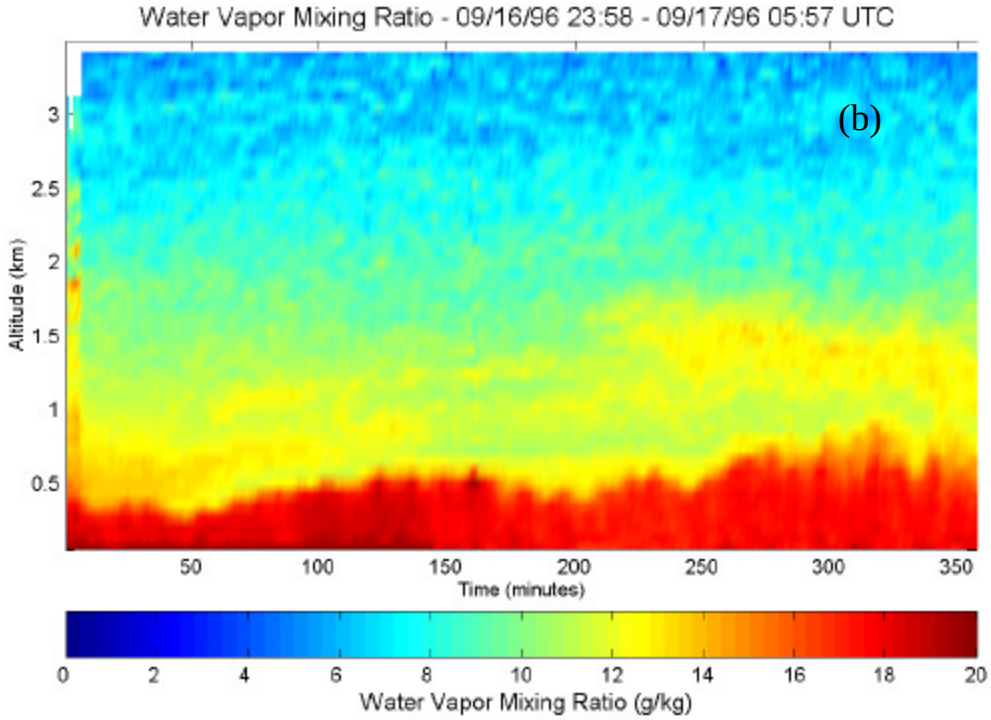
Water Vapor Mixing Ratio - 09/16/96 23:58 - 09/17/96 05:57 UTC
(b)
Altitude (km)
3
2.5
2
1.5
1
0.5
50
100
150
200
250
300
350
Time (minutes)
0
2
4
6
8
10
12
14
16
18
20
Water Vapor Mixing Ratio (g/kg)

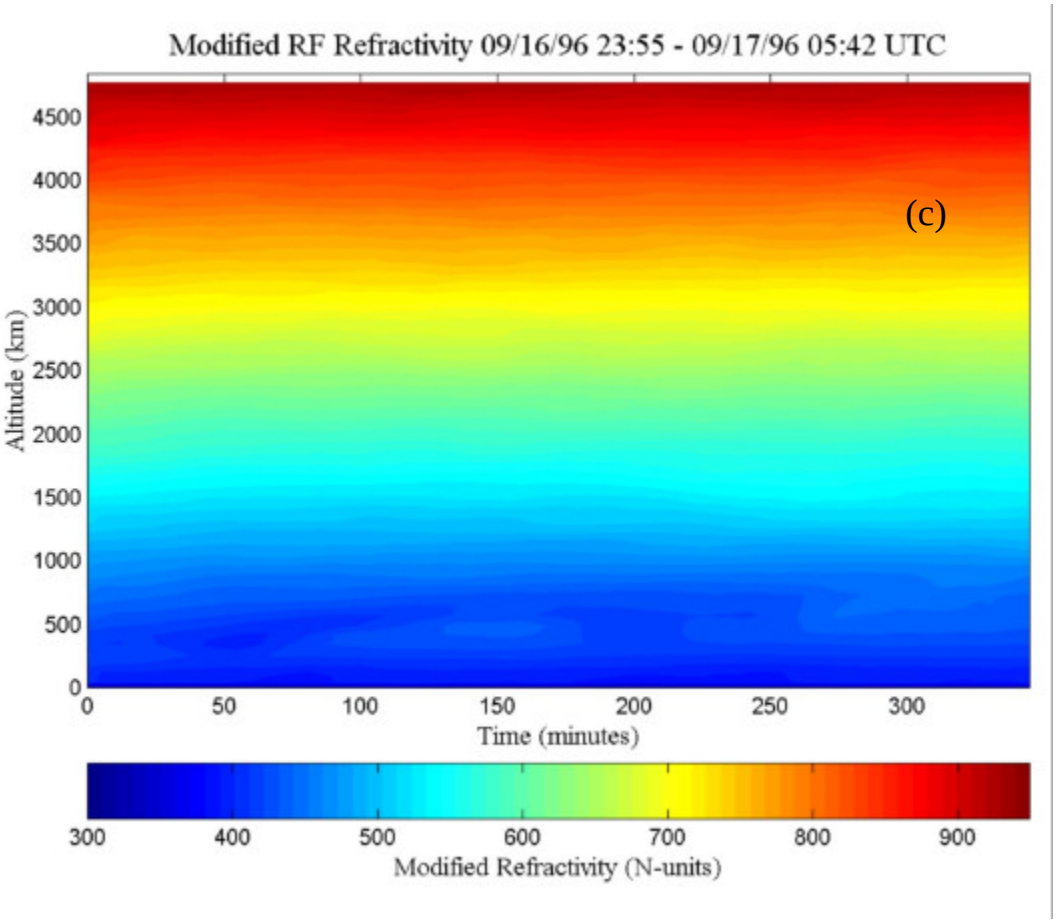

Figure 3.4. Effects of (a) temperature, and (b) water vapor on (c) modified RF refractivity.

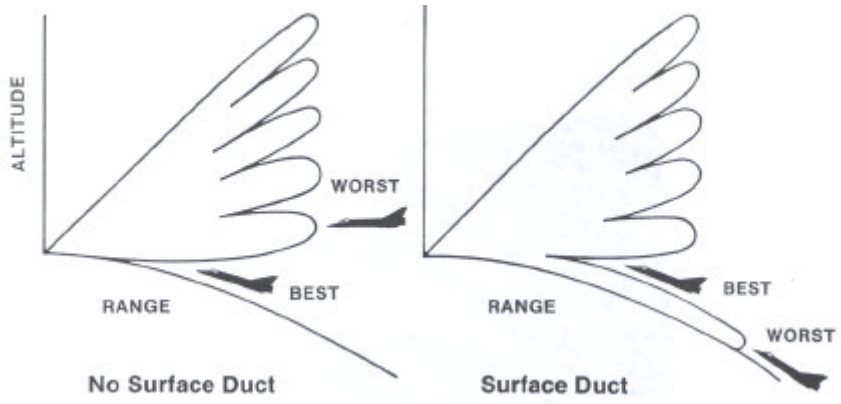

Figure 3.5. Tactical use of radar coverage [Wave Propagation Panel, 1990].

Chapter 4 - MODELLING AND SIMULATION

4.1 LAPS Transmitter Center Wavelength Determination

All analyses done in this thesis are based upon knowing very precisely the transmitted wavelengths produced by the LAPS laser. The most obvious way to obtain this information is to measure the output wavelengths. This was not possible however, because even the more basic wavelength measuring instruments are very costly. There are other methods that could be devised to measure the output wavelengths, but they would be much too sensitive to experimental setup errors. The alternative method that was settled on relies on the laser manufacturer's specifications, available publications, and the output wavelength dependence on laser rod temperature.

The temperature of the water in the laser cooling reservoir is measured directly in the reservoir after being pumped through the laser heads and then through a 3.5 kW water-to-water heat exchanger. A temperature regulator uses a proportional valve to keep the water coolant within ±1 ºC of a preselected standard operating condition. The temperature of the water coolant settles at approximately 87 °F (30.6 °C). The temperature of the laser rod, where the flashlamp energy is absorbed, is obviously higher than the equilibrium water coolant temperature. Since the oscillator and amplifier laser heads each have different rod diameters, flashlamp sizes and flashlamp energies, it would be extremely difficult to determine precisely the heat transferred to the coolant water from a single head.

The manufacturer gives the oscillator output wavelength as 1064.14 nm at room temperature. Since the LAPS laser does not use an injection seed laser, the output center wavelength cannot be specified to additional decimal places. According to Marling [1978], the shift in spontaneous emission center wavelength with change in crystal temperature for the Nd^{3+}:YAG line centered near 1064 nm is approximately 4.6 pm $°C^{-1}$. A plot of this temperature dependence, along with the maufacturer's data and a fit to both data sets, is shown in Figure 4.1.

The temperature of the oscillator rod will determine the center line position of the transmission. A reasonable assumption for the oscillator rod temperature is to add an

additional 10 ºC to the temperature of the water measured in the coolant reservoir. Figure 4.2 shows calculated output 3rd harmonic wavelength dependence on temperature for a range of operating temperatures. As can be seen from the plot, a shift of only 0.016 nm exists for the center wavelengths produced at 30.6 ºC and 40.6 ºC (87 °F and 105.1 °F), if one goes by Marling's data. This shift corresponds to 15.6% of the passband width of the optical filters used. It was neglected in subsequent calculations because of uncertainty in increased oscillator rod temperature over that of the water coolant, but the effect of it added to additional tolerances encountered later may be to decrease the received signal strength. For subsequent calculations, an average center wavelength shift of 4.6 pm $ºC^{-1}$ was assumed, and the third harmonic wavelength was rounded to three decimal places and taken as 354.714 nm.

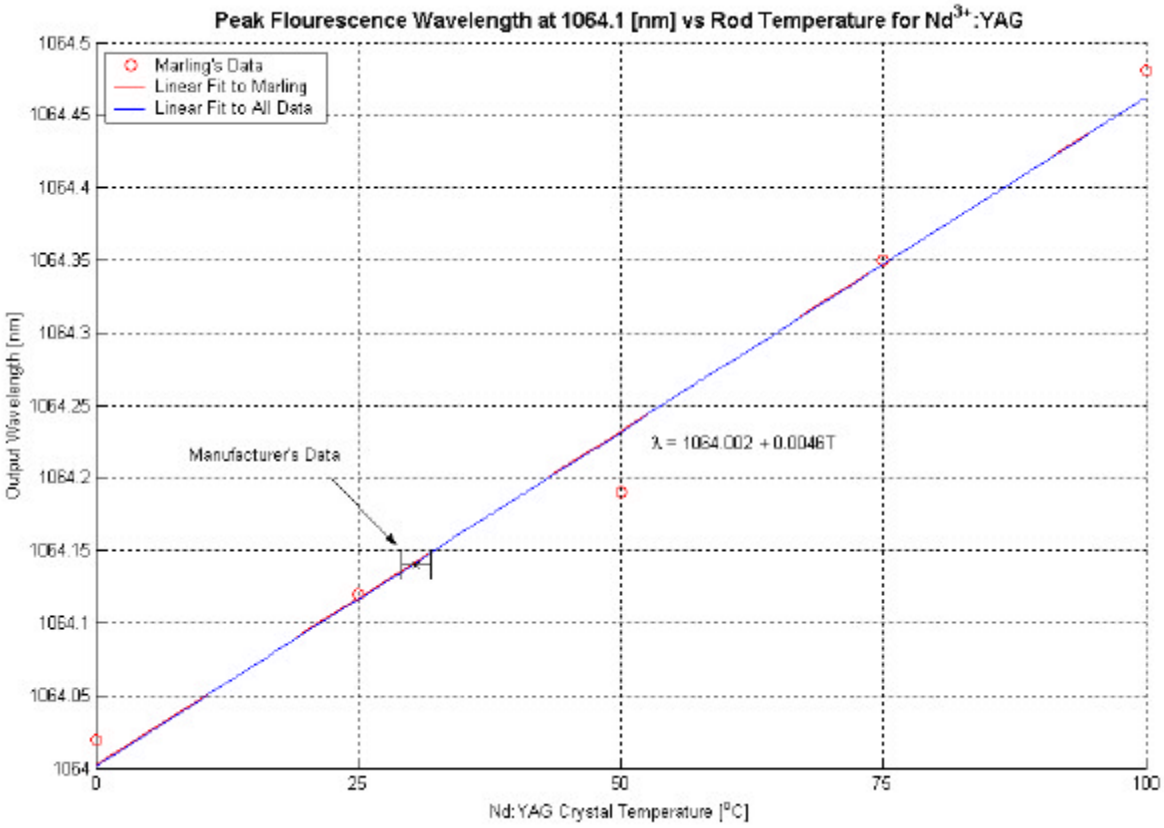

Figure 4.1. Output wavelength dependence on laser rod temperature, including that of Marling [1978].

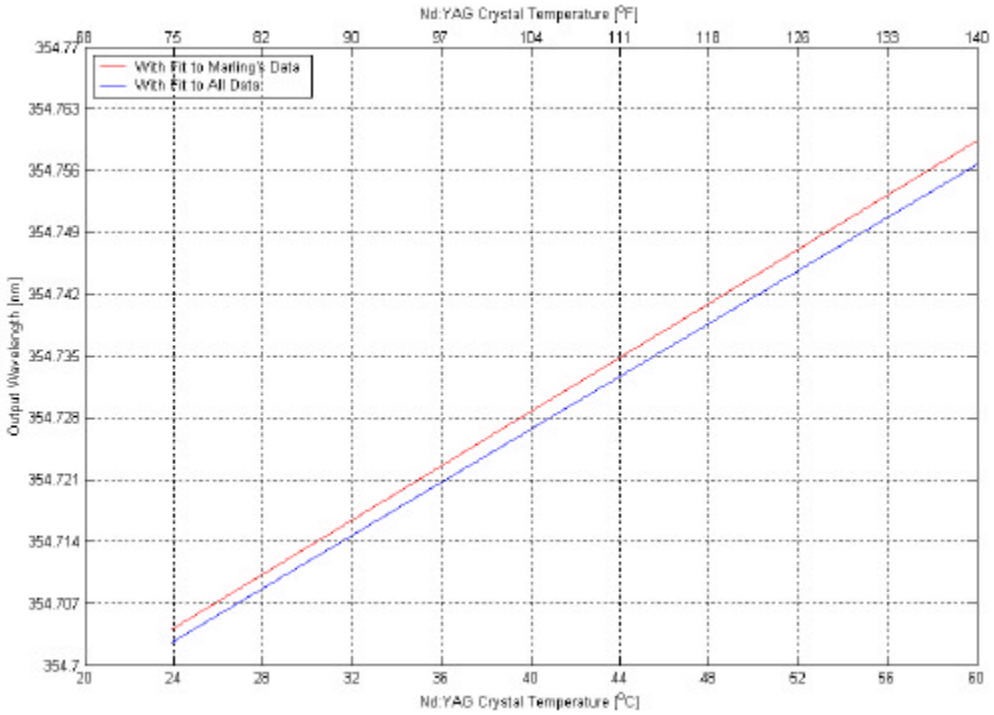

Figure 4.2. Third harmonic wavelength as a function of oscillator rod temperature.

4.2 Theory of Temperature Measurement Using Rotational Raman Spectra

The expected number of backscattered photons calculated with the lidar equation for a rotational Raman lidar channel is given by [Haris, 1995],

$$N_{rot} = \frac{E_L}{E_{p_L}} \Delta z \frac{A_0}{4pz^2} T_{atm}^2(z) n(z) x(z) h_{opt} F(J,T) \qquad 4.1$$

where,

E_L	is the laser energy per pulse [J]
Ep_L	is the energy of a photon at the laser wavelength [J]
? z	is the altitude increment [m]
A_0	is the receiver area [m^2]
z	is the altitude [m]
$T_{atm}(z)$	is the atmospheric transmission at the rotational Raman shifted wavelength [unitless]

n(z)	is the number density [m^{-3}]
$?_{opt}$	is the optical efficiency of the system [unitless]
?(z)	is the telescope form factor [unitless]
J	is the rotational quantum number

and,

$$F(J,T) = \sum_{J} A(J,T)\, filt(J) s_{J \to J'} \qquad 4.2$$

F(J,T) is the probability that a molecule will be in an initial quantum state within the filter spectrum, filt(J), and will backscatter, $\sigma_{J \to J'}$, to the observer. The thermal population distribution of the rotational states, A(J,T), is given by,

$$A(J,T) = \frac{g(J)}{Q(T)} (2J+1) \exp\left[-\frac{E_J}{kT} \right] \qquad 4.3$$

where,

$$E_J = \frac{h^2 J(J+1)}{8p^2 I} = B \cdot h \cdot c \cdot J(J+1) \qquad 4.4$$

and,

$$Q(T) = \frac{(2I+1)^2 kT}{2 \cdot h \cdot c \cdot B} \qquad 4.5$$

and,

g(J)	is the nuclear spin statistical weight factor
E_J	is the energy in the J^{th} quantum state [J]
k	is Boltzmann's constant [J K^{-1}]
T	is the temperature [K]
h	is Planck's constant [J s]
I	is the moment of inertia [kg m^{-2}]
B	is the rotational constant for a particular molecule [cm^{-1}]

c is the speed of light in free space [cm s^{-1}]

The rotational partition function, Q(T), serves to normalize the molecular wavefunction, preserving the probabilistic laws that dictate the population distribution. Of greatest importance to note is that fact that *the number of molecules which will cause backscatter to be received in a rotational Raman Lidar channel is a function of only molecular properties and temperature.* One can project the expected return only if the quantized rotational energy levels and the backscatter cross-sections for the distribution of allowed transitions can be calculated [Haris, 1995]. Quantum selection rules show that the spacing between quantum lines must follow: ? J = 0, ±2. Neglecting centripetal distortion effects on the molecule, (a valid assumption for J ≤ ~500, which it will be in this case), the shift in angular frequency for the Stoke's spectrum is equal to,

$$\Delta w_{J \to J'} = -2B(2J+3) \qquad 4.6$$

and,

$$\Delta w_{J \to J'} = 2B(2J-1) \qquad 4.7$$

for the anti-Stoke's spectrum. Measurements are made only in the anti-Stoke's region of the rotational spectrum, as opposed to the Stoke's region, to avoid fluorescence contamination of the measurement (fluorescence occurs only at redshifted wavelengths).

The backscattering cross-sections of each of the lines can be determined by,

$$s_p = \frac{32p^4}{15} b(J)(w_o + \Delta w_{J \to J'})^4 g^2 \qquad 4.8$$

where,

w_o is the wavenumber of the transmitted laser [cm^{-1}]

$\Delta w_{J \to J'}$ is the wavenumber shift to the J^{th} energy level [cm^{-1}]

γ is the anisotropic invariant of the polarizability tensor [cm^6]

b(J) is the Placzek-Teller coefficient

For linear molecules, such as N_2 and O_2, b(J) is given by,

$$b(J) = \frac{3J(J+1)(J+2)}{2(2J+1)(2J+3)} \quad 4.9$$

for Stoke's scattering and,

$$b(J) = \frac{3J(J-1)}{2(2J+1)(2J-1)} \quad 4.10$$

for anti-Stoke's scattering. Molecular coefficients for calculating backscatter intensity are given in Table 4.1.

Table 4.1. Rotational Raman coefficients for N_2 and O_2 [Haris, 1995].

Coefficient	**N_2**	**O_2**
B	1.9895 ± 0.00002	1.43768 ± 0.00001
g(J) even J	6	0
odd J	3	1
γ^2	$0.518 \cdot 10^{-48}$ ± 8%	$1.35 \cdot 10^{-48}$ ± 10%

An example plot of the effect of atmospheric temperature on back-scattering cross-section is given in Figure 4.3. The figure shows that the backscattering cross-sections of the higher J number lines are much more sensitive to scattering volume temperature than those of the lower J number lines. Also, one can see from examining Eqn. 4.1 that taking the ratio of return signals from two separate rotational Raman lidar channels removes instrument inaccuracies from any measurements made. The combination of these two factors provides the capability of profiling temperature in the lower atmosphere. Once 528/530 channel count ratios have been measured at various heights, the instrument is then calibrated with the theoretical temperature sensitivity curve and verified with a sonde release.

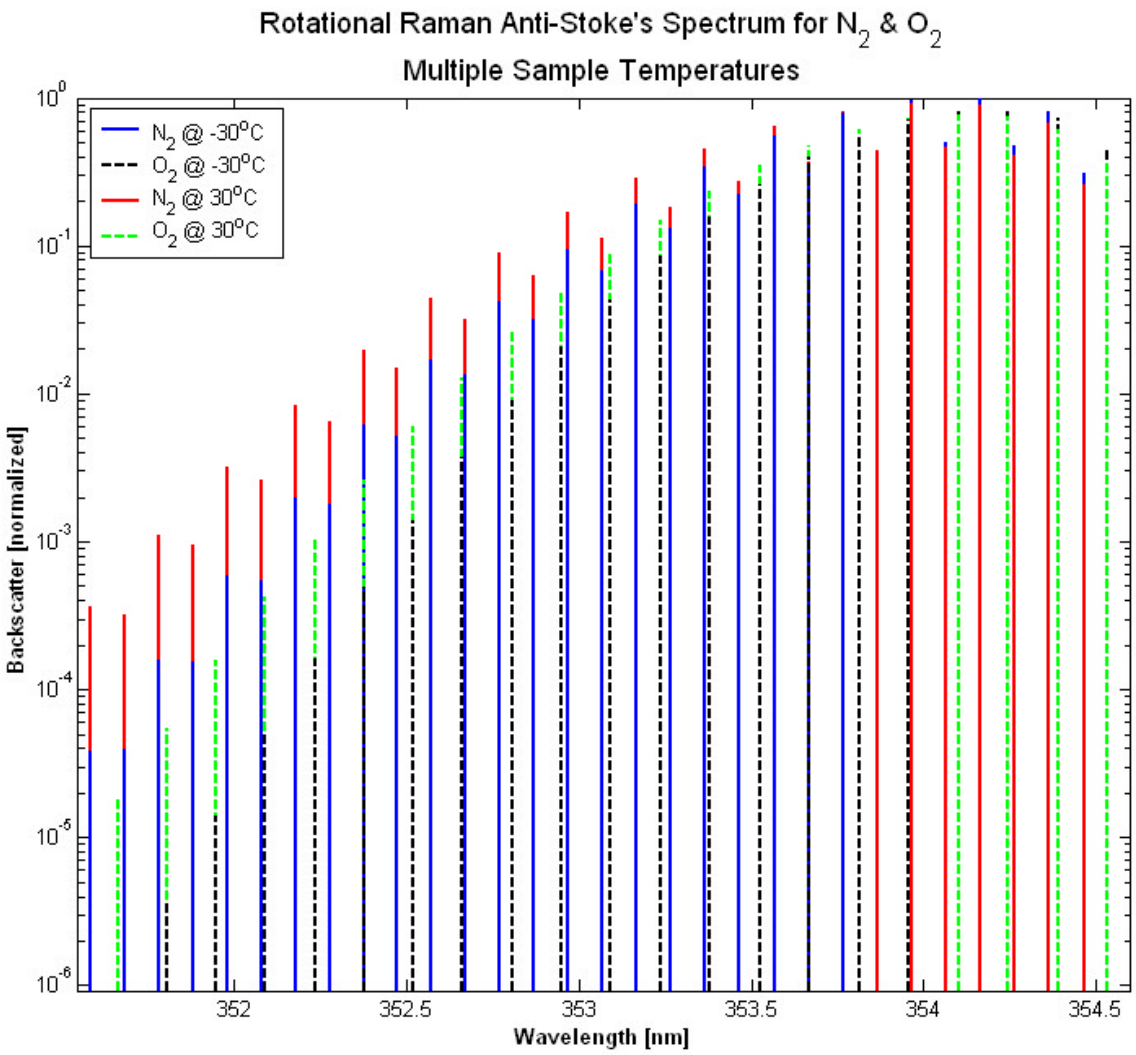

Figure 4.3. Effect of sample temperature on backscattering cross-section for two extremes in atmospheric temperature.

4.3 Verification of Algorithm for Calculating Anti-Stokes Spectra

All calculations done in selecting optimal filter center wavelengths were based on the method discussed in the previous section for determining the rotational energy levels and their respective backscattering cross-sections. Before any further work could take place, it was deemed appropriate to demonstrate the validity of this algorithm. Figure 4.4 shows the experimentally measured pure rotational Raman spectrum of molecular nitrogen [Kroto, 1975]. The central, unshifted peak is the Cabannes line. The intensity alternation for even and odd J is due to the nuclear spin statistical weighting factor. From

Figure 4.4, wavenumber shifts ($\Delta\nu$) corresponding to particular rotational quantum numbers were approximated. To verify that we have correctly calculated the shifted wavenumbers, they were compared to those measured for N_2 by Kroto. A summary of the findings is given in Table 4.2, including differences in shifted wavelengths predicted by the algorithm and those derived from measured wavenumber shifts. It is seen that these differences are quite small, and are most likely due to unavoidable errors made in interpreting Figure 4.4.

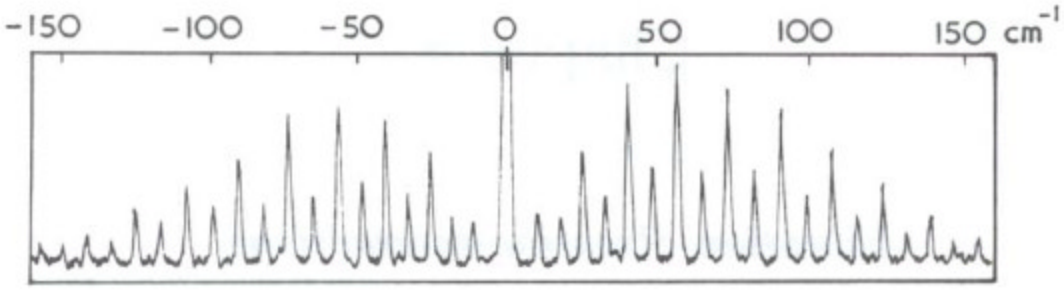

Figure 4.4. Experimentally measured pure rotational Raman spectrum of N_2. Laser excitation wavelength of 632.8 nm [Kroto, 1975].

This same verification process was foregone for O_2 because of the physics of the model. Both N_2 and O_2 are linear rotors, so aside from the molecular rotational constant and a simple statistical weighting function, the algorithms for calculating their anti-Stokes spectra are the same. As is shown in Table 4.1, the rotational constant for O_2 is known to a high degree of accuracy. For purposes of this thesis, this measurement uncertainty produces negligible differences in rotational Raman shifted wavelengths.

Table 4.2. Comparison of calculated rotational Raman shifts of N_2 with those measured by Kroto [1984].

Spectral Region	**Rotational Quantum Number (J)**	Dn **Taken from Figure 4.4 (cm^{-1})**	**Calculated Wavenumber Shift (cm^{-1})**	**Wavelength derived from Measured** Dn **(nm)**	**Calculated Wavelength (nm)**	**Difference (nm)**
anti-Stoke's	0	11.50	11.937	354.5694	354.5639	0.0055
anti-Stoke's	1	19.25	19.895	354.472	354.4639	0.0081
anti-Stoke's	2	30.05	27.853	354.3746	354.3639	0.0107
anti-Stoke's	3	33.55	35.811	354.2648	354.2640	0.0008
Stoke's	0	-11.25	-11.937	354.8556	354.8643	0.0087
Stoke's	1	-19.5	-19.895	354.9595	354.9645	0.0050
Stoke's	2	-27.00	-27.853	355.0540	355.0648	0.0108
Stoke's	3	-33.25	-35.811	355.1329	355.1652	0.0325

4.3 Optimum Narrow-Band Optical Filter Selection

The cumulative theoretical background over the entire optical filter passband is given by [Haris, 1995],

$$N_{Back} = \frac{A_0 h_{opt} T_D 2\Delta z}{c} \int_{l_1}^{l_2} \frac{L(l)\, filt(l)}{E_p(l)}\, dl \qquad 4.11$$

where,

$$T_D = p \sin^2\left(\frac{FS}{2FL}\right) \qquad 4.12$$

and,

L(?)	is the solar radiance [W m^{-1}]
E_p(?)	is the energy of a photon at ? [J]
filt(λ)	is the filter function [unitless]
FS	is the field stop diameter [m]
FL	is the focal length of the telescope [m]
c	is the speed of light in air [m s^{-1}]

Taking the ratio of Equations 4.1 and 4.11, the signal-to-noise ratio is determined to be [Haris, 1995],

$$SNR = \frac{N_{Rot}(z)}{N_{Background}} = \frac{\frac{E_L}{E_{p_L}} \frac{1}{4p \cdot z^2} n(z) T_{atm}^2(z) F(J,T)}{\frac{2T_D}{c} \int_{l_1}^{l_2} \frac{L(l)\, filt(l)}{E_p(l)} dl} \qquad 4.13$$

Calculations using Eqn. 4.13 allow the determination of the expected SNR for returns from particular altitudes. Figure 4.5 shows a plot of atmospheric transmission to various altitudes as a function of wavelength. This plot was produced using PCModTran 4.0. A similar plot of solar radiance can be produced with the same software.

In determining optical filter center wavelengths, the main factors to consider are SNR and sensitivity to atmospheric temperature variations. According to Haris [1995], filters centered on a single pair of N_2 and O_2 lines for daytime operation should be placed at 11.94 cm^{-1} and 107.32 cm^{-1} to give the greatest SNR. For a transmission wavelength of 355 nm, these wavenumber shifts translate to centering filters at 354.5638 nm and 353.3688 nm, respectively. Over the small band of wavelengths in the rotational anti-Stokes spectrum considered for placement of filters, solar radiance and photon energy can be considered constant. Thus, assuming the filter function would be the same shape regardless of center wavelength, looking at Eqn. 4.13 reveals that background noise can also be considered constant. This then leaves intensity of the rotational Raman return signal and temperature sensitivity to channel ratio as the main factors to be considered. A MATLAB program was written to examine both of these design aspects.

A few of the closely-spaced pairs of N_2 and O_2 rotational lines around which the optical filters were considered being centered are shown in Figure 4.6. In reference to the figure, the labels L and R refer to which side of the peak cross section a pair of lines falls on, while subscripts designate a specific pair of lines on a particular side. A subscript of H signifies that the pair was chosen for maximum SNR by Haris, while a subscript of O signifies that a pair was one of two originally chosen for final implementation of the optics used for this thesis. Selecting a typical atmospheric temperature of 10 °C (50 °F) for an altitude of 1.5 km, and taking into account the species relative atmospheric concentrations, a few comparisons can be made. Using the cross- section obtained for the L_H line as a reference, it was determined that the signal intensity decreases by 71% for L_o, 94.6% for L_2 and 97.5% for L_1. However, the signal intensity increases by 66.8%

from R_H to R_o. So, at this atmospheric temperature, an overall decrease in signal intensity of 4.2% is incurred from Haris' original design. Figure 4.7 shows sensitivities to temperature of combinations of the filters shown in Figure 4.6. As can be seen from Figure 4.7, the original filter combination design (L_o and R_o) provides for a much more temperature-sensitive measurement than Haris' original design.

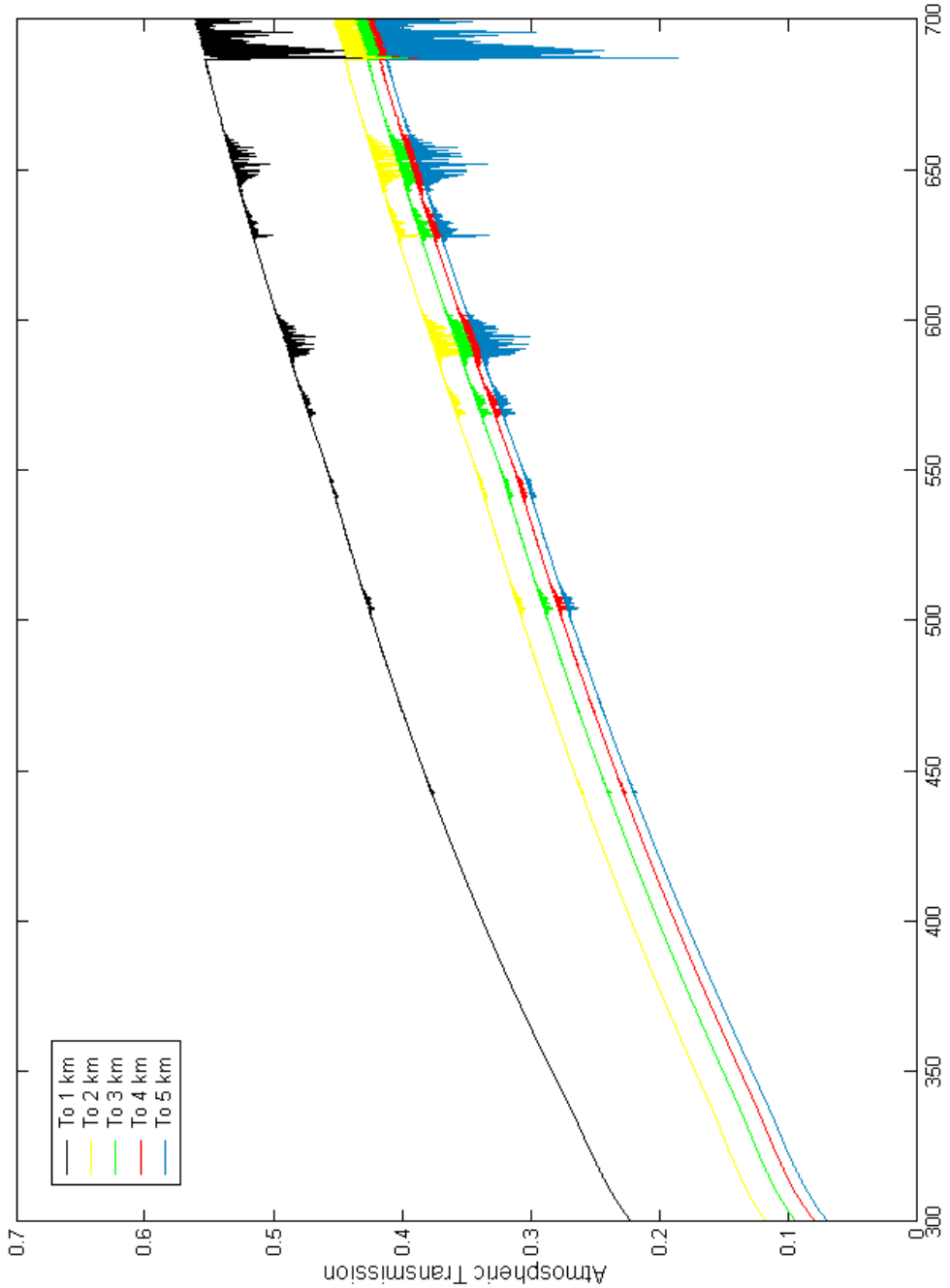

Figure 4.5. Atmospheric transmission from the surface to 1, 2, 3, 4, and 5 km from PCModTran 4.0, assuming 5 km visibility.

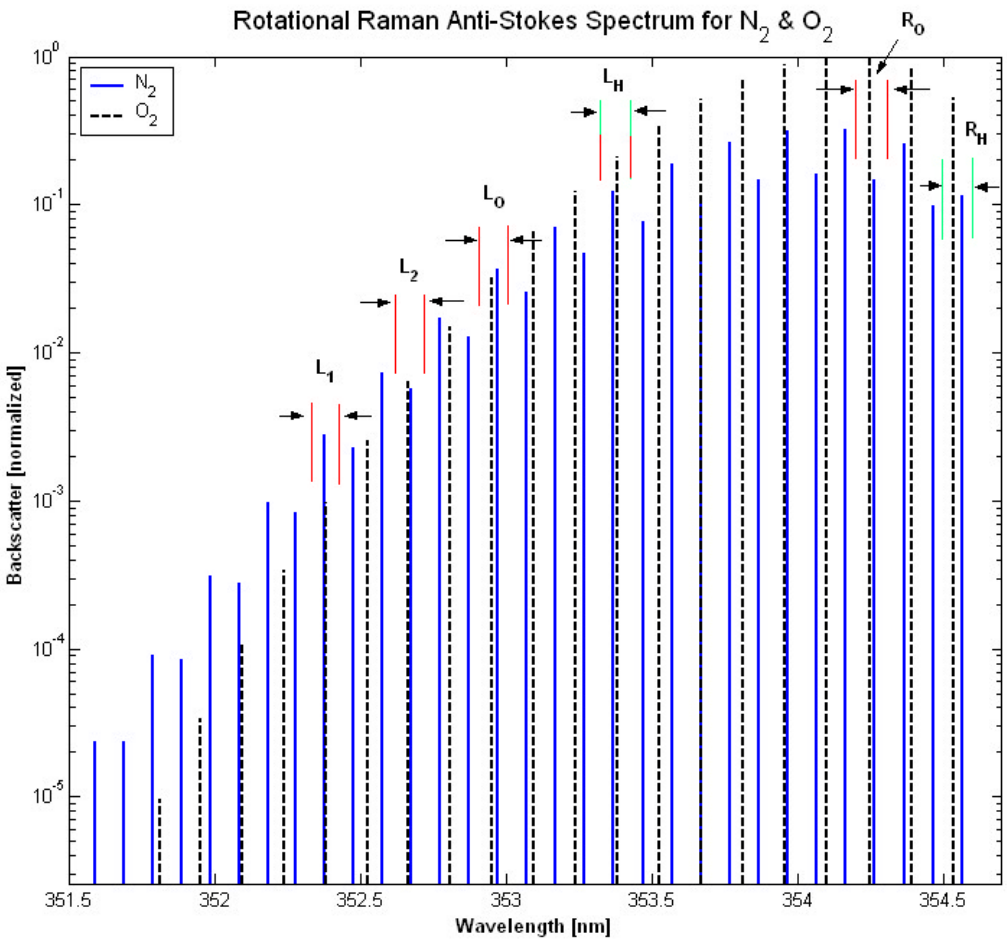

Figure 4.6. Rotational Raman anti-Stokes spectrum of N_2 and O_2 for 355 nm exciting radiation and an arbitrary atmospheric temperature. The figure shows ideal filters (FWHM = 0.1 nm) centered about closely spaced pairs of N_2 and O_2 lines. Species relative atmospheric concentrations not taken into account.

However, an additional requirement of the filtering optics is that they must have an optical density (OD) of greater than OD-8 at the 354.714 nm laser line. Optical density is given as,

$$OD = \log_{10}\left(\frac{1}{T}\right) \qquad 4.14$$

where T is the transmissivity of the filter at a particular wavelength. Hence, the filtering optics must transmit less than 10^{-8} of the signal at the laser line into each photon counting channel. However, conversations with a representative from Barr Associates, the manufacturer of the optical filters, revealed that filter R_o of Figure 4.6 would be much too costly to construct, given this stringent blocking requirement at a separation of only

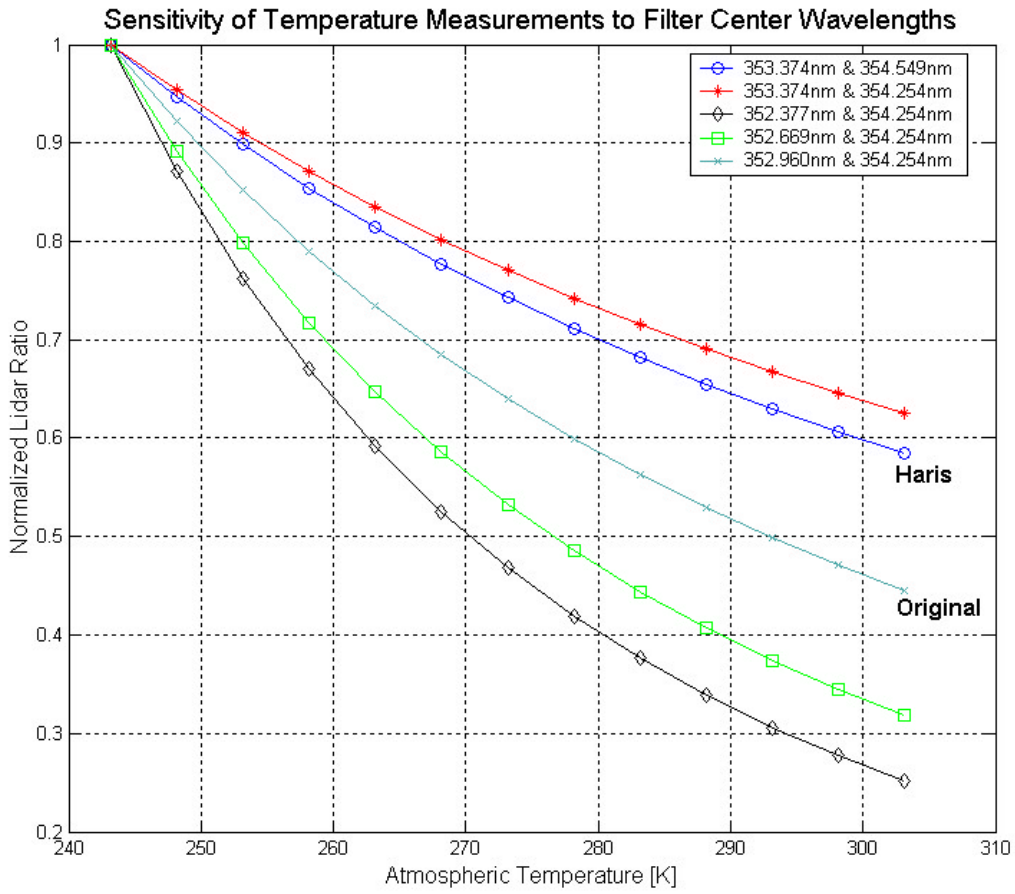

Figure 4.7. Temperature sensitivity using different combinations of filter center wavelengths, including those suggested by Haris [1995]. Species relative atmospheric concentrations were not taken into account.

0.46 nm, or 36.6 wavenumbers from the laser line. So, an alternative center wavelength had to be chosen for the second rotational filter. Given the constraints imposed on the design by the manufacturer, signal intensity and temperature sensitivity were again considered, along with available blocking strength at the laser line, to give the design shown in Figure 4.8. The center wavelength of Filter F_2 was chosen to be 353.79 nm.

The total tolerance given by the manufacturer, taken as the uncertainty in center wavelength (± 0.02 nm) plus the uncertainty in full-width half maximum (FWHM) passband width (± 0.02 nm), is shown in green in the figure. The full specifications for the filters are given in Appendix A. Signal intensity for filter F_2 is increased to 117.3% of the intensity encountered with the original design, R_o. Signal intensity with filter F_2 is also 95.7% higher than Haris' [1995] design, R_H. A comparison of temperature

sensitivities for the original and final filter designs, as well as for Haris' [1995] design is shown in Figure 4.9. Final selected filter center wavelengths are given in Table 4.3. Also shown in Figure 4.9 is the sensitivity of an additionally considered design, having the low J number filter centered at 353.96 nm. As can be seen from the figure, this design would provide greater measurement sensitivity to temperature than the final chosen design. Additionally, this design would give 117.8% of the received signal intensity of the final chosen combination of filters. However, the low J number filter for this design was too costly to purchase, and hence was not opted for in the final filter selections.

It should be further specified that the metal oxide filters to be used are being designed to operate at an ambient temperature of 34º C; the temperature at which the wavelength separation and detection unit is set to maintain internally. Metal oxide filters have a center wavelength dependence on temperature, which varies approximately as 0.0025 nm $^{o}C^{-1}$ [Chadha, 2001]. For this relation to be useful, the manufacturer must specify the temperature at which the filters original transmission and reflection curves were measured, and temperature must be noted when performing ones own measurements.

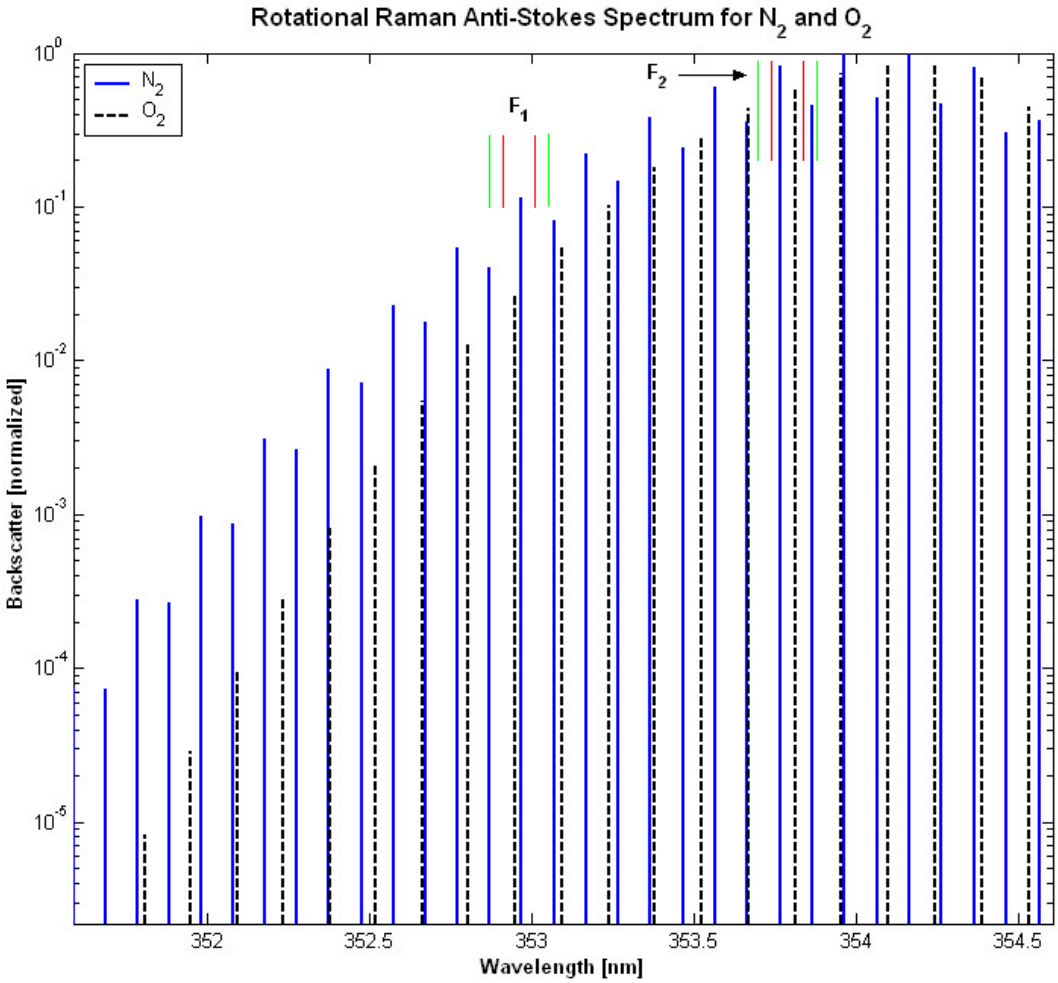

Figure 4.8. Final filter placement at center wavelengths of 352.96 nm and 353.79 nm. Red lines mark FWHM about center wavelength; green lines mark FWHM using maximum tolerance values given by manufacturer. Species relative atmospheric concentrations taken into account.

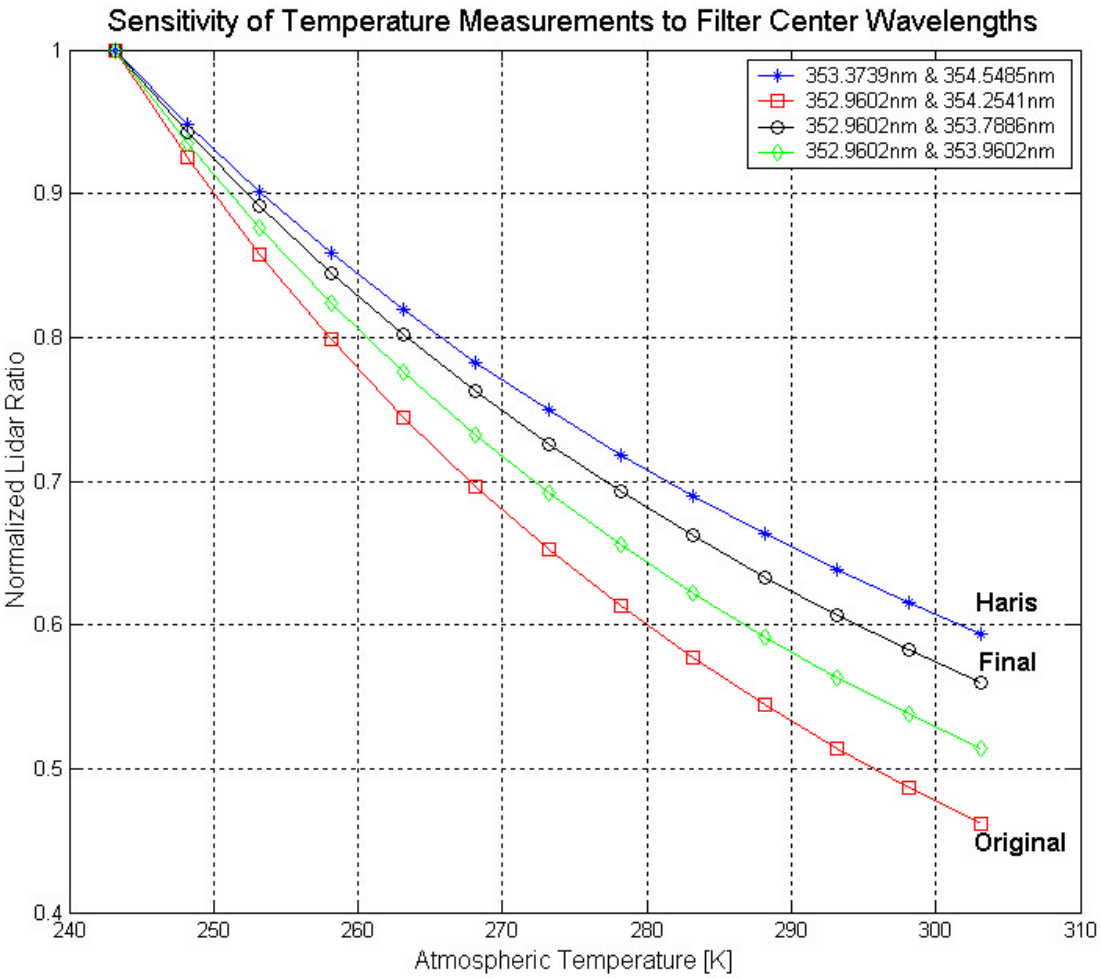

Figure 4.9. Temperautre sensitivities for Haris' [1995] design, along with the original and final designs for this thesis. The sensitivity of an additionally considered filter configuration is also shown. Species relative atmospheric concentrations taken into account.

Table 4.3. Final selected center wavelengths for narrow-band optical filters.

Radiation Source	**Center Wavelength (nm)**	**Wavenumber Shift from Laser Line (cm^{-1})**
Rayleigh backscatter	354.71	0
N_2 – vibrational Raman	386.68	-2330.5
H2O - vibrational Raman	407.50	-3651.8
N_2/O_2 – Rotational Raman	353.79	73.63
N_2/O_2 – Rotational Raman	352.96	140.096

The minimum necessary passband widths of the filters are determined by line broadening, and also the separation distance of the N_2 and O_2 lines in each pair. The primary sources of broadening are the finite linewidth of the transmission and the thermal Doppler effect. The FWHM frequency linewidth induced by thermal Doppler broadening is given by [Measures, 1984],

$$\Delta n = \frac{b\sqrt{\ln 2}}{2p} \qquad 4.15$$

where,

$$b = 2\cdot\sqrt{\frac{2kT\cdot(2p\cdot f_o)^2}{mc^2}} \qquad 4.16$$

and,

k	is Boltzmann's constant [J K^{-1}]
T	is temperature in [K]
f_o	is the exciting laser frequency [Hz]
m	is the mass of the molecule [kg]
c	is the speed of light [m s^{-1}]

Conversion to linewidth in wavelengths can be done using the relation,

$$\Delta l = \frac{l^2}{c}\Delta n \qquad 4.17$$

where λ is the exciting laser wavelength.

Table 4.3 gives the bandpass widths necessary to isolate the chosen pairs of N_2 and O_2 lines. As can be seen from the table, the necessary filter passband widths fit just within those of the filters specified for purchase. Additionally, it should be noted that the FWHM broadening contributed by the transmitter 3rd harmonic was originally believed to be 1/3 of the fundamental linewidth, or 1/3 cm^{-1} (0.034 nm), but recently it was discovered to be 1.5 cm^{-1} (0.0377 nm).

Table 4.4. Narrow-band filter constraints for isolating chosen N_2 and O_2 line pairs.

Filter	**Center** l **(nm)**	**Laser FWHM (GHz)**	**Laser FWHM (nm)**	**N_2 FWHM (GHz)**	**N_2 FWHM (nm)**	**O_2 FWHM (GHz)**	**O_2 FWHM (nm)**	**Inter-pair distance**	**Min. FWHM (nm)**
F_1	352.96	89.94	0.0377	1.991	0.00084	0.6	1.86	0.02	0.059
F_2	353.79	89.94	0.0377	1.991	0.00084	0.6	1.86	0.047	0.086

Chapter 5 - PROPOSED INSTRUMENT SETUP

5.1 Transmission Optics

For the temperature measurement experiment described in this thesis, the only differences in the transmission optics from normal operation will be

1.) Replacement of a 4th harmonic generator (FHG) with a 3rd harmonic generator (THG)
2.) Remove dichroic beamsplitter (reflects 1064 nm and transmits 532 nm) normally used to remove the 1064 nm wavelength from the beampath
3.) Replace the 266 nm wideband filter with a 355 nm wideband filter.
4.) Replace mirror in beam expander with proper optical coating

A photograph of the transmission optics setup is shown in Figure 2.1. The reason for the removal of the dichroic beamsplitter is that the 1064 nm wavelength is necessary to produce both the 355 nm wavelength and 532 nm wavelength. Only the 532 nm wavelength is necessary to produce the 266 nm wavelength. Without getting too detailed, the processes behind third-harmonic generation is three-wave mixing, respectively. In three-wave mixing, three electromagnetic waves, each oscillating at its own frequency (? $_1$, ? $_2$, ? $_3$) within a birefringent medium (the crystals in the harmonic generators), combine to produce an output wave at another frequency, for example mixing of 1064 nm and 532 nm to produce 355 nm. In the case of FHG, ? $_1$ = ? $_2$ = ? = $2 \cdot p \cdot c$ / 532 [nm], and the output wave ? $_3$ = 2? , twice the second-harmonic frequency, or the fourth harmonic of the fundamental at 1064 nm. The process of four-wave mixing entails the coupling of three waves of frequency ? $_1$, ? $_2$, and ? $_3$ to produce a fourth wave of frequency ? $_4$. As is possible in the three-wave mixing process, the induced wave can have a frequency equal to the sum of the incident wave frequencies. In this case, ? $_4$ = ? $_1$ + ? $_2$ + ? $_3$ = $2 \cdot p \cdot c$ / 1064 [nm]. This is called *third-harmonic generation* (THG) or frequency tripling [Milonni, 1988].

5.2 Detection Optics

The physical layout of the detector will be the same as that typically used for measurements done with LAPS. However, three of the beamsplitting optics will be replaced and the new narrow-band filters inserted into the channels already used for UV returns. Theoretical data for these optics are given in Appendix A. The arrangement given here was chosen to avoid the need to switch the PMT physical locations, which is not a trivial task. A diagram of input signal separation into specific channels is given in Figure 5.1, and a photograph of the detector layout is given in Figure 5.2. Table 5.1 lists the optics to be used in the detector, as referenced to these two figures. Just prior to the PMTs, additional optics will also be inserted in each of the two new rotational Raman channels to assist with laser line and out-of-band blocking. These optics are listed in Table A.2 as items 4 and 5.

Table 5.1. List of optical components, as referred to Figures 5.1 and 5.2.

Part Number	Specification Sheet Location	Description
1	Table A.3	Longpass Filter T > 80% @ 528 nm R > 80% @ 408 nm
2	Table A.2, Item 2	Shortpass Filter T > 70% @ 354 nm R > 80% @ 408 nm
3	Table A.2, Item 3	Beamsplitter 50% / 50%
4	Currently in detector box	Beamsplitter R = 532,528,530 nm T = 660, 607 nm
5	Currently in detector box	Beamsplitter R = 70% ; T = 30%
6	Currently in detector box	Beamsplitter R = 660 nm ; T = 607 nm

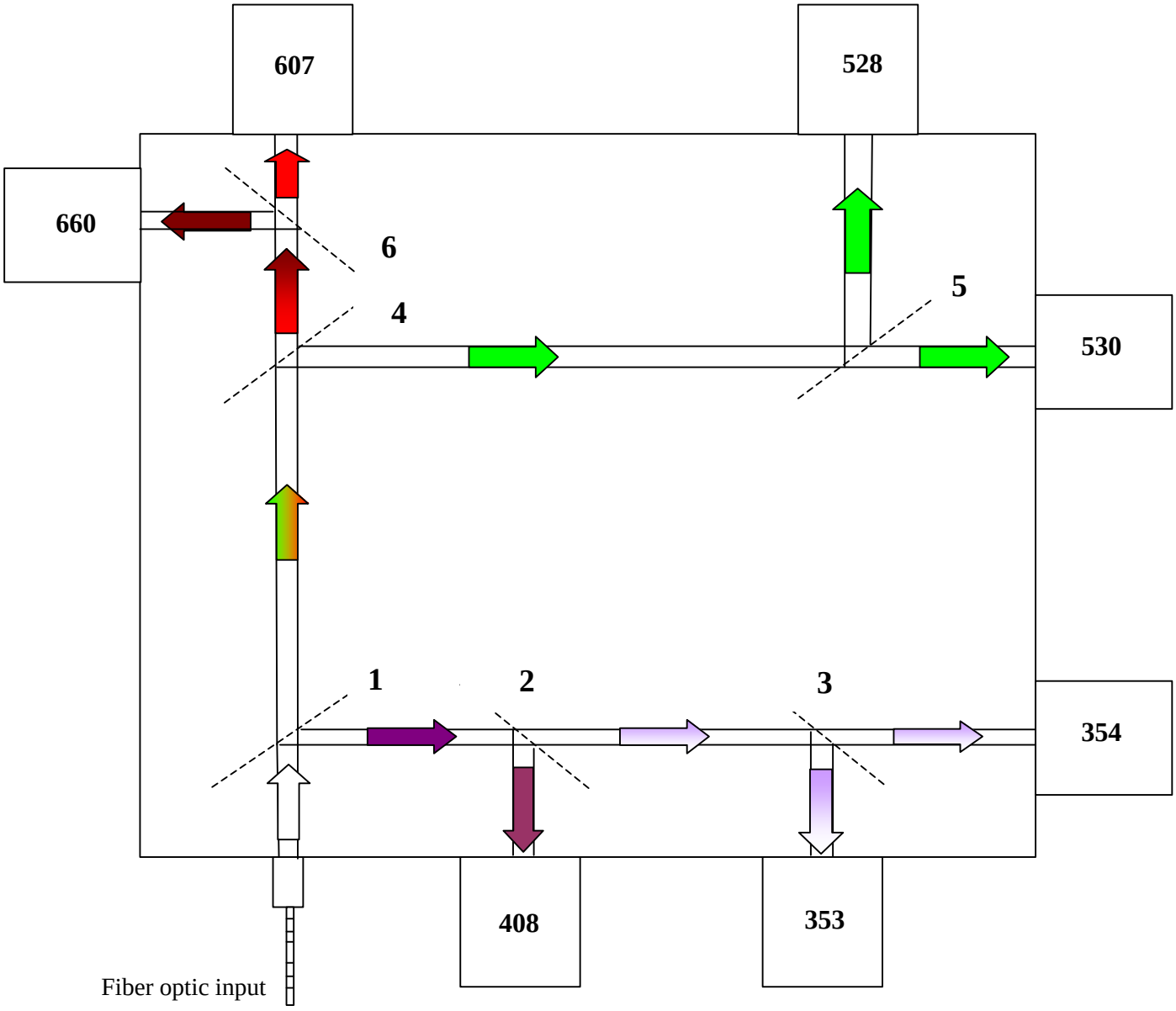

Figure 5.1. Test configuration for optical separation and detection subsystem.

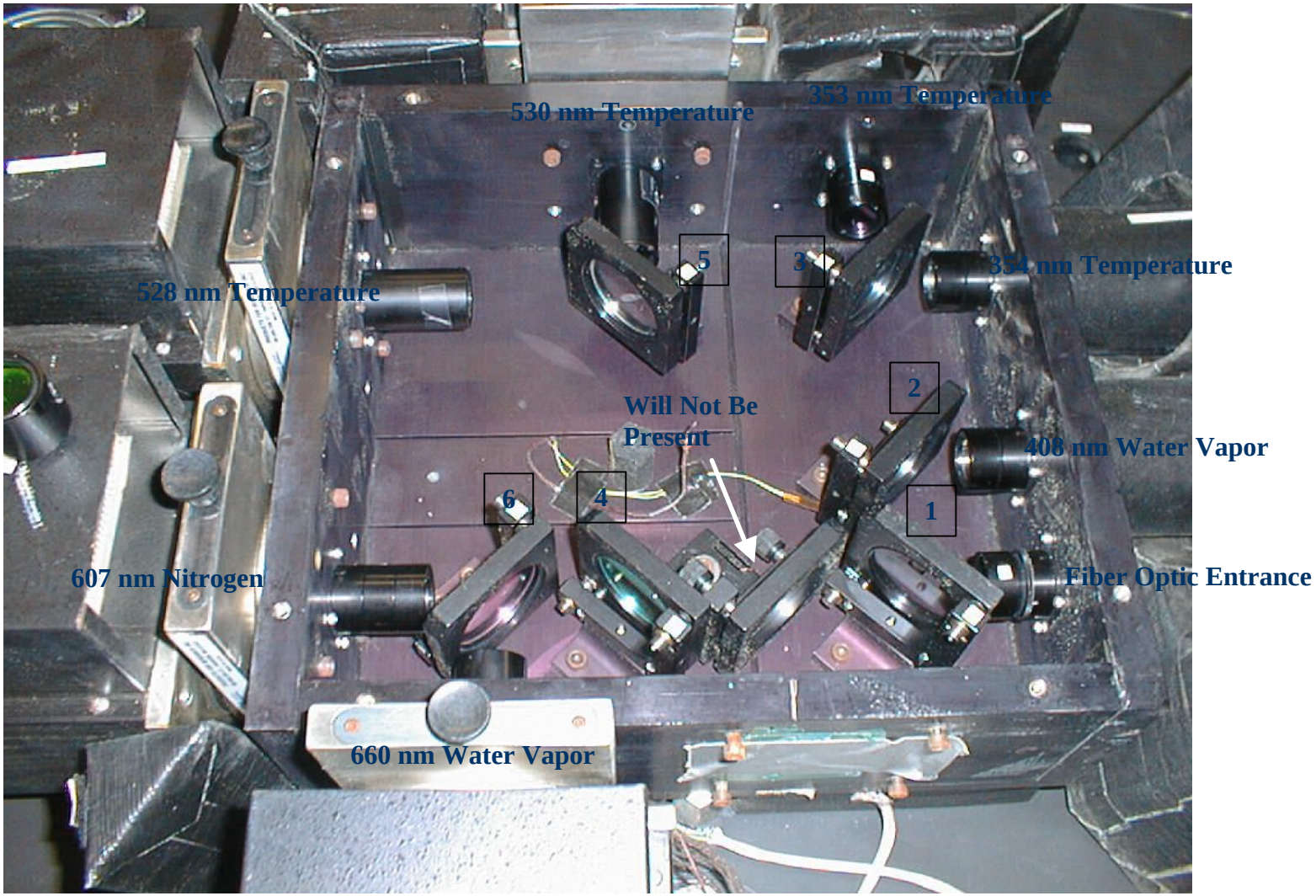

Figure 5.2. Optical detector box layout (photo credit, C.R. Philbrick).

Another modification will come in the calculation of water vapor during initial testing. To simultaneously measure all of the properties listed in Table 2.3, eight channels would be needed. However, only seven channels are available in the detector. To resolve this problem, the 387 nm vibrational return from N_2 produced with the 355 nm transmission will not be used for testing. Instead, the ratio of the 408 nm vibrational return from H_2O and 353 nm rotational return from N_2 and O_2 will be used to replace the intended 408/387 ratio. A comparison of this methodology for calculating water vapor concentration using the visible channel returns is shown in Figure 5.3 for data taken aboard the USNS Sumner in September 1996. As can be seen from the figure, the test method for determining water vapor has a larger error at higher altitudes, however it should provide useful data over a sufficient range for initial proof of concept.

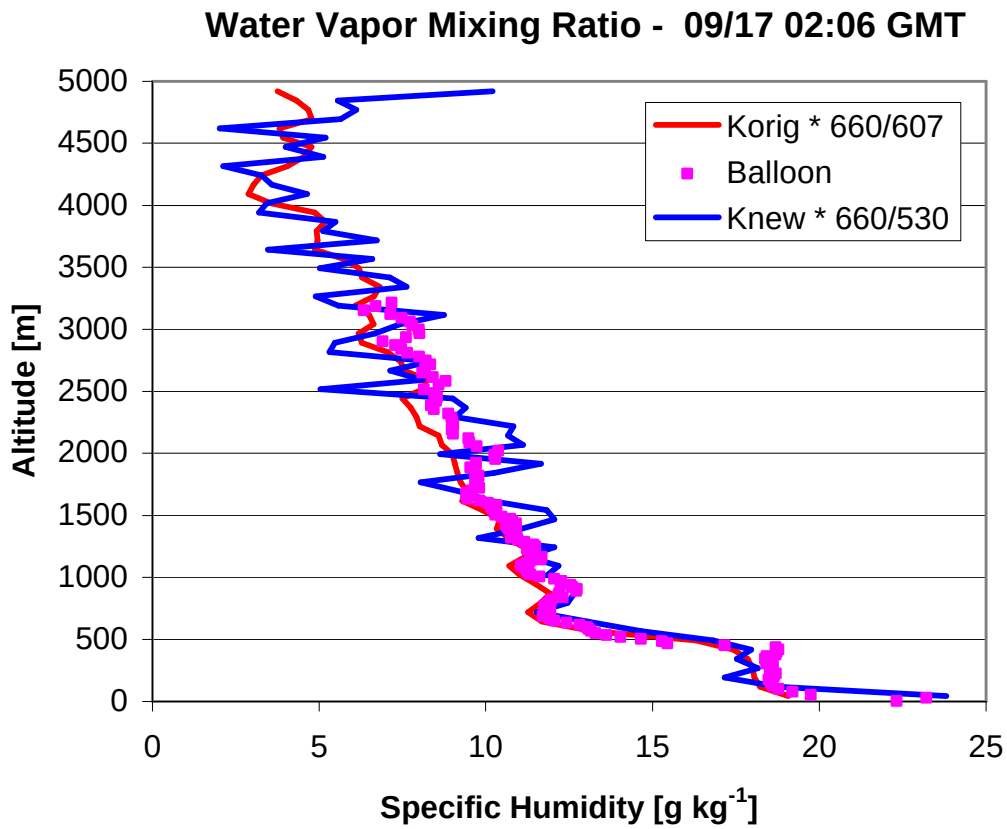

Figure 5.3. Comparison of water vapor measurements using ratios relative to vibrational N_2 return and to rotational return from combination of N_2 and O_2.

Chapter 6 - REGRESSION ANALYSIS OF LIDAR TEMPERATURE DATA

6.1 Correction to NE-OPS 2001 LAPS Temperature Data

In preparation for taking measurements using the 355 nm transmission, a concern that arose during the NE-OPS 2001 study was examined. Temperature profiles derived from processing LAPS data, as it is typically done, showed great variation compared to sonde profiles made near LAPS. Initially, it was suspected that the reason for this was the center wavelengths of the narrow-band filters used in the 528 nm and 530 nm detector temperature channels had shifted, and it was discovered that the filter center wavelengths had in fact shifted (plots of which are shown in Appendix C). However, this was proven not to be a significant problem with the temperature data.

An example of measured LAPS temperature channel return ratios (TCRRs) and the theoretical temperature sensitivity curve (TTSC) for the system are shown in Figure 6.1(c) and (d), respectively. As can be seen from the figure, the trend in the 528/530 ratio is to increase with temperature, see Figure 6.1(a) and (b). The exact opposite trend of a decreasing ratio with temperature was initially observed however. This observation lead to the conclusion that the 528 nm and 530 nm data channels had been switched for one-another at some point during the preparation for the 2001 campaign. At this point, it seems that for the NE-OPS 2001 campaign, either the photon counts from the 528 and 530 channels are logged in reverse order in the raw data files (due to software changes that were being made at the time), or the filter tubes for the 528 nm and 530 nm channels were switched during a calibration run before the start of the study. In either event, simply taking the inverse of the TCRR in the DataProduct.cpp file used with the LapsProcessor program seems to solve the problem. Consequently, the C++ processing software should be modified in the aforementioned manner when processing NE-OPS 2001 data. Figure 6.2 shows the results of calibrating LAPS with a sonde release near the beginning of the 2001 campaign, and Figure 6.3 shows the degree to which the instrument calibration had deteriorated three weeks later. As can be seen from comparing Figures 6.2 and 6.3(b), LAPS temperature measurements do not coincide with

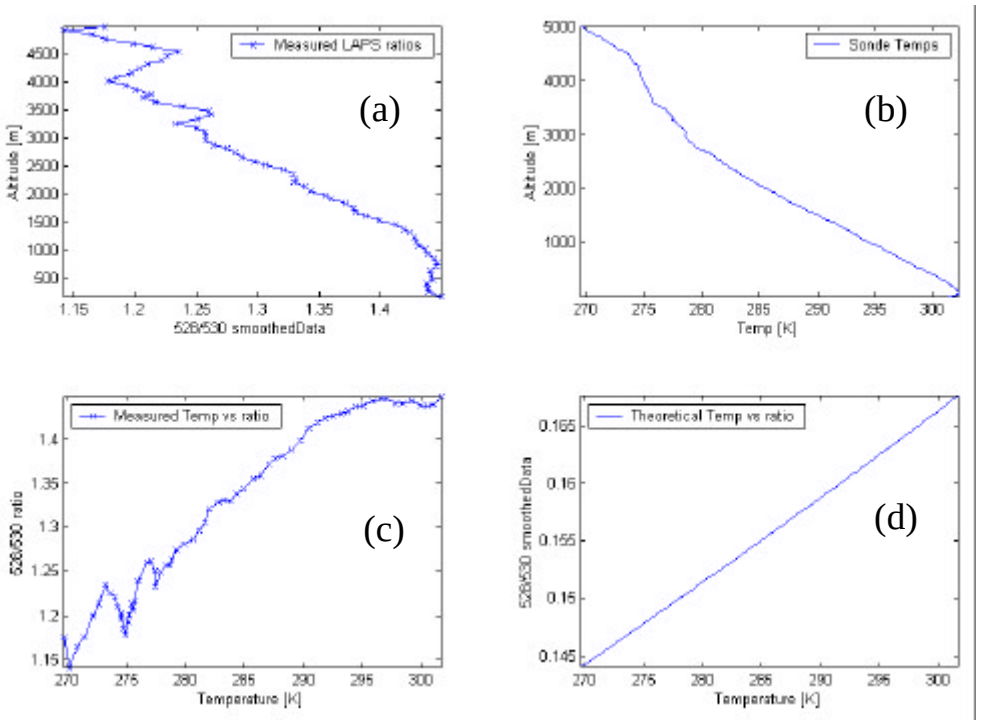

Figure 6.1. Measured lidar returns and calibration bases for the integration period: 10 JUL 2001, 2:19 – 2:32 UTC. (a) and (c) smoothed using 3-point moving average.

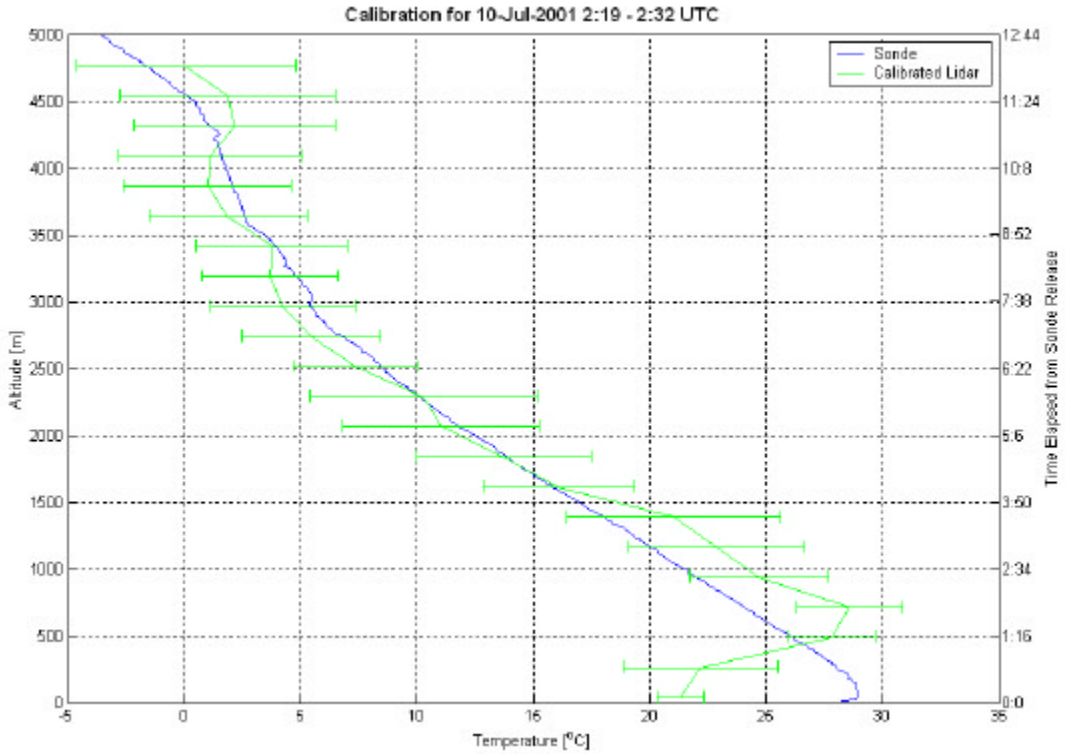

Figure 6.2. Comparison of sonde temperature profile and calibrated lidar for 10 JUL 2001, 2:19 – 2:32 UTC (5-point Hanning filter applied; no vignetting correction).

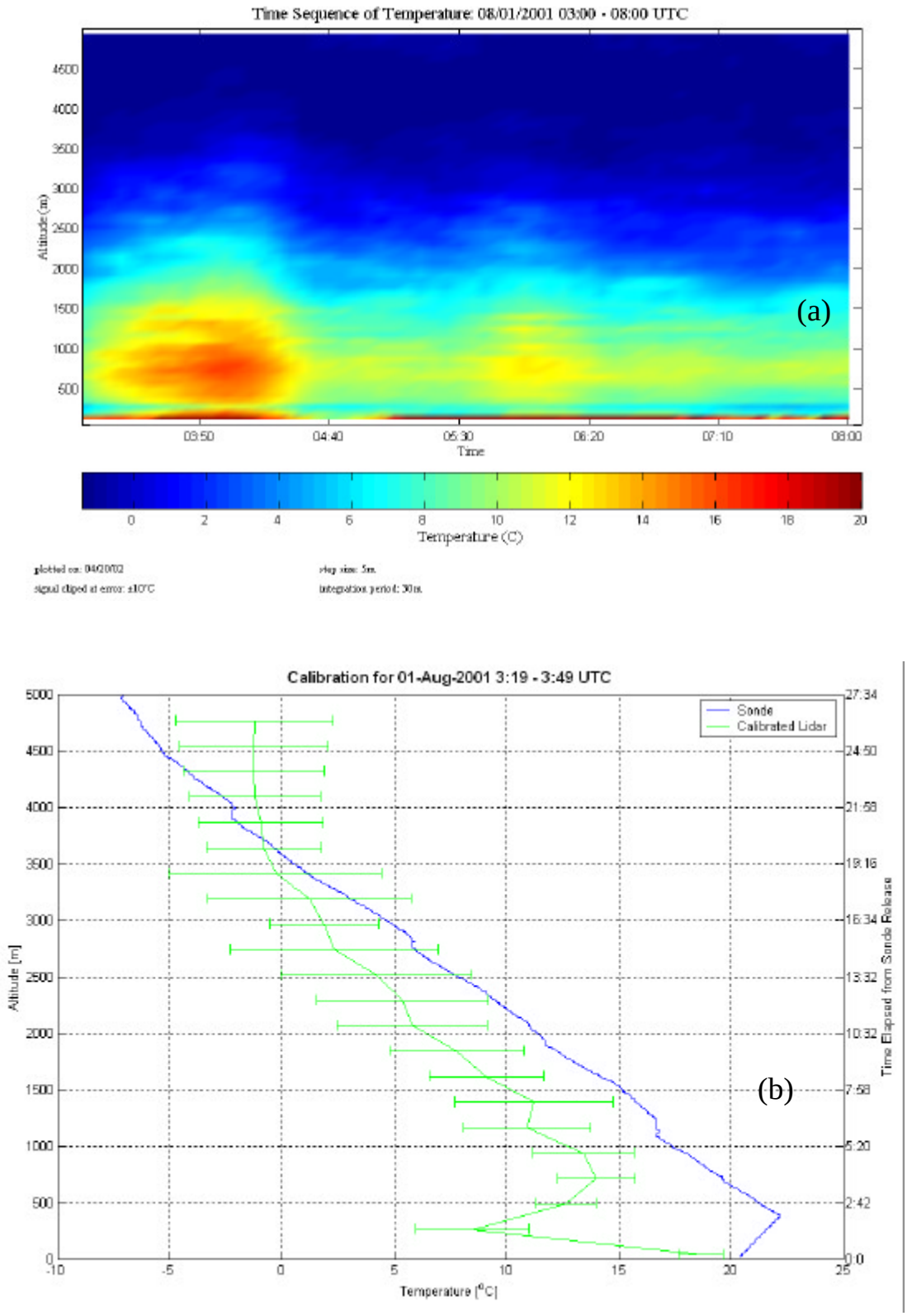

Figure 6.3. (a) Time sequence of temperature for the time period 1 AUG 2001, 03:19 – 08:00 UTC. (b) Radiosonde temperature measurements for the time period 08/01/2001, 03:19 – 03:49 UTC (5-point Hanning filter applied; no vignetting correction).

those of the sonde as well as when the calibration was initially done. This is possibly due in part to atmospheric variations.

6.2 Comparison of Regression Techniques

The calibration method typically used for measuring atmospheric temperature with pure rotational Raman lidar is a least-squares fit of the TCRRs to a measured vertical profile of temperature recorded using a radiosonde. In an attempt to provide measurements accurate over a wider range of altitudes, and hence wider temperature range, the outcome of calibrating the instrument using an alternate method was examined. Haris determined that for the data he used, either a non-weighted polynomial, relating TCRRs to ballon temperatures, or a non-weighted linear relation between the TTSC and the TCRRs and balloon data, provided the best results [1995]. Vaughn et al. [1993] have made temperature measurements using calibration with a temperature sensitivity curve. However, their instrument was calibrated *in situ* using light from a stabilized quartz-halogen lamp and a monochromator. Effectively, they created a look-up table of the ratio of powers in the two rotational Raman channels as a function of temperature, or a *measured* temperature sensitivity curve. Here, the intention is not to perform this calibration measurement, but to calculate the TTSC from the molecular constants of N_2 and O_2, the filter functions, temperature effects on optical components, and varying optical signal attenuations in the receiver and detector. A MATLAB program written for this purpose is given in Appendix B.

LAPS TCRR measurements and temperature measurement calibration bases are shown in Figure 6.1. In the typical calibration scheme, the curve shown in Figure 6.1(a) is fitted to that in (b). The results of this process are shown in Figure 6.4. Regression fits of the curve shown in Figure 6.1(c) to that in (d) (measured TCRR to theoretical TCRR) result in the curves represented in Figure 6.5.

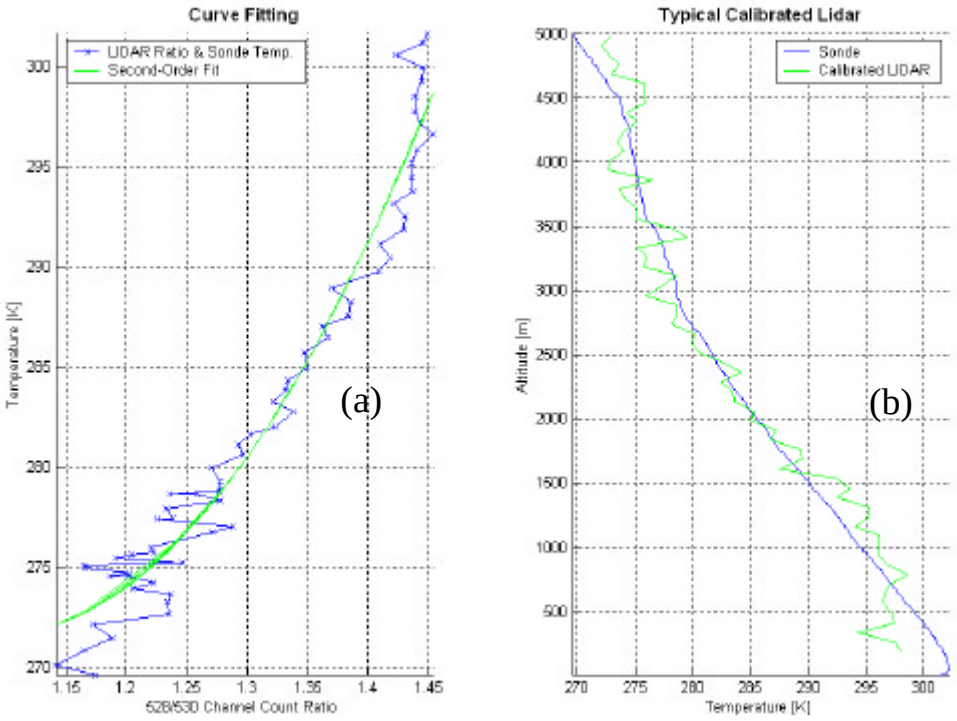

Figure 6.4. Typical second-order polynomial fit of 528/530 channel ratio to measured sonde temperatures. Integration period: 10 JUL 2001, 2:09 – 2:39.

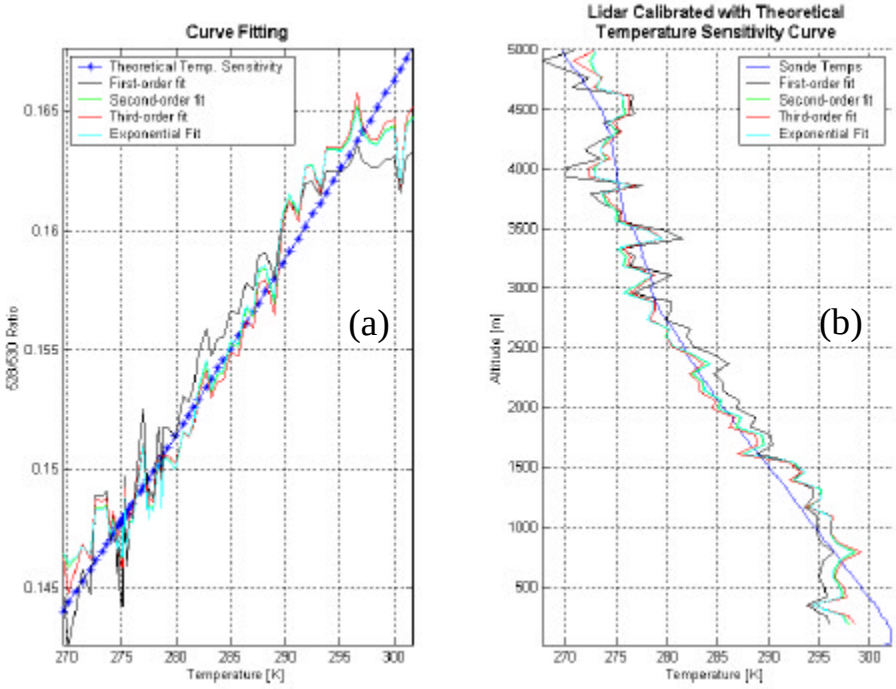

Figure 6.5. (a) Various regression fits of lidar temperature channel ratios to theoretical temperature sensitivity curve, and (b) Comparison of calibrated lidar and sonde temperature profiles. Integration period: 10 JUL 2001, 2:09 – 2:39 UTC.

Examining Figure 6.6 shows no visible improvement in calibration for the fit to the TTSC. In fact, the two calibration methods examined produce nearly identical results.

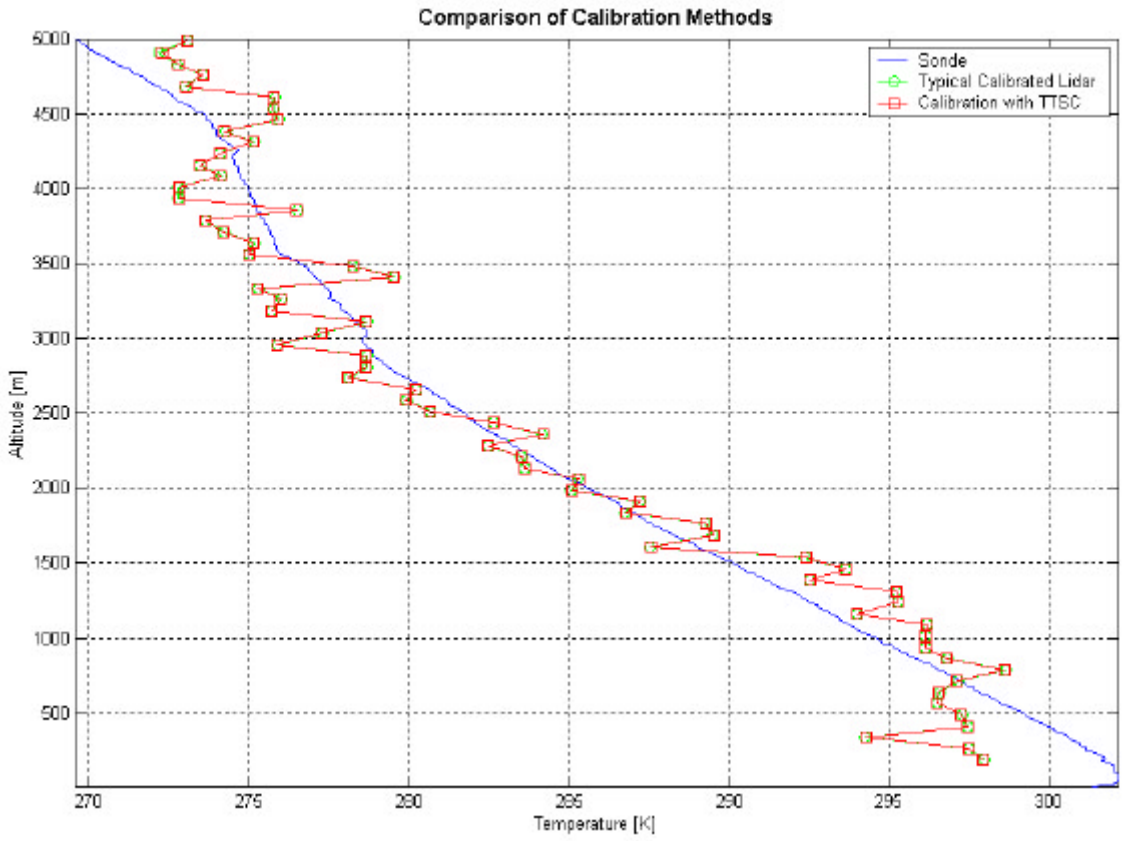

Figure 6.6. Comparison of lidar calibrated using typical method and fit to theoretical temperature sensitivity curve. Integration period: 10 JUL 2001, 2:09 – 2:39 UTC.

As can be seen from Figure 6.1, the TCRR decreases with altitude. All calibrated lidar curves shown in Figure 6.6 show a pronounced deviation from the TTSC at lower altitudes (at higher temperatures in the TTSC fit curves). Vignetting effects appear in measurements made with LAPS below approximately 800 m, due to the fiber optic end field stop in the telescope being overfilled by the return signal below this altitude. It has also been suggested that incomplete mode mixing in the fiber optic transfer is the cause of some attenuation. As a result of these effects, the received signal power is markedly reduced below 800 m. It is possible to achieve a better fit at low altitudes by incorporating these effects into the calibration scheme. Comparisons of received counts measured and predicted by theory in the 528 nm and 530 nm channels are given in Figure

6.7(a) and (b), respectively. The relatively constant difference in magnitude between the expected and measured counts is attributed to inaccuracies in estimation of various attenuations encountered by the optical signal through the entire receiver system. However, attention should be focused mainly on the deviation in *trends* of received counts below 800 m. Tables 6.1 and 6.2 give values for the factors contributing to a few of the theoretical data points shown in Figure 6.7(a) and (b). Volume backscattering coefficient, ß, was unable to be displayed due to machine precision. In calculating the volume backscattering coefficient, values of the measured filter functions were multiplied with the relative backscattering cross-sections encountered for corresponding rotational Raman-shifted spectral line positions. These values were then multiplied with the atmospheric number density corresponding to the altitude from which the backscatter was received. This process was done separately for N_2 and O_2. The magnitudes of the volume backscattering coefficients for both molecules over each filter passband were then summed in the last step.

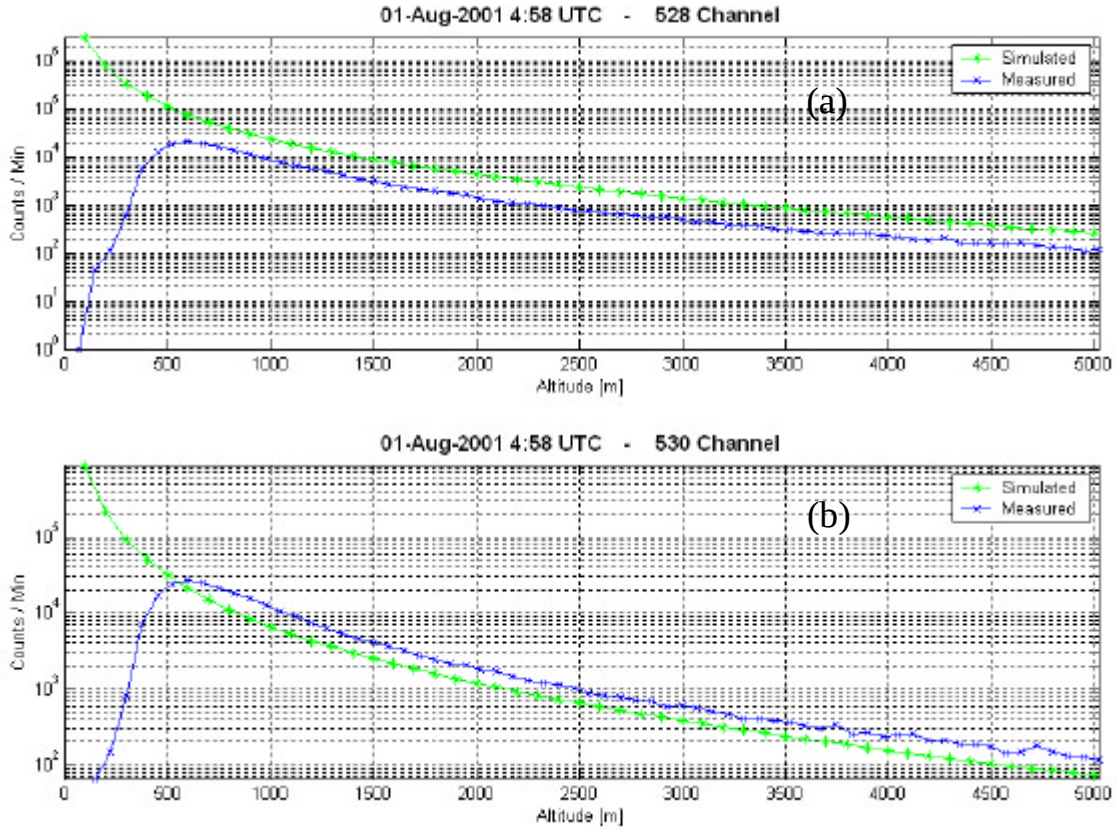

Figure 6.7. Effect of telescope form factor on the number of counts received in the 528 nm and 530 nm channels (50 km visibility assumed).

Table 6.1. Elements of the lidar equation (Eqn. 2.1) used in constructing Figure 6.7(a).

P_T [W]	?(T) [unitless]	?(R) [unitless]	c [m s^{-1}]	t [ns]	A [m^2]	z [m]	ß [m^{-1}]	a [m^{-1}]	Received photon counts
1440	0.9703	0.0422	$3 \cdot 10^8$	500	1.169	1000	----	$8.4 \cdot 10^{-5}$	23851
1440	0.9703	0.0422	$3 \cdot 10^8$	500	1.169	2000	----	$8.4 \cdot 10^{-5}$	4314
1440	0.9703	0.0422	$3 \cdot 10^8$	500	1.169	3000	----	$8.4 \cdot 10^{-5}$	1387
1440	0.9703	0.0422	$3 \cdot 10^8$	500	1.169	4000	----	$8.4 \cdot 10^{-5}$	564
1440	0.9703	0.0422	$3 \cdot 10^8$	500	1.169	5000	----	$8.4 \cdot 10^{-5}$	261

Table 6.2. Elements of the lidar equation (Eqn. 2.1) used in constructing Figure 6.7(b).

P_T [W]	?(T) [unitless]	?(R) [unitless]	c [m s^{-1}]	t [ns]	A [m^2]	z [m]	ß [m^{-1}]	a [m^{-1}]	Received photon counts
1440	0.9703	0.0045	$3 \cdot 10^8$	500	1.169	1000	----	$8.4 \cdot 10^{-5}$	65997
1440	0.9703	0.0045	$3 \cdot 10^8$	500	1.169	2000	----	$8.4 \cdot 10^{-5}$	11937
1440	0.9703	0.0045	$3 \cdot 10^8$	500	1.169	3000	----	$8.4 \cdot 10^{-5}$	3838
1440	0.9703	0.0045	$3 \cdot 10^8$	500	1.169	4000	----	$8.4 \cdot 10^{-5}$	1562
1440	0.9703	0.0045	$3 \cdot 10^8$	500	1.169	5000	----	$8.4 \cdot 10^{-5}$	723

Chapter 7 - CONCLUSIONS AND FUTURE WORK

The capability of the LAPS instrument to measure lower tropospheric properties contributing to RF refractivity, and hence electromagnetic ducting conditions, has been proven repeatedly over the period 1996-2002. As a step toward production lidar instruments, such as ALAPS, a method of safely and discretely obtaining profiles of atmospheric temperature has been presented in this thesis.

An attempt to accurately predict the output wavelength of the LAPS transmitter was made. Under reasonable operating system parameter assumptions, it was shown that for the optical filter FWHM values selected in this thesis, the uncertainty in transmission wavelength by itself is negligible. Narrow-band optical filters were then selected for isolating two portions of the rotational Raman anti-Stoke's spectrum of N_2 and O_2, based on the calculated transmission wavelength. The filters selected are centered at 28265 cm^{-1} (353.79 nm) and 28332 cm^{-1} (352.96 nm). Centering the low rotational quantum number filter at 28228 cm^{-1} (354.254 nm) would make possible improved temperature sensitivity by increasing the separation between the high and low rotational quantum number filters, while still providing high intensity in the return signal.

For measuring atmospheric temperature and water vapor concentration using the output of the frequency-tripled LAPS Nd:YAG laser, the proposed setup modifications to the transmitter and detector were outlined. Hardware specifications were given for a design that should work as an initial proof of concept for an eye-safe, ultraviolet lidar system capable of providing vertical profiles of atmospheric RF refractivity. However, one additional aspect of the transmitter will need to be considered before implementation, and that is how to deal with the residual 1.06 μm transmission that will be incident on the mirrors in the beam expander telescope. These mirrors were not be intended for use at 1.06 μm, hence this wavelength may need to be removed from the beam prior to it entering the beam expander.

A comparison of regression techniques used to calibrate temperature measurements with LAPS has also been presented. It was shown that no improvement in measurement accuracy is gained by calibrating the instrument with the theoretical

temperature sensitivity curve instead of with a radiosonde temperature profile, however the technique is preferred for extension over a wider temperature range. Due to beamsplitter reflection and transmission percentages typical dependence upon polarization of the incident beam, uneven division of the signal intensity as the light passes through the detector box may be enocuntered [Vaughn et al., 1993]. As a result, more precise fitting to both the sonde profiles and the theoretical temperature sensitivity curve may be possible if effects of laser transmitter polarization and depolarization ratio of Raman scattering are considered in analyses of the detector design.

References

Achey, Alexander D., “Design of an Upgraded Electronics Control System for an Advanced Lidar Atmospheric Profiling System,” Master of Science Thesis for Penn State University, Department of Computer Engineering, May, 2002.

Arshinov, Yu. F., S. M. Bobrovnikov,Vladimir E. Zuev,and V. M. Mitev, “Atmospheric temperature measurements using a pure rotational Raman lidar,” Applied Optics, Vol. 22 Issue 19, Page 2984, October 1983.

Atkins, Peter W., *Physical Chemistry*, New York: Freeman, 2000.

Balsiger, F., P.A.T. Haris, and C.R. Philbrick, “Lower tropospheric temperature measurement using a rotatinal Raman lidar,” Proceedings of the SPIE Optical Instruments for Weather Forecasting Conference, vol. 2832, pp. 53-60, 1996.

Behrendt, Andreas and Jens Reichardt, “Atmospheric Temperature Profiling in the Presence of Clouds with a Pure Rotational Raman Lidar by Use of an Interference-Filter-Based Polychromator,” Journal of Applied Optics, Vol. 39, No. 9, pp. 1372-1378, March 2000.

Chadha, Ginnipal S., “Optical Design for Advanced Lidar Detectors,” Master of Science Thesis for Penn State University, Department of Electrical Engineering, May, 2001.

Cohen, Ariel, John A. Cooney, and Kenneth N. Geller, “Atmospheric temperature profiles from lidar measurements of rotational Raman and elastic scattering,” Applied Optics, Vol. 15 Issue 11, Page 2896, November 1976.

Continuum Laser Corporation, Powerlite 9000 specification sheet.

Cooney, John A., “Measurement of atmospheric temperature profiles by Raman backscatter,” Journal of Applied Meteorology, Vol. 11, pp. 108-112, 1972.

Cooney, John A., and Madeline Pina, “Laser radar measurements of atmospheric temperature profiles by use of Raman rotational backscatter,” Applied Optics, Vol. 15 Issue 3, Page 602, March 1976.

Esposito, Steven T., “Applications and analysis of Raman lidar techniques for measurements of ozone and water vapor in the troposphere,” Master of Science Thesis for Penn State University, Department of Electrical Engineering, May, 1999.

Faduilhe, Denis, Hassan Bencherif and Serge Baldy, "Lidar Raman Measurements of Temperature in the southern Tropics : instrumentation Description and First Result Checking on Radiosounding and Model Data," Selected Papers Presented at the 20th International Laser Radar Conference (ILRC), pp. 129-132, Vichy, 10-14 July 2000.

Haris, Paul A.T., "Pure Rotational Raman Lidar for Temperature Measurements in the Lower Troposphere," Doctor of Philosophy Thesis for Penn State University, Department of Electrical Engineering, August, 1995.

Heaps, William S., John Burris and Julie A. French, "Lidar Technique for Remote Measurement of Temperature by Use of Vibrational-Rotational Raman Spectroscopy," Applied Optics-LP, Vol. 36, Issue 36, Page 9402, December, 1997.

Hecht, Eugene, *Optics - Third Edition*. Reading: Addison Wesley Longman, Inc., 1998.

Helvey, R., J. Rosenthal, C.R. Philbrick, T.J. Kane and D.B. Lysak, Jr., "Lidar and radiosonde measurements of coastal atmospheric refraction," Proceedings of the SPIE Atmospheric Propagation and Remote Sensing Conference, vol. 2222, pp. 288-298, 1994.

Henderson, S.W., E.H. Yuen, and E.S. Fry, "Fast resonance-detection technique for single-frequency operation of injection-seeded Nd:YAG lasers," Optics Letters, Vol. 11, No. 11, pp.715-717, November 1986.

Killinger, D.K. and Norman Menyuk, "Laser Remote Sensing of the Atmosphere," Science Vol. 235, pp. 37-45, January 1987.

Kroto, H.W., *Molecular Rotation Spectra*. London: John Wiley & Sons, 1975.

Machuga, David W., "Daytime Performance of the LAMP Rayleigh/Raman Lidar System," Master of Science Thesis for Penn State University, Department of Electrical Engineering, May, 1993.

Marling, Jack, "1.05-1.44 μm Tunability and Performance of the CW Nd^{3+}:YAG Laser," IEEE Journal of Quantum Electronics, Vol. QE-14, No. 1, pp. 56-62, January 1978.

Measures, R.M., *Laser Remote Sensing*. New York: John Wiley & Sons, 1984.

Milonni, P.W. and Joseph H. Eberly, *Lasers*. New York: John Wiley & Sons, 1988.

Mulik, Karoline, "Evolution of Ozone and Particulate Matter During Pollution Events Using Raman Lidar," Master of Science Thesis for Penn State University, Department of Electrical Engineering, May, 2000.

Nedeljkovic, D., Alain Hauchecorne and Marie-Lise Chanin, "Rotational Raman Lidar to Measure the Atmospheric temperature from the Ground to 30 km," IEEE Transactions on Geoscience and Remote Sensing, Vol. 31 No. 1, January 1993.

O'Brien, Michael D., T.D. Stevens, F. Balsiger, and C.R. Philbrick, "Optical extinction from Raman lidar measurements," Proceedings of the SPIE Optical Instruments for Weather Forecasting Conference, vol. 2832, pp. 45-52, 1996.

Petri, Kenneth, Alfred Salik, and John A. Cooney, "Variable-wavelength solar-blind Raman lidar for remote measurement of atmospheric water-vapor concentration and temperature," Applied Optics, Vol. 21 Issue 7, Page 1212, April 1982.

Philbrick, C.R. and Daniel B. Lysak, Jr., "Lidar Measurements of Meteorological Properties and Profiles of RF Refractivity," Proceedings of the 1996 Battlespace Atmospherics Conference, pp. 595-609, 1996.

Rajan S, T.J. Kane, and C.R. Philbrick, "Multiple-wavelength Raman lidar measurements of atmospheric water vapor," Geophysical Research Letters. Vol. 21, no. 23, pp. 2499-2502, 1994.

Vaughan, G., D.P. Wareing, S.J. Pepler, L. Thomas, and V. Mitev, "Atmospheric Temperature Measurements Made by Rotational Raman Scattering," Applied Optics-LP, Vol. 32 Issue 15, Page 2758, May, 1993.

Wave Propagation Panel, "Radio Wave Propagation Modeling, Prediction and Assessment," NATO AGARD Monograph AG-326, Ed. J. H. Richter, 1990.

Zeyn, J., W. Lahmann, and C. Weitkamp, "Remote daytime measurements of tropospheric temperature profiles with a rotational Raman lidar," Optics Letters, Vol. 21 Issue 16, Page 1301, August 1996

Appendix A - OPTICAL HARDWARE SPECIFICATIONS

Table A.1. Narrow-band optical filter specifications.

Item	Description
1	UV Filter, CWL = 386.68 +,-0.02 nm FWHM = 0.10 +,- 0.02 nm, T > 30% E-5 blocking 200-1200 nm, E-10 Blocking @ 354.71 nm 1.0 Inch Diameter, Operating Temp = 34 Deg C
2	Same as Item One Except: CWL = 407.5 +,- 0.02 nm
3	UV Filter, CWL = 352.96 +,- 0.02 nm FWHM = 0.10 +,- 0.02 nm T >15% E-5 Blocking 200-1200 nm, E-10 @ 354.71 nm 1.0 inch diameter, Operating Temp = 34 Deg C
4	UV Filter, CWL = 353.79 +,- 0.02 nm FWHM = 0.10 +,- 0.02 nm, T > 15% E-5 Blocking 200-1200 nm, E-8 Blocking @ 354.71 nm 1.0 inch diameter, Operating Temp = 34 Deg C

Table A.2. Proposed edge filter specifications.

Item	Description
1	Longpass Filter: T>80% @ 528 nm & R>80% @ 408 nm
2	Shortpass Filter: T>70% @ 354 nm & R>80% @ 408 nm
3	50%/50% Beamsplitter Items 1-3 have the following common specifications: AOI = 45º, Designed for operating Temp.=34º but measured @ 23º C Size: 2” DIAMETER Thickness = 6.35mm ±0.5mm
4	Longpass Filter: T>80% @ 407.5 nm & R>80% @ 354.71 nm
5	Bandpass Filter: T>65% @ 353.79 nm & R>80% @ 354.71 nm

	Items 4 & 5 have the following common specifications: AOI = 0º, Designed for operating Temp.=34º but measured @ 23 ºC Size: 1” DIAMETER

Table A.3. Edge filter specification sheet.

LPF • Long Pass Filters

CVI Laser Corporation
800-296-9541

- Long Wave Pass Filters are available individually or as filter sets (see LPFS) for visible, near IR, and IR wavelength ranges
- Custom options are available for cut-on wavelength and size. Contact a CVI applications engineer for more information.

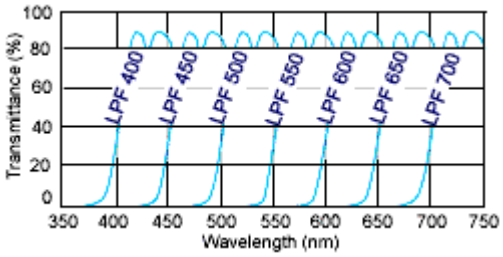

Specifications	
Sizes	0.50" Ø, 1.00" Ø, and 2.00" Ø
Thickness	0.25" nominal
Surface Figure	Commercial polish
Surface Quality	80-50
Clear Aperture	Filter Size / Clear Aperture 0.50" / 0.35" (9.0mm) 1.00" / 0.79" (20.0mm) 2.00" / 1.79" (45.4mm)
Mounting	Black anodized aluminum ring
Cut-on Wavelength	50% of peak transmittance
Cut-on Tolerance	±10mm
Blocking Range	O.D. 3 from x-ray to 85% of cut-on λ
Transmittance Range	from cut-on λto 2500nm

Note: In reference to Figures 5.1 and 5.2, 2” diameter model LPF 450 should be selected for filter position #1. Current cost as of 10 APR 02 is US $210.

Appendix B - MATLAB PROGRAM FOR LIDAR TEMPERATURE DATA REGRESSION TECHNIQUE COMPARISONS

```
%%%%%%%%%%%%%%%%%%%%%%%%%%%%%%%%%%%%%%%%%%%%%%%%%%%%%%%%%%%%%%%%%%%%%%%%
%%%%%
%regressionCompare
%  Function to compare the two lidar temperature data
%  regression methods of:
%   1.) Fitting to lidar ratio & sonde temperature
%   2.) Fitting to theoretical temperature sensitivity
%       curve
%
%   - Utilizes code written by:
%       Alex Achey: for reading LAPS raw data files.
%       Dan Lysak:  for predicting rotational Raman
%                   spectra of N2 and O2
%
%  Created by Corey Slick - 22 MARCH 2002
%%%%%%%%%%%%%%%%%%%%%%%%%%%%%%%%%%%%%%%%%%%%%%%%%%%%%%%%%%%%%%%%%%%%%%%%
%%%%%

function regressionCompare(showTempSensCurveCompare);

%%%%%%%%%%%%%%%%%%%%%%%%%%%%%%%%%%%%%%%%%%%%%%%%%%%%%%%%%%%%%%%%%%%%%%%%
%Effectively loads values given in Appendix D
%%%%%%%%%%%%%%%%%%%%%%%%%%%%%%%%%%%%%%%%%%%%%%%%%%%%%%%%%%%%%%%%%%%%%%%%
%Get filter functions MEASURED with spectrophotometer
%These are the combination of both filters in each channel
%(two 528 filters in 528 channel and two 530 filters in 530 channel)
load('trans_528')
load('trans_530')
load('wavLen_528')
load('wavLen_530')

%Interpolate filter function values using cubic spline method
trans_528 = interp1(wavLen_528,trans_528,[525:0.001:531],'spline');
trans_530 = interp1(wavLen_530,trans_530,[527:0.001:533],'spline');
%Set to zero filter transmissivities measured to be below zero
negIndx = find(trans_528<0);
trans_528(negIndx) = 0;
negIndx = find(trans_530<0);
trans_530(negIndx) = 0;
wavLen_528 = [525:0.001:531];
wavLen_530 = [527:0.001:533];

%Center wavelength shift of metal-oxide filters
%due to temperature increase in detector box above
%that which the filters were originally measured at.
upShift = (34 - 23)*.0025;
wavLen_528 = wavLen_528 + upShift;
wavLen_530 = wavLen_530 + upShift;
%Ideal filter functions centered at approx. 528 nm and 530 nm
```

```
wavLen_528_Ideal = wavLen_528 - 0.3;
wavLen_530_Ideal = wavLen_530 - 0.5;

%Load MEASURED LAPS values
% startDateNum = datenum(2001,07,23,5,12,00);
% endDateNum = datenum(2001,07,23,5,42,00);
startDateNum = datenum(2001,07,10,2,09,00);
endDateNum = datenum(2001,07,10,2,39,00);

%Base path to LAPS raw data files
basePath = 'L:\campaigns\phil_01\laps\rawdata';
integratedRawData = GetIntegratedRawDataSet(basePath, startDateNum, endDateNum);
% 528/530 signal ratio
ratio = [integratedRawData.Channels(4).Signal ./ integratedRawData.Channels(3).Signal]';
%Channels are reversed in LAPS raw data files, take inverse to go from
%INCORRECT - 530/528 to CORRECT - 528/530
ratio = ratio.^-1;

LAPS_alt = load('LAPS_alt'); %LAPS altitudes for these ratios
LAPS_alt = struct2cell(LAPS_alt);
LAPS_alt = LAPS_alt{1};
ratio = ratio(1:length(LAPS_alt));

Sonde_alt = load('Sonde_alt_7_10'); %Sonde altitudes
Sonde_alt = struct2cell(Sonde_alt);
Sonde_alt = Sonde_alt{1};
Sonde_temp = load('Sonde_temp_7_10'); %Sonde temperatures
Sonde_temp = struct2cell(Sonde_temp);
Sonde_temp = Sonde_temp{1};

%Get sonde temperatures measured at altitudes closest to altitudes measured by LAPS
for i = 1:length(LAPS_alt)
   indx = find(abs(LAPS_alt(i)-Sonde_alt) == min(abs(LAPS_alt(i)-Sonde_alt)));
   pos(i) = indx(1);
end
temp = Sonde_temp(pos);

%To remove bad data point in trial data set
LAPS_alt = LAPS_alt(3:end);
ratio = ratio(3:end);
temp = temp(3:end);

%%%%%%%%%%%%%%%%%%%%%%%%%%%%%%%%%%%%%%%%%%%%%%%%%%%%%%%%%%%%%%%%%%%%%%%%%%%%%%%%
%%%%%%%%%%%%%%%%%%%%%%%%%%%%%%%%%%%%%%%%%%%%%%%%%%%%%%%%%%%%%%%%%%%%%%%%%%%%%%%%
%%%
%Main function for Rotational Raman temperature simulation
%Reference: P. Haris dissertation [1995]

%Theoretical temperature calculations for 532 nm transmitted wavelength
wavLenL = 1064.14*10^-9 / 2;

c = 3e10;                       %Speed of light (cm/s)
h = 6.626e-34;                  %Plank's constant (J/s)
k = 1.38e-23;                   %Boltzmann const (J/K)
fLaser = 0.01/wavLenL;          %Laser frequency (1/cm)
```

```
nN2 = 32;                       %Number of wavelengths in N2 & O2 arrays
nO2 = 44;
BN2 = 1.9895;                   %Rotational constants for N2 & O2 (1/cm)
BO2 = 1.43768;
DN2 = 5.48e-6;                  %Centrif distortion const for N2 & O2 (1/cm)
DO2 = 4.85e-6;
IN2 = 1;                        %Nuclear spin
IO2 = 0;
gam2N2 = 0.5e-48;               %Anisotropy of polarizability tensor (squared)
gam2O2 = 1.2e-48;               %(cm^6)


%Do theoretical analysis at same temperature measured by sonde
tC = temp;
tK = tC + 273.16;               %Temps in K
nT = length(tC);                %Number of temps to examine

wavLenN2 = zeros(nN2,1); %Init array sizes
wavLenO2 = zeros(nO2,1);
Q = zeros(nT);

%For N2 calc wavelens of lines j & corresp strength for all temps i
AN2 = zeros(nT, nN2);                   %Init array size - N2 strengths
for j=1 : nN2,
  %Find the wavelength for each line j
  dF = (4*j - 2)*BN2;                   %Frequency shift (1/cm)
  fN2 = fLaser + dF;                    %Freq of lines (1/cm)
  wavLenN2(j) = 0.01 / fN2;             %Wavelength of line (m)
  %Now find the scattering strength at
  %that line for temps i
  b = 3*j*(j-1)/(2*(2*j+1)*(2*j-1));    %Teller-Placzek coefficients
  xSect = 32*pi^4/15*(b * fN2^4 * gam2N2)*0.78; %Relative xSect for line
  gj = 3*(2 - mod(j,2));                %Stat wt N2 (even->6, odd->3)
  for i=1 : nT
    Q = (2*IN2+1)^2*k*tK(i) / (2*h*c*BN2);
    Ej = BN2*h*c*j*(j+1);
    Fj = gj*(2*j + 1) * exp(-Ej/k/tK(i)) / Q;
    AN2(i,j) = Fj * xSect;              %Rel strength of line j, temp i
  end;
end;

%Repeat for O2
AO2 = zeros(nT, nO2);                   %Init array size - O2 strengths
for j=1 : nO2,
  %Find the wavelength for each line j
  dF = (4*j - 2)*BO2;                   %Frequency shift (1/cm)
  freq = fLaser + dF;                   %Freq of lines (1/cm)
  wavLenO2(j) = 0.01 / freq;            %Wavelength of line (m)
  %Now find the scattering strength
  %at that line for temps i
  b = 3*j*(j-1)/(2*(2*j+1)*(2*j-1));    %Teller-Placzek coefficients
  xSect = 32*pi^4/15*(b * freq^4 * gam2O2)*0.21;%Relative xSect for line
  gj = mod(j,2);                        %Stat wt O2 (even->0, odd->1)
  for i=1 : nT
    Q = (2*IO2+1)^2*k*tK(i) / (2*h*c*BO2);
    Ej = BO2*h*c*j*(j+1);
```

```
    Fj = gj*(2*j + 1) * exp(-Ej/k/tK(i)) / Q;
    AO2(i,j) = Fj * xSect;                %Rel strength of line j, temp i
  end;
end;

%Four bounds for the filters - from the range of spectrophotometer measurements
w1 = min(wavLen_528);
w2 = max(wavLen_528);
w3 = min(wavLen_530);
w4 = max(wavLen_530);
w1_Ideal = min(wavLen_528_Ideal);
w2_Ideal = max(wavLen_528_Ideal);
w3_Ideal = min(wavLen_530_Ideal);
w4_Ideal = max(wavLen_530_Ideal);

%Convert to nanometers to make use of necessary number of decimal places,
%avoiding successive identical shifted wavelengths
wavLenO2_All = wavLenO2 * 10^9;
wavLenN2_All = wavLenN2 * 10^9;

%Avoid throwing initial data off on each iteration
savedN2Strength = AN2;
savedO2Strength = AO2;


for inputTempIndex = 1:length(tC);
   inputTempIndex
   %Get rid of zero intensity N2 & O2 lines (they throw a wrench in the works)
   indexO2 = find(savedO2Strength(inputTempIndex,:)~=0);
   indexN2 = find(savedN2Strength(inputTempIndex,:)~=0);
   strengthO2 = savedO2Strength(inputTempIndex,indexO2);
   strengthN2 = savedN2Strength(inputTempIndex,indexN2);
   wavLenO2 = wavLenO2_All(indexO2);
   wavLenN2 = wavLenN2_All(indexN2);

   ampN2_1 = 0;
   ampN2_2 = 0;
   ampO2_1 = 0;
   ampO2_2 = 0;
   newStrengthN2 = strengthN2;
   for j = 1:length(wavLenN2)

      %Determine whether N2 Raman line wavelength falls within filter function #1
      if (wavLenN2(j)>=w1 & wavLenN2(j)<=w2)
         %Find theoretical line position most closely matching that measured
         %with spectrophotometer
         wavInd = find( abs(wavLenN2(j)-wavLen_528) == min(abs(wavLenN2(j)-wavLen_528)) );
         %Multiply value of filter function by theoretical line intensity
         newStrengthN2(j) = strengthN2(j) * trans_528(wavInd);
         ampN2_1 = ampN2_1 + newStrengthN2(j);
      end

      %Determine whether N2 Raman line wavelength falls within filter function #2
      if (wavLenN2(j)>=w3 & wavLenN2(j)<=w4)
         %Find theoretical line position most closely matching that measured
         %with spectrophotometer
```

```
        wavInd = find( abs(wavLenN2(j)-wavLen_530) == min(abs(wavLenN2(j)-wavLen_530)) );
        %Multiply value of filter function by theoretical line intensity
        newStrengthN2(j) = strengthN2(j) * trans_530(wavInd);
        ampN2_2 = ampN2_2 + newStrengthN2(j);
    end


    %Determine whether Ideal N2 Raman line wavelength falls within filter function #1
    if (wavLenN2(j)>=w1_Ideal & wavLenN2(j)<=w2_Ideal)
        %Find theoretical line position most closely matching that measured
        %with spectrophotometer
        wavInd = find( abs(wavLenN2(j)-wavLen_528_Ideal) == min(abs(wavLenN2(j)-
wavLen_528_Ideal)) );
        %Multiply value of filter function by theoretical line intensity
        newStrengthN2_Ideal(j) = strengthN2(j) * trans_528(wavInd);
        ampN2_1_Ideal = ampN2_1 + newStrengthN2_Ideal(j);
    end

    %Determine whether Ideal N2 Raman line wavelength falls within filter function #2
    if (wavLenN2(j)>=w3_Ideal & wavLenN2(j)<=w4_Ideal)
        %Find theoretical line position most closely matching that measured
        %with spectrophotometer
        wavInd = find( abs(wavLenN2(j)-wavLen_530_Ideal) == min(abs(wavLenN2(j)-
wavLen_530_Ideal)) );
        %Multiply value of filter function by theoretical line intensity
        newStrengthN2_Ideal(j) = strengthN2(j) * trans_530(wavInd);
        ampN2_2_Ideal = ampN2_2 + newStrengthN2_Ideal(j);
    end


end

newStrengthO2 = strengthO2;
for j = 1:length(wavLenO2)

    %Determine whether O2 Raman line wavelength falls within filter function #1
    if (wavLenO2(j)>=w1 & wavLenO2(j)<=w2)
        %Find theoretical line position most closely matching that measured
        %with spectrophotometer
        wavInd = find( abs(wavLenO2(j)-wavLen_528) == min(abs(wavLenO2(j)-wavLen_528)) );
        %Multiply value of filter function by theoretical line intensity
        newStrengthO2(j) = strengthO2(j) * trans_528(wavInd);
        ampO2_1 = ampO2_1 + newStrengthO2(j);
    end

    %Determine wheter O2 Raman line wavelength falls within filter function #2
    if (wavLenO2(j)>=w3 & wavLenO2(j)<=w4)
        %Find theoretical line position most closely matching that measured
        %with spectrophotometer
        wavInd = find( abs(wavLenO2(j)-wavLen_530) == min(abs(wavLenO2(j)-wavLen_530)) );
        %Multiply value of filter function by theoretical line intensity
        newStrengthO2(j) = strengthO2(j) * trans_530(wavInd);
        ampO2_2 = ampO2_2 + newStrengthO2(j);
    end
```

```
      %Determine whether Ideal O2 Raman line wavelength falls within filter function #1
      if (wavLenO2(j)>=w1_Ideal & wavLenO2(j)<=w2_Ideal)
         %Find theoretical line position most closely matching that measured
         %with spectrophotometer
         wavInd = find( abs(wavLenO2(j)-wavLen_528) == min(abs(wavLenO2(j)-wavLen_528)) );
         %Multiply value of filter function by theoretical line intensity
         newStrengthO2_Ideal(j) = strengthO2(j) * trans_528(wavInd);
         ampO2_1_Ideal = ampO2_1 + newStrengthO2_Ideal(j);
      end

      %Determine wheter Ideal O2 Raman line wavelength falls within filter function #2
      if (wavLenO2(j)>=w3_Ideal & wavLenO2(j)<=w4_Ideal)
         %Find theoretical line position most closely matching that measured
         %with spectrophotometer
         wavInd = find( abs(wavLenO2(j)-wavLen_530) == min(abs(wavLenO2(j)-wavLen_530)) );
         %Multiply value of filter function by theoretical line intensity
         newStrengthO2_Ideal(j) = strengthO2(j) * trans_530(wavInd);
         ampO2_2_Ideal = ampO2_2 + newStrengthO2_Ideal(j);
      end


   end

   %Use correction for 70/30 temperature channel beamsplitter (70% to 528 channel)
   ratio_current(inputTempIndex) = (ampN2_1 + ampO2_1)/ (ampN2_2 + ampO2_2) * (3/7);
   ratio_orig(inputTempIndex) = (ampN2_1_Ideal + ampO2_1_Ideal) / (ampN2_2_Ideal +
ampO2_2_Ideal) * (3/7);

end

if showTempSensCurveCompare

   %Show that theoretical ratio curve does not change because of the
   %observed shift in 528 and 530 channel filter center wavelengths
   figure
   subplot(3,1,1)
   plot(wavLen_528,trans_528*100,'b',wavLen_530,trans_530*100,'g')
   grid on
   h = title('Measured Filter Functions');
   set(h,'FontWeight','Bold')
   ylabel('% Transmission')
   xlabel('Wavelength [nm]')
   legend('528 nm Channel Filters','530 nm Channel Filters',2)
   subplot(3,1,2)
   plot(wavLen_528_Ideal,trans_528*100,'b',wavLen_530_Ideal,trans_530*100,'g')
   grid on
   legend('Original 528 nm Channel Filters','Original 530 nm Channel Filters',2)
   ylabel('% Transmission')
   xlabel('Wavelength [nm]')
   subplot(3,1,3)
   plot(ratio_current,tC+273.16,'rx-',ratio_orig,tC+273.16,'bo-')
   axis tight
   h = title('Temperature vs Lidar Ratio');
   set(h,'FontWeight','Bold')
   xlabel('528/530 Ratio')
   ylabel('Temperature [K]')
```

```
    legend('Shifted Filter Centers','Original Filter Centers',2)

end
%%%%%%%%%%%%%%%%%%%%%%%%%%%%%%%%%%%%%%%%%%%%%%%%%%%
%%%%%%%%%%%%%%%%%%%%%%%%%%%%%%%%%%%%%%%%%%%%%%%%%%%
%%%%%%%%%%%%%%%%%%%%%%%%%%%

%Plotting
Name = ['Integration of LAPS data from: ' datestr(startDateNum) ' - ' datestr(endDateNum)];
figure
set(gcf,'Name',Name,'NumberTitle','off')
subplot(2,2,1)
plot(ratio,LAPS_alt,'b-x')
axis tight
legend('Measured LAPS Ratios',1)
ylabel('Altitude [m]')
xlabel('528/530 Ratio')

subplot(2,2,2)
plot(Sonde_temp+273.15,Sonde_alt,'b-')
axis tight
legend('Sonde Temps',1)
ylabel('Altitude [m]')
xlabel('Temp [K]')

subplot(2,2,3)
plot(temp+273.15,ratio,'b-x')
xlabel('Temperature [K]')
ylabel('528/530 Ratio')
axis tight
ht=get(gca,'title');
set(ht,'FontSize',12,'FontWeight','Bold');
legend('Measured Temp vs Ratio',2)

subplot(2,2,4)
plot(tC+273.15,ratio_current,'b-')
axis tight
legend('Theoretical Temp vs Ratio',2)
ylabel('528/530 Ratio')
xlabel('Temperature [K]')

%%%%%%%%%%%%%%%%%%%%%%%%%%%%%%%%%
%Sonde altitude/temp data fitting
%%%%%%%%%%%%%%%%%%%%%%%%%%%%%%%%%%%%%%%%%%%%%%%%%%%
%%%%%%%%%%%%%%%%%%%%%%%%
%Do regression fit
X = [ones(size(ratio))  ratio  ratio.^2];
a2 = X\temp;
oldTempFitCurve = [ones(size(ratio))  ratio  ratio.^2]*a2 + 273.16;
%%%%%%%%%%%%%%%%%%%%%%%%%%%%%%%%%%%%%%%%%%%%%%%%%%%
%%%%%%%%%%%%%%%%%%%%%%%%

%Plotting
figure
set(gcf,'Name',Name,'NumberTitle','off')
subplot(1,2,1)
```

```
hold on
plot(ratio,temp+273.15,'b-x',ratio,oldTempFitCurve,'g-')
grid on
xlabel('528/530 Channel Count Ratio')
ylabel('Temperature [K]')
title('Curve Fitting')
axis tight;
legend('LIDAR Ratio & Sonde Temp.','Second-Order Fit',2)
ht=get(gca,'title');
set(ht,'FontSize',12,'FontWeight','Bold');

subplot(1,2,2)
hold on
plot(Sonde_temp+273.15,Sonde_alt,'b-',oldTempFitCurve,LAPS_alt,'g-')
legend('Sonde','Calibrated LIDAR')
grid on
xlabel('Temperature [K]')
ylabel('Altitude [m]')
line1 = ['a = ' num2str(a2(3))];
line2 = ['b = ' num2str(a2(2))];
line3 = ['c = ' num2str(a2(1))];
title({'Typical Calibrated Lidar';[line1 '  ' line2 '  ' line3]})
axis tight;
ht=get(gca,'title');
set(ht,'FontSize',12,'FontWeight','Bold');


%%%%%%%%%%%%%%%%%%%%%%%%%%%%%%%%%%%%%%%%%%%%%%%%%%%%%%%%%%%%
%Theoretical temp sensitivity curve fitting
%%%%%%%%%%%%%%%%%%%%%%%%%%%%%%%%%%%%%%%%%%%%%%%%%%%%%%%%%%%%
X = [ones(size(ratio)) ratio];
%Fit to theoretical ratios obtained using current filter center wavlengths
a1 = X \ ratio_current'
newTempFitCurve = [ones(size(ratio)) ratio]*a1;
newTempFitCurve1 = newTempFitCurve;

interpTemps = [-70:.01:70]+273.16;
%Get rid of repeated temperature values (for interpolation)
[tC_new,I,J] = unique(tC);
tC_new = tC_new(end:-1:1);
ratio_current_new = ratio_current(I(end:-1:1));
%Interpolate values of theoretical temp. sensitivity curve
newRatios = interp1(tC_new+273.15,ratio_current_new,interpTemps,'spline');
for i = 1:length(newTempFitCurve1)
   %Get index into new temperatures where new ratio is closest to theoretical value
   indexVal = find( abs( (newTempFitCurve1(i) - newRatios)) == min( abs( (newTempFitCurve1(i) -
newRatios))  ) );
   newTemps(i) = interpTemps(indexVal);
end
newTemps1 = newTemps;

X = [ones(size(ratio)) ratio ratio.^2];
%Fit to theoretical ratios obtained using current filter center wavlengths
a1 = X \ ratio_current'
newTempFitCurve = [ones(size(ratio)) ratio ratio.^2]*a1;
newTempFitCurve2 = newTempFitCurve;
```

```
interpTemps = [-70:.01:70]+273.16;
%Get rid of repeated temperature values (for interpolation)
[tC_new,I,J] = unique(tC);
tC_new = tC_new(end:-1:1);
ratio_current_new = ratio_current(I(end:-1:1));
%Interpolate values of theoretical temp. sensitivity curve
newRatios = interp1(tC_new+273.15,ratio_current_new,interpTemps,'spline');
for i = 1:length(newTempFitCurve2)
   %Get index into new temperatures where new ratio is closest to theoretical value
   indexVal = find( abs( (newTempFitCurve2(i) - newRatios)) == min( abs( (newTempFitCurve2(i) -
newRatios))  ) );
   newTemps(i) = interpTemps(indexVal);
end
newTemps2 = newTemps;

X = [ones(size(ratio)) ratio ratio.^2 ratio.^3];
%Fit to theoretical ratios obtained using current filter center wavlengths
a1 = X \ ratio_current'
newTempFitCurve = [ones(size(ratio)) ratio ratio.^2 ratio.^3]*a1;
newTempFitCurve3 = newTempFitCurve;

interpTemps = [-70:.01:70]+273.16;
%Get rid of repeated temperature values (for interpolation)
[tC_new,I,J] = unique(tC);
tC_new = tC_new(end:-1:1);
ratio_current_new = ratio_current(I(end:-1:1));
%Interpolate values of theoretical temp. sensitivity curve
newRatios = interp1(tC_new+273.15,ratio_current_new,interpTemps,'spline');
for i = 1:length(newTempFitCurve3)
   %Get index into new temperatures where new ratio is closest to theoretical value
   indexVal = find( abs( (newTempFitCurve3(i) - newRatios)) == min( abs( (newTempFitCurve3(i) -
newRatios))  ) );
   newTemps(i) = interpTemps(indexVal);
end
newTemps3 = newTemps;

X = [ones(size(ratio)) ratio ratio.*exp(-ratio)];
%Fit to theoretical ratios obtained using current filter center wavlengths
a1 = X \ ratio_current'
newTempFitCurve = [ones(size(ratio)) ratio ratio.*exp(-ratio)]*a1;
newTempFitCurve4 = newTempFitCurve;

interpTemps = [-70:.01:70]+273.16;
%Get rid of repeated temperature values (for interpolation)
[tC_new,I,J] = unique(tC);
tC_new = tC_new(end:-1:1);
ratio_current_new = ratio_current(I(end:-1:1));
%Interpolate values of theoretical temp. sensitivity curve
newRatios = interp1(tC_new+273.15,ratio_current_new,interpTemps,'spline');
for i = 1:length(newTempFitCurve4)
   %Get index into new temperatures where new ratio is closest to theoretical value
   indexVal = find( abs( (newTempFitCurve4(i) - newRatios)) == min( abs( (newTempFitCurve4(i) -
newRatios))  ) );
   newTemps(i) = interpTemps(indexVal);
end
```

```
newTemps4 = newTemps;

%Plotting
figure
set(gcf,'Name',Name,'NumberTitle','off')
subplot(1,2,1)
plot(tC+273.15,ratio_current,'b-*',temp+273.15,newTempFitCurve1,'k-
',temp+273.15,newTempFitCurve2,'g',temp+273.15,newTempFitCurve3,'r',temp+273.15,newTempFitCurv
e4,'c')
title('Curve Fitting','FontSize',12,'FontWeight','Bold');
axis tight
grid on
axis tight
title('Curve Fitting','FontSize',12,'FontWeight','Bold');
legend('Theoretical Temp. Sensitivity','First-order fit','Second-order fit','Third-order fit','Exponential Fit',2)
xlabel('Temperature [K]')
ylabel('528/530 Ratio')

subplot(1,2,2)
hold on
plot(Sonde_temp+273.15,Sonde_alt,'b-',newTemps1,LAPS_alt,'k-
',newTemps2,LAPS_alt,'g',newTemps3,LAPS_alt,'r',newTemps4,LAPS_alt,'c')
legend('Sonde Temps','First-order fit','Second-order fit','Third-order fit','Exponential Fit',1)
grid on
axis tight
title({'Lidar Calibrated with Theoretical';'Temperature Sensitivity
Curve'},'FontSize',12,'FontWeight','Bold')
xlabel('Temperature [K]')
ylabel('Altitude [m]')

figure
subplot(1,2,1)
hold on
plot(Sonde_temp+273.15,Sonde_alt,'b-',oldTempFitCurve,LAPS_alt,'g-')
legend('Sonde','Calibrated LIDAR')
grid on
xlabel('Temperature [K]')
ylabel('Altitude [m]')
line1 = ['a = ' num2str(a2(3))];
line2 = ['b = ' num2str(a2(2))];
line3 = ['c = ' num2str(a2(1))];
title({'Typical Calibrated Lidar';[line1 '  ' line2 '  ' line3]})
axis tight;
ht=get(gca,'title');
set(ht,'FontSize',12,'FontWeight','Bold');

subplot(1,2,2)
hold on
plot(Sonde_temp+273.15,Sonde_alt,'b-',newTemps2,LAPS_alt,'g')
legend('Sonde Temps','Second-order fit',1)
grid on
axis tight
title({'Lidar Calibrated with Theoretical';'Temperature Sensitivity
Curve'},'FontSize',12,'FontWeight','Bold')
xlabel('Temperature [K]')
ylabel('Altitude [m]')
```

Appendix C - MEASURED TEMPERATURE FILTER TRANSMISSION VALUES

Table C.1. 528 nm channel filter trnamission values.

Wavelength [nm]	%T	Wavelength [nm]	%T	Wavelength [nm]	%T
531	0.4	530.56	0.3	530.19	-0.2
530.99	1.9	530.55	0.2	530.18	-0.1
530.98	1.7	530.54	-0.2	530.17	-0.3
530.97	0.6	530.53	-0.4	530.16	-0.3
530.96	-0.5	530.52	-0.5	530.15	-0.3
530.95	-0.2	530.51	-0.5	530.14	-0.2
530.94	-0.1	530.5	-0.3	530.13	-0.1
530.93	0	530.49	-0.2	530.12	-0.1
530.92	0.1	530.48	0	530.11	-0.3
530.91	0.1	530.47	0.1	530.1	-0.1
530.9	0	530.46	0.2	530.09	-0.2
530.89	-0.2	530.45	0	530.08	0
530.88	-0.3	530.44	0	530.07	-0.1
530.87	-0.3	530.43	-0.3	530.06	-0.3
530.86	-0.3	530.42	-0.4	530.05	-0.4
530.85	-0.2	530.41	-0.4	530.04	-0.3
530.84	-0.1	530.4	-0.2	530.03	-0.3
530.83	-0.1	530.39	0	530.02	0
530.82	-0.4	530.38	-0.1	530.01	0.1
530.81	-0.4	530.37	-0.2	530	0.1
530.8	-0.3	530.36	-0.1	529.99	0
530.79	0	530.35	-0.1	529.98	-0.1
530.78	0.1	530.34	0.2	529.97	-0.1
530.77	0.1	530.33	0.3	529.96	0
530.76	-0.1	530.32	0.1	529.95	0.1
530.75	-0.1	530.31	-0.1	529.94	0
530.74	-0.1	530.3	-0.5	529.93	0.2
530.73	0	530.29	-0.4	529.92	0.1
530.72	-0.1	530.28	-0.2	529.91	0.2
530.71	0	530.27	-0.1	529.9	0.1
530.7	-0.3	530.56	0.3	529.89	0.1
530.69	-0.2	530.55	0.2	529.88	0.2
530.68	-0.1	530.54	-0.2	529.87	0.2
530.67	0	530.53	-0.4	529.86	0.1
530.66	0	530.52	-0.5	529.85	0.1
530.65	-0.1	530.51	-0.5	529.84	-0.1
530.64	-0.4	530.5	-0.3	529.83	-0.2
530.63	-0.4	530.26	-0.2	529.82	-0.2
530.62	-0.2	530.25	-0.3	529.81	-0.2
530.61	0	530.24	-0.6	529.8	0.1
530.6	-0.1	530.23	-0.4	529.79	0.3
530.59	0	530.22	-0.3	529.78	0.2
530.58	0.1	530.21	-0.1	529.77	0.1
530.57	0.1	530.2	-0.2	529.76	0

Wavelength [nm]	%T	Wavelength [nm]	%T	Wavelength [nm]	%T
529.75	-0.1	529.73	0.2	529.22	0.1
529.74	0	529.72	-0.1	529.21	0.1
529.73	0.2	529.71	-0.1	529.2	0.1
529.72	-0.1	529.7	-0.2	529.19	0
529.71	-0.1	529.69	-0.2	529.18	0
529.7	-0.2	529.68	-0.1	529.17	0.2
529.69	-0.2	529.67	0.1	529.16	0.6
529.68	-0.1	529.66	0.1	529.15	0.5
529.67	0.1	529.65	0.1	529.14	0.5
529.66	0.1	529.64	0.1	529.13	0.3
529.65	0.1	529.63	0.3	529.12	0
529.64	0.1	529.62	0.3	529.11	-0.2
529.63	0.3	529.61	0.3	529.1	-0.1
529.62	0.3	529.6	0	529.09	-0.2
529.61	0.3	529.59	-0.2	529.08	0.2
529.6	0	529.58	-0.3	529.07	0.5
529.59	-0.2	529.57	-0.2	529.06	0.7
529.58	-0.3	529.56	-0.2	529.05	0.6
529.57	-0.2	529.55	-0.1	529.04	0.4
529.56	-0.2	529.54	-0.4	529.03	0.1
529.55	-0.1	529.53	-0.4	529.02	0
529.54	-0.4	529.52	-0.4	529.01	0.1
529.53	-0.4	529.51	-0.3	529	0.3
529.52	-0.4	529.5	-0.1	528.99	0.5
529.51	-0.3	529.49	0	528.98	0.3
529.5	-0.1	529.48	0	528.97	0
529.49	0	529.47	0.1	528.96	-0.1
529.48	0	529.46	0	528.95	-0.3
529.47	0.1	529.45	-0.1	528.94	-0.2
529.46	0	529.44	-0.2	528.93	0
529.45	-0.1	529.43	-0.1	528.92	0
529.44	-0.2	529.42	0	528.91	0
529.43	-0.1	529.41	0.1	528.9	0.1
529.42	0	529.4	0.1	528.89	0.1
529.41	0.1	529.39	-0.1	528.88	0.3
529.4	0.1	529.38	-0.2	528.87	0.5
529.39	-0.1	529.37	-0.3	528.86	0.5
529.38	-0.2	529.36	-0.2	528.85	0.6
529.37	-0.3	529.35	0	528.84	0.3
529.36	-0.2	529.34	0.1	528.83	0.2
529.35	0	529.33	0	528.82	0.3
529.34	0.1	529.32	-0.1	528.81	0.5
529.33	0	529.31	-0.2	528.8	0.8
529.32	-0.1	529.3	-0.1	528.79	1
529.31	-0.2	529.29	-0.1	528.78	1
529.3	-0.1	529.28	0.1	528.77	1.1
529.29	-0.1	529.27	-0.1	528.76	1.4
529.28	0.1	529.26	0	528.75	1.3
529.27	-0.1	529.25	0	528.74	1.2
529.75	-0.1	529.24	-0.1	528.73	1
529.74	0	529.23	0	528.72	1

Wavelength [nm]	%T	Wavelength [nm]	%T	Wavelength [nm]	%T
528.71	1.1	528.2	3.5	527.69	0.8
528.7	1.5	528.19	3.5	527.68	0.6
528.69	1.6	528.18	3.4	527.67	0.5
528.68	1.5	528.17	3.2	527.66	0.6
528.67	1.6	528.16	3.1	527.65	0.8
528.66	1.8	528.15	3.2	527.64	0.7
528.65	1.9	528.14	3.1	527.63	0.6
528.64	1.9	528.13	3	527.62	0.3
528.63	2	528.12	3	527.61	0
528.62	2	528.11	2.9	527.6	-0.1
528.61	2	528.1	2.7	527.59	0
528.6	2.1	528.09	2.7	527.58	0.1
528.59	2.4	528.08	2.8	527.57	0.3
528.58	2.4	528.07	3	527.56	0.2
528.57	2.6	528.06	2.8	527.55	0.2
528.56	2.8	528.05	2.8	527.54	0.3
528.55	2.6	528.04	2.5	527.53	0.2
528.54	2.8	528.03	2.5	527.52	0.3
528.53	3.1	528.02	2.6	527.51	0.1
528.52	3	528.01	2.7	527.5	-0.1
528.51	2.9	528	2.6	527.49	-0.2
528.5	3.2	527.99	2.8	527.48	-0.2
528.49	3.3	527.98	2.8	527.47	-0.1
528.48	3.6	527.97	2.9	527.46	0.1
528.47	3.6	527.96	2.8	527.45	0.2
528.46	3.5	527.95	2.7	527.44	0.3
528.45	3.6	527.94	2.6	527.43	0
528.44	3.6	527.93	2.5	527.42	-0.1
528.43	3.7	527.92	2.5	527.41	-0.3
528.42	3.8	527.91	2.7	527.4	-0.3
528.41	3.6	527.9	2.6	527.39	-0.1
528.4	3.6	527.89	2.6	527.38	0
528.39	3.7	527.88	2.5	527.37	0.1
528.38	3.6	527.87	2.4	527.36	0.1
528.37	3.7	527.86	2.2	527.35	0.1
528.36	3.7	527.85	2.4	527.34	0
528.35	3.6	527.84	2.1	527.33	0.2
528.34	3.7	527.83	2.2	527.32	0.1
528.33	3.6	527.82	2.1	527.31	0.3
528.32	3.6	527.81	2.1	527.3	0.2
528.31	3.6	527.8	2.1	527.29	0.1
528.3	3.6	527.79	2.2	527.28	0
528.29	3.6	527.78	1.9	527.27	0.2
528.28	3.7	527.77	1.7	527.26	0.2
528.27	3.5	527.76	1.2	527.25	0.1
528.26	3.3	527.75	1	527.24	0.1
528.25	3.5	527.74	1	527.23	-0.2
528.24	3.6	527.73	1	527.22	-0.2
528.23	3.6	527.72	1.1	527.21	-0.2
528.22	3.7	527.71	1.1	527.2	-0.1
528.21	3.7	527.7	0.8	527.19	-0.3

Wavelength [nm]	%T	Wavelength [nm]	%T	Wavelength [nm]	%T
527.18	0	526.67	0.2	526.16	-0.4
527.17	-0.1	526.66	0	526.15	-0.2
527.16	0.1	526.65	0.1	526.14	0
527.15	0	526.64	-0.1	526.13	0.2
527.14	-0.1	526.63	0.1	526.12	0.1
527.13	-0.3	526.62	-0.1	526.11	-0.2
527.12	-0.4	526.61	-0.3	526.1	-0.4
527.11	-0.5	526.6	-0.4	526.09	-0.5
527.1	-0.4	526.59	-0.1	526.08	-0.7
527.09	-0.2	526.58	0	526.07	-0.5
527.08	-0.1	526.57	0.3	526.06	-0.2
527.07	-0.1	526.56	0	526.05	0.1
527.06	-0.3	526.55	-0.4	526.04	0.2
527.05	-0.1	526.54	-0.3	526.03	0.1
527.04	0.1	526.53	-0.1	526.02	0
527.03	0.1	526.52	0	526.01	0
527.02	0	526.51	0	526	-0.1
527.01	0	526.5	-0.1	525.99	0
527	-0.3	526.49	-0.4	525.98	-0.2
526.99	-0.2	526.48	-0.1	525.97	-0.3
526.98	-0.1	526.47	0	525.96	-0.2
526.97	-0.3	526.46	0.1	525.95	-0.1
526.96	-0.3	526.45	0	525.94	-0.1
526.95	-0.1	526.44	-0.3	525.93	0
526.94	-0.2	526.43	-0.2	525.92	-0.1
526.93	0	526.42	-0.2	525.91	0
526.92	0	526.41	-0.4	525.9	0
526.91	0.1	526.4	-0.2	525.89	-0.1
526.9	-0.1	526.39	-0.2	525.88	-0.2
526.89	0	526.38	-0.3	525.87	-0.2
526.88	-0.2	526.37	-0.1	525.86	0
526.87	-0.1	526.36	-0.1	525.85	0.1
526.86	-0.1	526.35	-0.1	525.84	0.1
526.85	0	526.34	0	525.83	0
526.84	-0.2	526.33	0	525.82	-0.3
526.83	-0.1	526.32	0	525.81	-0.3
526.82	-0.1	526.31	-0.1	525.8	-0.1
526.81	-0.1	526.3	-0.2	525.79	0
526.8	-0.3	526.29	-0.3	525.78	-0.1
526.79	-0.3	526.28	-0.3	525.77	-0.2
526.78	-0.2	526.27	-0.3	525.76	-0.2
526.77	-0.1	526.26	-0.1	525.75	-0.1
526.76	0	526.25	-0.2	525.74	-0.1
526.75	0.1	526.24	-0.1	525.73	0
526.74	0.2	526.23	-0.2	525.72	0
526.73	0.2	526.22	0	525.71	0
526.72	0.3	526.21	0.1	525.7	0
526.71	0.2	526.2	0.3	525.69	-0.2
526.7	0	526.19	0.2	525.68	-0.4
526.69	0.1	526.18	0	525.67	-0.3
526.68	0.2	526.17	-0.4	525.66	-0.3

Wavelength [nm]	%T	Wavelength [nm]	%T
525.65	-0.1	525.14	-0.6
525.64	-0.2	525.13	-0.6
525.63	-0.2	525.12	-0.3
525.62	-0.2	525.11	-0.1
525.61	-0.1	525.1	-0.1
525.6	-0.2	525.09	0.1
525.59	0	525.08	0.2
525.58	-0.2	525.07	0.2
525.57	-0.5	525.06	0.1
525.56	-0.5	525.05	0.2
525.55	-0.4	525.04	0
525.54	-0.4	525.03	0
525.53	-0.4	525.02	0.1
525.52	-0.5	525.01	0.1
525.51	-0.5	525	0.1
525.5	-0.2		
525.49	0.1		
525.48	0.1		
525.47	0		
525.46	-0.1		
525.45	0.1		
525.44	0.1		
525.43	0		
525.42	-0.2		
525.41	-0.4		
525.4	-0.3		
525.39	-0.1		
525.38	0		
525.37	0.1		
525.36	0		
525.35	0		
525.34	0		
525.33	-0.2		
525.32	-0.2		
525.31	-0.3		
525.3	-0.2		
525.29	0		
525.28	0.1		
525.27	0.1		
525.26	0.3		
525.25	0.1		
525.24	-0.2		
525.23	-0.4		
525.22	-0.8		
525.21	-0.8		
525.2	-0.3		
525.19	0		
525.18	0.4		
525.17	0.1		
525.16	-0.4		
525.15	-0.6		

Table C.2. 530 nm channel filter trnamission values.

Wavelength [nm]	%T	Wavelength [nm]	%T	Wavelength [nm]	%T
533	1.2	532.5	-0.1	532	-0.3
532.99	0.5	532.49	0.1	531.99	0
532.98	0.1	532.48	0.3	531.98	-0.1
532.97	-0.2	532.47	0.3	531.97	-0.1
532.96	-0.5	532.46	0.1	531.96	0
532.95	-0.4	532.45	-0.2	531.95	0.1
532.94	-0.5	532.44	-0.5	531.94	0
532.93	-0.3	532.43	-0.6	531.93	-0.2
532.92	-0.1	532.42	-0.4	531.92	-0.3
532.91	0.2	532.41	-0.5	531.91	-0.3
532.9	0	532.4	-0.5	531.9	-0.2
532.89	0	532.39	-0.4	531.89	-0.1
532.88	-0.2	532.38	-0.3	531.88	0
532.87	-0.2	532.37	-0.5	531.87	-0.1
532.86	-0.4	532.36	-0.3	531.86	-0.1
532.85	-0.3	532.35	-0.5	531.85	-0.1
532.84	-0.4	532.34	-0.3	531.84	-0.1
532.83	-0.3	532.33	-0.2	531.83	0
532.82	-0.6	532.32	-0.2	531.82	-0.1
532.81	-0.6	532.31	-0.2	531.81	-0.3
532.8	-0.7	532.3	-0.1	531.8	-0.3
532.79	-0.2	532.29	-0.1	531.79	-0.2
532.78	0.3	532.28	0.1	531.78	-0.2
532.77	0.3	532.27	0.2	531.77	-0.1
532.76	0.4	532.26	0.1	531.76	0
532.75	0.2	532.25	0.1	531.75	0.1
532.74	0.1	532.24	-0.2	531.74	0.4
532.73	0.1	532.23	-0.2	531.73	0.6
532.72	0.1	532.22	-0.2	531.72	0.7
532.71	-0.1	532.21	-0.2	531.71	0.2
532.7	0.1	532.2	-0.1	531.7	-0.2
532.69	-0.1	532.19	0.1	531.69	-0.3
532.68	-0.1	532.18	0.2	531.68	-0.2
532.67	-0.1	532.17	0.2	531.67	0
532.66	-0.2	532.16	0.1	531.66	0.4
532.65	-0.2	532.15	-0.2	531.65	0.3
532.64	-0.3	532.14	-0.3	531.64	0.2
532.63	-0.1	532.13	-0.3	531.63	-0.2
532.62	-0.2	532.12	0.1	531.62	-0.2
532.61	0.1	532.11	0.1	531.61	-0.3
532.6	0.1	532.1	0.3	531.6	-0.1
532.59	0.4	532.09	0.4	531.59	0.1
532.58	0.4	532.08	0.4	531.58	0.1
532.57	0.7	532.07	0.2	531.57	0
532.56	0.6	532.06	0.2	531.56	0.1
532.55	0.6	532.05	0.1	531.55	0
532.54	0.3	532.04	0	531.54	0.1
532.53	0.1	532.03	-0.1	531.53	0.1
532.52	0	532.02	-0.2	531.52	0.1
532.51	0	532.01	-0.3	531.51	0.2

Wavelength [nm]	%T	Wavelength [nm]	%T	Wavelength [nm]	%T
531.5	0.1	530.99	0.8	530.48	2.5
531.49	0	530.98	1.1	530.47	2.3
531.48	0.1	530.97	1.3	530.46	2.2
531.47	0.2	530.96	1.5	530.45	2.2
531.46	0.2	530.95	1.7	530.44	2.4
531.45	0.2	530.94	1.7	530.43	2.5
531.44	0.3	530.93	1.7	530.42	2.4
531.43	0.3	530.92	1.9	530.41	2.5
531.42	0.1	530.91	1.8	530.4	2.5
531.41	0.1	530.9	1.7	530.39	2.5
531.4	0.1	530.89	1.9	530.38	3
531.39	0.1	530.88	2.1	530.37	2.9
531.38	0.3	530.87	2.1	530.36	2.9
531.37	0.3	530.86	2.3	530.35	2.9
531.36	0.1	530.85	2.3	530.34	2.8
531.35	0.3	530.84	1.9	530.33	3
531.34	0.4	530.83	1.7	530.32	3.4
531.33	0.3	530.82	2.1	530.31	3.1
531.32	0.1	530.81	2	530.3	3.1
531.31	-0.2	530.8	2.3	530.29	3
531.3	-0.3	530.79	2.6	530.28	2.7
531.29	0.1	530.78	2.8	530.27	2.7
531.28	0.3	530.77	2.6	530.26	2.8
531.27	0.3	530.76	2.4	530.25	2.9
531.26	0.2	530.75	2.2	530.24	2.9
531.25	0	530.74	2	530.23	2.8
531.24	-0.1	530.73	2.2	530.22	2.4
531.23	0.2	530.72	2.4	530.21	2
531.22	0.2	530.71	2.3	530.2	1.9
531.21	0.3	530.7	2.2	530.19	2.2
531.2	0.2	530.69	2.3	530.18	2.2
531.19	0.3	530.68	2.2	530.17	2.3
531.18	0.4	530.67	2.1	530.16	2
531.17	0.5	530.66	2.1	530.15	1.8
531.16	0.4	530.65	1.7	530.14	1.6
531.15	0.5	530.64	1.7	530.13	1.6
531.14	0.4	530.63	1.8	530.12	1.7
531.13	0.5	530.62	2	530.11	1.8
531.12	0.7	530.61	2.1	530.1	1.6
531.11	0.5	530.6	2.3	530.09	1.3
531.1	0.6	530.59	2	530.08	1.2
531.09	0.7	530.58	1.9	530.07	0.9
531.08	0.7	530.57	1.8	530.06	0.7
531.07	0.8	530.56	1.9	530.05	0.7
531.06	0.8	530.55	2.1	530.04	0.7
531.05	1	530.54	2.3	530.03	0.8
531.04	1.2	530.53	2.2	530.02	0.9
531.03	1.1	530.52	2.3	530.01	0.7
531.02	1	530.51	2.3	530	0.6
531.01	0.8	530.5	2.6	529.99	0.4
531	0.6	530.49	2.8	529.98	0.3

Wavelength [nm]	%T	Wavelength [nm]	%T	Wavelength [nm]	%T
529.97	0.4	529.46	0	528.95	-0.3
529.96	0.4	529.45	-0.1	528.94	-0.4
529.95	0.4	529.44	-0.3	528.93	-0.4
529.94	0.7	529.43	-0.4	528.92	-0.3
529.93	0.5	529.42	-0.3	528.91	0
529.92	0.4	529.41	-0.3	528.9	0.1
529.91	0.4	529.4	-0.2	528.89	0.1
529.9	0.6	529.39	-0.2	528.88	-0.1
529.89	0.6	529.38	-0.2	528.87	-0.1
529.88	0.6	529.37	-0.2	528.86	0
529.87	0.4	529.36	-0.1	528.85	0.2
529.86	0.1	529.35	-0.2	528.84	0.3
529.85	0	529.34	-0.1	528.83	0.2
529.84	-0.2	529.33	-0.1	528.82	0.1
529.83	-0.3	529.32	0	528.81	-0.1
529.82	-0.2	529.31	0.1	528.8	-0.2
529.81	-0.1	529.3	0.2	528.79	-0.2
529.8	-0.1	529.29	0.1	528.78	-0.2
529.79	0.1	529.28	0.1	528.77	-0.3
529.78	0.1	529.27	0	528.76	-0.4
529.77	0.2	529.26	-0.1	528.75	-0.4
529.76	0.3	529.25	-0.1	528.74	-0.4
529.75	0.1	529.24	-0.1	528.73	-0.2
529.74	0	529.23	-0.1	528.72	-0.1
529.73	-0.2	529.22	-0.4	528.71	0.2
529.72	0	529.21	-0.2	528.7	0.3
529.71	0	529.2	0.1	528.69	0.2
529.7	0.2	529.19	0.3	528.68	0
529.69	0.2	529.18	0.2	528.67	-0.1
529.68	0.4	529.17	0.2	528.66	-0.1
529.67	0.4	529.16	-0.2	528.65	0.2
529.66	0.4	529.15	-0.2	528.64	0.2
529.65	0.3	529.14	-0.2	528.63	0.1
529.64	0.2	529.13	-0.4	528.62	0.1
529.63	0	529.12	-0.4	528.61	-0.1
529.62	0.2	529.11	0	528.6	-0.1
529.61	0	529.1	0.1	528.59	-0.1
529.6	-0.1	529.09	0.2	528.58	-0.1
529.59	-0.1	529.08	0.1	528.57	-0.3
529.58	-0.2	529.07	0.1	528.56	-0.3
529.57	-0.2	529.06	0.1	528.55	-0.2
529.56	-0.1	529.05	0	528.54	0.1
529.55	-0.2	529.04	-0.2	528.53	0.4
529.54	-0.2	529.03	-0.4	528.52	0.3
529.53	-0.1	529.02	-0.4	528.51	-0.5
529.52	-0.1	529.01	-0.4	528.5	-0.9
529.51	0.1	529	-0.1	528.49	-0.8
529.5	0.3	528.99	-0.3	528.48	-0.6
529.49	0.3	528.98	-0.2	528.47	-0.1
529.48	0.2	528.97	-0.3	528.46	0
529.47	0.2	528.96	-0.1	528.45	-0.2

Wavelength [nm]	%T	Wavelength [nm]	%T	Wavelength [nm]	%T
528.43	0	527.92	-0.2	527.41	-0.1
528.42	0	527.91	-0.3	527.4	0.1
528.41	0.2	527.9	-0.2	527.39	0
528.4	-0.2	527.89	-0.2	527.38	-0.1
528.39	-0.4	527.88	-0.1	527.37	-0.1
528.38	-0.4	527.87	-0.4	527.36	-0.4
528.37	-0.3	527.86	-0.4	527.35	-0.5
528.36	-0.2	527.85	-0.3	527.34	-0.3
528.35	0.1	527.84	-0.1	527.33	-0.4
528.34	0.1	527.83	-0.1	527.32	-0.3
528.33	-0.1	527.82	0.1	527.31	-0.2
528.32	0	527.81	-0.1	527.3	-0.3
528.31	-0.1	527.8	-0.3	527.29	-0.2
528.3	0	527.79	0	527.28	0
528.29	0	527.78	0	527.27	-0.1
528.28	0.1	527.77	-0.3	527.26	0
528.27	0	527.76	-0.1	527.25	0
528.26	-0.1	527.75	0	527.24	-0.1
528.25	-0.5	527.74	0	527.23	-0.2
528.24	-0.3	527.73	0	527.22	-0.4
528.23	-0.4	527.72	-0.4	527.21	-0.7
528.22	-0.1	527.71	-0.6	527.2	-0.6
528.21	0	527.7	-0.7	527.19	-0.3
528.2	-0.1	527.69	-0.3	527.18	-0.2
528.19	-0.2	527.68	-0.2	527.17	-0.2
528.18	-0.3	527.67	-0.2	527.16	-0.1
528.17	-0.3	527.66	-0.3	527.15	-0.2
528.16	0	527.65	-0.1	527.14	0
528.15	0	527.64	-0.2	527.13	0.3
528.14	0	527.63	-0.1	527.12	0.4
528.13	-0.1	527.62	-0.4	527.11	0.3
528.12	-0.4	527.61	-0.6	527.1	0
528.11	-0.3	527.6	-0.5	527.09	-0.3
528.1	-0.1	527.59	-0.3	527.08	-0.4
528.09	-0.1	527.58	-0.1	527.07	-0.4
528.08	0	527.57	0	527.06	-0.4
528.07	-0.2	527.56	-0.1	527.05	-0.4
528.06	-0.2	527.55	-0.2	527.04	-0.2
528.05	-0.2	527.54	-0.3	527.03	0
528.04	-0.1	527.53	-0.4	527.02	0.1
528.03	0	527.52	-0.3	527.01	-0.1
528.02	0.1	527.51	-0.1	527	-0.9
528.01	0	527.5	-0.2		
528	0.3	527.49	0		
527.99	0.1	527.48	0		
527.98	-0.1	527.47	0.1		
527.97	-0.3	527.46	0.2		
527.96	-0.4	527.45	0.1		
527.95	-0.4	527.44	-0.1		
527.94	-0.2	527.43	-0.1		
527.93	-0.2	527.42	-0.2		

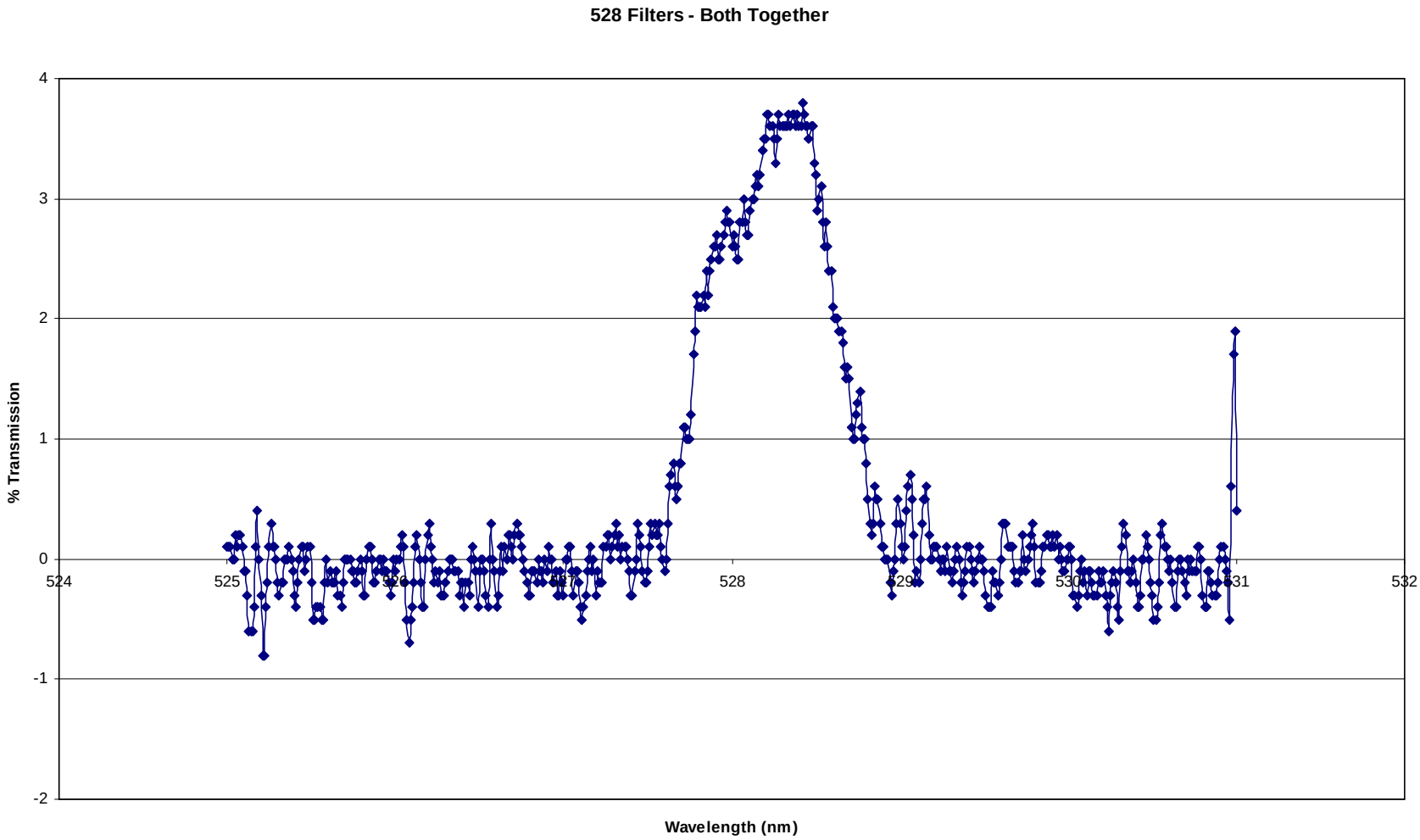

Figure C.1. Transmission values for 528 nm channel filter combination.

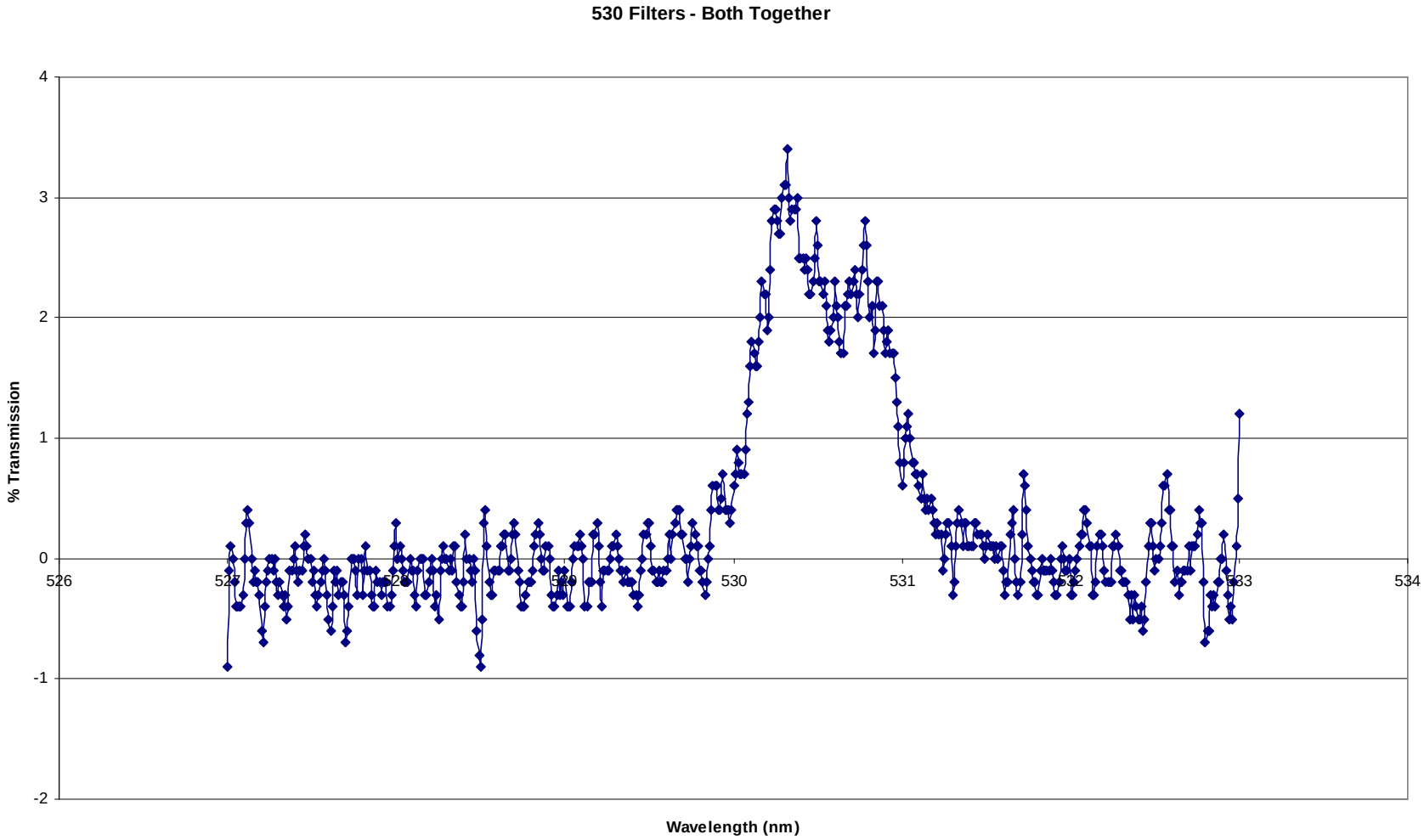

Figure C.2. Transmission values for 530 nm channel filter combination.